Article:

Restrepo-Coupe, N, Albert, LP, Longo, M et al. (14 more authors) (2021) Understanding water and energy fluxes in the Amazonia: Lessons from an observation-model intercomparison. Global Change Biology, 27 (9). pp. 1802-1819. ISSN 1354-1013

https://doi.org/10.1111/gcb.15555

Understanding water and energy fluxes in the Amazonia:

Lessons from an observation-model intercomparison

Running head: Seasonal water-energy flux in Amazon forests

Natalia Restrepo-Coupe[1,2], Loren P. Albert[1,3], Marcos Longo[5,6], Ian Baker[4], Naomi M. Levine[5,7], Lina M. Mercado[8,9], Alessandro C. da Araujo [10,11], Bradley O'Donnell Christoffersen[12,19], Marcos H. Costa[13], David R. Fitzjarrald[14], David Galbraith[15], Hewlley Imbuzeiro[13], Yadvinder Malhi [16], Celso von Randow[17], Xubin Zeng[18], Paul Moorcroft[5], Scott R. Saleska[1]

(1) Department of Ecology and Evolutionary Biology, University of Arizona, Tucson, AZ, USA.

(2) School of Life Sciences, University of Technology Sydney, Ultimo, NSW, Australia.

(3) Biology Department, West Virginia University, Morgantown, WV, USA.

(4) Colorado State University, Atmospheric Science, Fort Collins, CO, USA.

(5) Department of Organismic and Evolutionary Biology, Harvard University, Cambridge, MA, USA.

(6) Jet Propulsion Laboratory, California Institute of Technology, Pasadena, CA, USA.

(7) College of Letters, Arts, and Science, University of Southern California, Los Angeles, CA, USA.

(8) University of Exeter, College of Life and Environmental Sciences, Exeter, Devon, EX4 4RJ UK.

(9) Centre for Ecology and Hydrology, Wallingford, Oxfordshire, OX10 8BBUK, UK.

(10) Embrapa Amazônia Oriental, Belém, Pará, Brazil.

(11) Programa LBA, Instituto Nacional de Pesquisas da Amazônia (INPA), Manaus, Amazonas, Brazil.

(12) Department of Biology, University of Texas Rio Grande Valley, Edinburg, TX USA.

(13) Department of Agricultural Engineering, Federal University of Vicosa, Vicosa, MG, Brazil.

(14) University at Albany SUNY, Albany, NY, USA.

(15) School of Geography, University of Leeds, Leeds, UK.

[16] Environmental Change Institute, School of Geography and the Environment, University of Oxford, Oxford, UK.

[17] National Institute for Space Research, Brazil (INPE), Center for Earth Systems Science, São José dos Campos, SP, Brazil.

[18] Department of Hydrology and Atmospheric Sciences, University of Arizona, Tucson, AZ, USA.

[19] Earth and Environmental Sciences Division, Los Alamos National Laboratory, Los Alamos, NM, USA.

Correspondence: Natalia Restrepo-Coupe

email: nataliacoupe@gmail.com, phone: +1 647 328 1494

Key words: Evapotranspiration, energy balance, eddy covariance flux seasonality, Amazonia, tropical forests, land surface models, ecosystem-climate interactions.

Type of Paper: Primary Research Article.

Abstract

Tropical forests are an important part of global water and energy cycles, but the mechanisms that drive seasonality of their land-atmosphere exchanges have proven challenging to capture in models. Here, we (1) report the seasonality of fluxes of latent heat (*LE*), sensible heat (*H*), and outgoing short and longwave radiation at four diverse tropical forest sites across Amazonia -- along the equator from the Caxiuanã and Tapajós National Forests in the eastern Amazon to a forest near Manaus, and from the equatorial zone to the southern forest in Reserva Jaru; (2) investigate how vegetation and climate influence these fluxes; and (3) evaluate land surface model (LSM) performance by comparing simulations to observations. We found that previously identified failure of models to capture observed dry-season increases in evapotranspiration was

associated with model over-estimations of (1) magnitude and seasonality of Bowen ratios (relative to aseasonal observations in which sensible was only 20-30% of the latent heat flux) indicating model exaggerated water limitation, (2) canopy emissivity and reflectance (albedo was only 10 to 15% of incoming solar radiation, compared to 0.15-0.22% simulated), and (3) vegetation temperatures (due to underestimation of dry-season evapotranspiration and associated cooling). These partially compensating model-observation discrepancies (e.g. higher temperatures expected from excess Bowen ratios were partially ameliorated by brighter leaves and more interception/evaporation) significantly biased seasonal model estimates of net radiation (*Rn*), the key driver of water and energy fluxes ($LE \sim 0.6Rn$ and $H \sim 0.15Rn$). Though these biases varied among sites and models. A better representation of energy-related parameters associated with dynamic phenology (e.g. leaf optical properties, canopy interception, and skin temperature) could improve simulations and benchmarking of current vegetation-atmosphere exchange and reduce uncertainty of regional and global biogeochemical models.

1. Introduction

Tropical forests play a major role in the global water and energy cycles, and modulate tropical atmospheric circulation processes, cloud formation and precipitation (Hagos & Leung, 2011; Held & Soden, 2006; Jasechko et al., 2013; Silva Dias et al., 2002; Wei et al., 2017; Worden et al., 2007). Water and energy fluxes are intrinsically linked, as energy is required for the phase transition from liquid to vapor. Tropical forests evapotranspire the energy equivalent of more than half of the total solar energy absorbed by earth's land surfaces (Trenberth et al., 2009), helping to maintain high atmospheric water content, increase moisture recycling, and mediate cloud development (Peters, 2016; Tan et al., 2019). Evapotranspiration (*ET*) mitigates heating as part of the incoming radiation is primarily "consumed" as latent heat (*LE)* rather than as sensible heat flux (*H*). High *ET* rates can offset the warming effect associated with tropical forest low albedo (the ratio of reflected to incoming shortwave radiation, SW_{out}/SW_{down}) driven by its relatively dark surface (Bonan, 2008; Yanagi & Costa, 2011). Therefore, land use change, fire, climate and extreme weather events (Aragão et al., 2007, 2008; Chagnon & Bras, 2005; Davidson et al., 2012) are listed as key factors determining subsequent changes in tropical forest albedo's (negative climate forcing) and alterations of the evaporative cooling flux (positive feedbacks – reducing warming) (Bonan, 2008; Li et al., 2015; Liu et al., 2019). Measuring and understanding water, radiation, and energy seasonal fluxes under present climatological conditions is thus needed to forecast the future of tropical forests and global atmospheric cycles (Fu et al., 2013; Sena et al., 2018; Spracklen et al., 2018).

Land-surface models (LSMs) represent our mechanistic understanding of cause-effect relationships between the surface and the atmosphere and constitute ideal tools to forecast water, energy and other biogeochemical fluxes (Pitman, 2003). However, given that ecosystem characteristics are diverse and that land-climate interactions are heterogeneous and complex, it is not surprising that LSMs have difficulty in reproducing the seasonality of rainforest *ET* (Baker et al., 2008; Christoffersen et al., 2014; Costa et al., 2010; Fisher et al., 2014; Restrepo-Coupe et al., 2017). A consistent problem is that models simulate reductions in *ET* during the dry season (when precipitation is less than ~100 mm month^{-1}), when most observations from eddy covariance towers in Amazonia show no reductions or even increases in *LE*, consistent with control by the availability of energy (net radiation), and inconsistent with limitation by available water (Baker et al., 2008; Christoffersen et al., 2014; Costa et al., 2010; R. A. Fisher et al., 2007; Restrepo-Coupe et al., 2017; Shuttleworth, 1988).

Previous attempts to improve the dry-season *LE* discrepancies between LSM simulations and observations of tropical forests, have been focused on the parameterization of higher soil water holding capacity, hydraulic redistribution (vegetation control mechanisms), deeper roots that can access the lower soil layers and/or increase root mass (enhanced pathways) and dynamics of stem‑water storage (plant hydraulics) (Baker et al., 2008; Christoffersen et al., 2014; Harper et al., 2010; Lee et al., 2005; Yan et al., 2020). Unfortunately, some of these model modifications appear to drive LSMs to (1) overestimate annual and/or dry-season *ET* and/or (2) model simulations could become insensitive to drought conditions.

Christoffersen et al. (2014) previously analyzed simulations from the same model-data intercomparison investigated here, focusing on modeled mechanisms of water supply (rooting depth, access to groundwater sources, and soil water availability) and vegetation demand (intrinsic water use efficiency (*iWUE*) and stomatal conductance) that drive the simulated dry-season reductions in *ET*. Chirstoffersen et al. (2014) identified model underrepresentation of phenological processes (including leaf development and associated changes in *iWUE*) as a cause of the bias. When these same LSM simulations were evaluated for their ability to represent the seasonal dynamics of carbon fluxes in these same tropical forests (Restrepo-Coupe et al., 2017), the analysis found that although water limitation was represented in models as the primary driver of the seasonality of photosynthesis across Amazonia, the LSMs did not accurately represent that seasonality. Observations showed incoming radiation and phenological cycles that included allocation lags between wood, leaf and non-structural carbon, and light harvesting adaptations (e.g., leaf demography) dominated carbon exchange and in some instances, were not well represented in LSMs. Both carbon and water fluxes are significantly influenced by tropical forest phenology (Chen et al., 2020; Restrepo-Coupe et al., 2017). However, the relationship between vegetation seasonal cycles and the radiation and energy exchange is not well documented.

Here, we extend the prior work of Christoffersen et al (2014) and Restrepo-Coupe et al., (2017), building on the consistent finding that *LE* appears to be controlled by net radiation (*Rn*). If this finding is correct, then inherent to the challenge of accurate modeling of *ET* (equivalent *LE*) is the accurate simulation of the other radiation components (LW_{out} and SW_{out}), as well as the accurate partitioning of the relevant energy fluxes (e.g. energy allocated to *LE* and *H*) (Bony et al., 2013; Getirana et al., 2014; Longo et al., 2019a), in addition to the accurate representation of phenological attributes (e.g. leaf-age driving seasonal canopy conductance values) (Lin et al., 2015; Medlyn et al., 2011) (see Figure 1). Yet, in tropical forests and across Amazonia there is scarce information on the seasonal cycle of energy-relevant components *H*, albedo (α), emissivity (ε_s), the Bowen ratio (*Bowen=H/LE*), and the outgoing and incoming longwave radiation (LW_{out} and LW_{down}).

Focusing on energy dynamics, we compare forest characteristics and water and energy fluxes from eddy covariance (EC) and meteorological observations at four tropical forest sites from the Brasil flux network, three Amazonian forests close to the Amazon river (Manaus-K34, Tapajós-K67, and Caxiuanã-CAX) and one southern location (Reserva Jaru-RJA) to four state-of-the-art land surface models (IBIS, ED2, JULES, and CLM3.5) (Restrepo-Coupe et al., 2017). The aim of this work is threefold: (1) to quantify and characterize the seasonal fluxes (timing and amplitude) and surface properties of the different water, energy and radiation cycle components; (2) to determine the relationships between these energy-related fluxes and vegetation and climate drivers, as we investigate the ability of other simple models and relations to predict ecosystem-level fluxes (e.g. linear regressions between *Rn* and *LE*); and (3) to identify areas to refine current LSM model formulations and to enhance seasonal *LE, H* and *Rn* simulations by including vegetation characteristics (e.g. albedo) in the analysis and improving the derivation of radiative fluxes (e.g. outgoing *SW* and *LW*), with special attention to the inherent coupling of carbon, energy and water cycles (Figure 1).

2. Methods

2.1. Site descriptions

Data were obtained at four EC flux tower tropical forest locations (Figure 2). All sites were established by the Brazilian-led Large-Scale Biosphere-Atmosphere Experiment in Amazonia (LBA-ECO) (Keller et al., 2004) and members of the Brasil flux network (da Rocha et al., 2004; Restrepo-Coupe et al., 2013). Three EC stations comprise a longitudinal transect close to the equator (~3°S) along the Amazon river from east to west, from high to low mean annual net radiation (Figure 2) and different seasonal patterns of monthly precipitation: Caxiuanã (CAX), the Tapajós National forest near Santarém (K67) and the Reserva Cuieiras near Manaus (K34). The fourth site, the Ji-Paraná Reserva Jaru (RJA) forest, is located at the southern margins of the basin, at latitude 10°S. For a detailed site description refer to previous works by da Rocha et al. (2009), Restrepo-Coupe et al. (2013, 2017) and Table S1.

2.2 Eddy flux (EC), meteorological and biometric data

Sensible heat (*H*), water (*ET*) and carbon fluxes (*Fc*) were measured using the EC method (Baldocchi et al., 1988; Wofsy et al., 1993). Hourly average covariances were obtained from high frequency observations (20 Hz) of vertical wind velocity, virtual temperature (T_{son}; °C), and water (H_2O_{mix}; mmol mol^{-1}), and carbon dioxide (CO_2; ppm) mixing ratios measured with a 3D sonic anemometer (CSAT) and an infrared gas analyzer (LI6262) (Burba, 2010; Foken et al., 2012). The *LE* was calculated as the product of water mass transfer (*ET*; mm day^{-1}) and latent heat of vaporization (λ; MJ kg^{-1}), where $LE = ET\,\lambda$. The λ calculated as a function of air temperature (Brutsaert, 1982).

Meteorological observations included: air temperature (T_{air}; °C), relative humidity (*RH*; %), precipitation (*Precip*; mm), wind speed (*ws*; m s^{-1}), turbulence measured as friction velocity (u_*; m s^{-1}), and the following radiation fluxes in W m^{-2}: incoming (SW_{down}) and outgoing shortwave (SW_{out}), and incoming (LW_{down}) and outgoing longwave (LW_{out}). Net radiation (*Rn*; W m^{-2}) was defined as the balance between incoming and outgoing fluxes ($Rn = SW_{down} - SW_{out} + LW_{down} - LW_{out}$). A four-dome net radiometer, CNR1 (Kipp & Zonen CM3 ISO-class, thermopile pyranometer, CG3 pyrgeometer, PT100 RTD) was used for the measurement of SW_{down}, SW_{out}, LW_{down} and LW_{out}, at all sites. The shortwave (*SW*) or solar radiation was defined as broadband radiation between 0.3 to 3 µm and the longwave (*LW*) as radiation with a spectral range from 3 and 300 µm. An independent *Rn* measurement from a single-component radiometer was available at K34 and K67.

Hourly data were subject to various quality control procedures: Values found to be outside ±3-standard deviations from the mean were removed for *ws*, *RH*, and T_{air}. Analogous and concurrent measurements were used to identify periods of instrument malfunction (e.g. T_{son} and T_{air}) recognized by observations outside 2-times the standard deviations from the linear relationship between the variables. Similarly to processing carbon flux data, we removed *LE* fluxes measured during low turbulence conditions (given a site-specific u_* threshold, $u_{*thresh}$), thus the EC method's no-advection assumption does not apply (see Restrepo-Coupe et al. 2013) (Table S1).

The energy balance was defined as $Rn\text{-}\Delta = LE+H+\Delta Sh+\Delta Sc+\Delta Sb$, where ΔSh is the sensible heat storage on the canopy layer storage, ΔSc is the energy change due to photosynthetic activity, ΔSb is the biomass heat storage, and Δ is the imbalance (Figure S1 and S2). The Δ term includes measurement errors (e.g. differences between the footprint of the radiation sensor and the EC and loss of low frequency large-scale eddies) and unaccounted fluxes: ground heat flux (*G*) and changes in the latent heat flux stored on the air column below the EC system (ΔSle). At K34 where profile temperature observations were not available, the Δ included ΔSh and ΔSb, as well.

The ΔSh was calculated as the hourly change in temperature across the air column (eight, five and four height levels at K67, RJA, and CAX, respectively) multiplied by air density and specific heat at constant pressure (Figure S3). The ΔSc was defined as the product of gross ecosystem productivity (see Sec. 2.4.) and the specific energy of conversion due to photosynthesis (1.088×10^4 J gCO_2^{-1}) (Moderow et al., 2009). We calculated ΔSb as the product of canopy-specific heat capacity (C_{veg} = 2958 J kg^{-1} K^{-1}), live wet biomass (m_{veg}; kg m^{-2}) and the change in temperature at canopy level (T_{cpy}; K). See SI for m_{veg} values and T_{cpy} heights. To flag possible outliers, as part of our QA procedures, we used the slope of the regression (*Rn vs. LE+H+*ΔSh*+*ΔSc*+*ΔSb*)* assuming the observations outside 2-times the standard deviations from the linear relationship (see Figure S6).

We reviewed the seasonality of the energy balance residual as to improve the confidence in our analysis rather than determine *LE*-corrected values (i.e., we did not force energy balance closure). Note that we observed no statistically significant differences in the seasonal (monthly) energy balance closure (Figure S1 and S5). For an extensive review of the energy balance problem, the reader is invited to refer to the work of Foken (2008), subsequent studies (Mauder et al., 2018; Reed et al., 2018) and our supporting information (SI).

At each EC site, meteorological drivers for the LSMs were generated from the standard suite of climatic variables available for periods between 1999 and 2006. We analyzed data for 2000-2005 for K34, 2002-2004 for K67, 2000-2002 for RJA and 1999-2003 for CAX. Drivers included: LW_{down}, SW_{down}, T_{air}, *ws*, near surface specific humidity (Q_{air}; g kg^{-1}), rainfall (*Precip*;

mm month^{-1}), and surface atmospheric pressure (P_a; hPa) (Figure 3). The CO_2 concentration (CO_{2air}; ppm) was fixed at 375 ppm, the average value during the period of measurements (de Goncalves et al., 2009). Observational data were filled using other nearby meteorological sites and/or the mean monthly diurnal cycle; however, only successive years with gaps no larger than two consecutive months were accepted. Although model drivers were gap-filled, regressions, and other calculations presented in this manuscript were implemented using only non-filled flux observations and meteorological values. We sampled the EC data to match the timing of the model drivers and output.

Biogeochemical fluxes can be sensitive to canopy structure and function. For our analysis we used 16-day values of leaf area index (*LAI*), net primary productivity (*NPP*) allocated to leaves (NPP_{leaf}; $gC\ m^{-2}\ d^{-1}$), wood (NPP_{wood}; $gC\ m^{-2}\ d^{-1}$) and litterfall (NPP_{litter}; $gC\ m^{-2}\ d^{-1}$). Litterfall data were available for all forests and included recently published values by Freire et al. (2020) for RJA. We used previously published *LAI* values -- see Table S1 for references, values and methods. For a description of biometric sampling methods see the original works of Metcalfe et al. (2007), Brando et al. (2010), Rice et al. (2004), and Fisher et al. (2007) and for calculations and a description of the *NPP* seasonal values see Restrepo-Coupe et al. (2017).

2.3. Surface emissivity (ε_s), Bowen ratio, outgoing longwave radiation (LW_{out}), and other calculations

We used observations of the longwave radiation balance (LW_{down} and LW_{out}) as per the integral of the Planck radiation function, the Stefan-Boltzmann equation, to obtain the measure of the surface's ability to emit energy by radiation, the Earth's surface spectral emissivity (ε_s):

$$LW_{out} = \varepsilon_s \sigma_{SB} T^4_{skin} + (1 - \varepsilon_s) LW_{down} \qquad \text{Equation 1}$$

where σ_{SB} is 5.6704×10^{-8} W m^{-2} K^{-4} the Stefan-Boltzmann constant, T_{skin} is the skin temperature (K) and ε_a is the effective emissivity of the atmosphere (Jin & Liang, 2006). The equation included the reflected fraction of LW_{down} the second term ($\left(1 - \varepsilon_s\right) LW_{down}$), following Kirchhoff's law, which assumes that absorptivity and emissivity are the same for each spectral band (Liou, 2002). We used canopy level temperature measurements (lagged as to reach a maximum four hours after peak T_{air}) as a proxy for T_{skin} (Moderow et al., 2009) (see SI section 4). No contact thermometry was installed at any of the study sites. We solved for ε_s:

$$\varepsilon_s = \frac{LW_{out} - LW_{down}}{\sigma_{SB} T^4_{skin} - LW_{down}} \qquad \text{Equation 2}$$

The derivation of ε_s is a simplification of a complex process: We did not account for the vertical variations of T_{air}, and we neglected the re-emission of *LW* radiation by water vapor. Nonetheless, we are measuring LW_{down} and LW_{out} at the four forests and we see this calculation as an improvement over the assumed emissivity values used by some LSMs. Similarly, to identify possible bias on model LW_{out} calculations, we solved Equation 2 for T_{skin} assuming ε_s values of 0.99 (see SI section 4).

Here we include 1-km grid MOD11A2.v6 (Wan et al., 2015) the land surface temperature (*LST)* product to scale and compare T_{air} measurements to satellite-derived land-surface temperature used by some models on their emissivity calculations (Figure S8).

To describe the forest optical brightness, we calculated the daytime albedo (top of the atmosphere radiation, TOA>200 W m^{-2}) as the unitless ratio of outgoing to incoming solar radiation ($\alpha = SW_{out}/SW_{down}$). We computed the TOA following Goudriaan (1986) and set a threshold of TOA and SW_{down} > 200 W m^{-2} to constrain daytime observations. To characterize the heat transfer and the partition between water and sensible heat fluxes, we used the Bowen ratio calculated as the fraction of H to LE ($Bowen = H/LE$). The Bowen ratio is used by some models as a driver in stomatal conductance and photosynthesis calculations (Berry et al., 2013; Sellers, 1985).

2.4. Vegetation contributions to *ET*

To quantify the vegetation response to meteorology, we evaluated the seasonal differences between observed ET and the reference ET (ET_{ref}) (also known as potential ET). The ET_{ref} is solely driven by atmospheric demand and climatic parameters and independent of the vegetation water use and soil factors. The ET_{ref} was calculated following the FAO Penman-Monteith method as:

$$ET_{ref} = \frac{\delta}{\delta+\gamma} Rn \qquad \text{Equation 3}$$

where γ is the psychrometric coefficient ($C_p\, P_a\, 10^3 / 0.622\, \lambda$; kPa K^{-1}), and δ is the slope of vapor pressure curve ($\delta = 4098\, e_{sat} / T_{air}^{-2}$; kPa K^{-1}), and C_p is the specific heat of air at constant pressure (J kg^{-1} K^{-1}).

We calculated the ecosystem water use efficiency (*WUE*) as the ratio between daytime photosynthetic activity (TOA>200 W m^{-2}) measured as the gross primary productivity ($GPP_{day\&dry}$; gC m^{-2} d^{-1}) to $ET_{day\&dry}$ over a 16-day period ($WUE = GPP_{day\&dry}/ET_{day\&dry}$; gC mm^{-1}). The $ET_{day\&dry}$ (mm d^{-1}) was measured excluding observations during and 12-hours after precipitation, and using only daytime data, and was assumed to be the *ET* dominated by transpiration (*T*) fluxes rather than by direct evaporation (*E*) from interception (e.g. after rain) and from condensation (e.g. dawn measurements). Similarly, the TOA threshold removed all early morning - late afternoon values from the *WUE* calculations, thus small *ET* values translated into abnormally high efficiencies without physical merit. Here, we use the term gross primary productivity (*GPP*) interchangeably with gross ecosystem productivity (*GEP*; gC m^{-2} d^{-1}) and negative gross ecosystem exchange (*GEE*; gC m^{-2} d^{-1}), where $GPP \sim GEP = -GEE$ (Stoy et al., 2006). The *GEE* was estimated from the measured daytime net ecosystem exchange (*NEE*; gC m^{-2} d^{-1}) by subtracting estimates of ecosystem respiration (R_{eco}; gC m^{-2} d^{-1}), which in turn were derived from nighttime *NEE* ($GEE = -NEE + R_{eco}$). The *NEE* was calculated as the sum of the fluxes measured at the top of the tower and the CO_2 storage flux ($NEE = Fc + S_{CO2}$) and filtered for low turbulence periods (site-specific $u_{*thresh}$). R_{eco} was calculated as the average within a centered 5-day wide moving window, assuming at least 8 valid hours of nighttime *NEE* (we expanded the window up to 30 days until sufficient valid data were included). The selected R_{eco} moving window accounts for sensitivity to seasonally varying soil moisture. Daytime R_{eco} was assumed to be equal to nighttime R_{eco}. See SI and Restrepo-Coupe et al. (2013, 2017) for uncertainty analysis and additional methods.

To better understand the contribution of vegetation to *LE* and consequently to the partition of turbulent heat fluxes (Figure 1), we calculated the canopy stomatal resistance to water vapor (*rsV*; s m^{-1}) and the corresponding canopy conductance (G_S; mmol m^{-2} s^{-1}) following the flux-gradient method as described by Wehr and Saleska (2015; 2020, 2021) (see SI section 6 for calculations and sensitivity analysis).

2.5. Land surface models (LSMs)

We present output from four process-based land surface models that were part of the 'Interactions between Climate, Forests, and Land Use in the Amazon Basin: Modeling and Mitigating Large Scale Savannization' project (Powell et al., 2013; Restrepo-Coupe et al., 2017). We used the Community Land Model-Dynamic Global Vegetation Model version 3.5 (CLM3.5) (Gotangco Castillo et al., 2012; Oleson et al., 2008; Stockli et al., 2008), the Ecosystem Demography model version 2 (ED2) (Longo et al., 2018; Longo et al., 2019b; Medvigy et al., 2009), the Integrated Biosphere Simulator (IBIS) (Foley et al., 1996; Kucharik et al., 2000) and the Joint UK Land Environment Simulator (JULES v.2.1) (Best et al., 2011; Clark et al., 2011).

The LSMs energy and water cycle dynamics, including how radiation and conductances were calculated by models are presented in Table S2.

Models compute *Rn* as the sum of LW_{down} and SW_{down} (forcing drivers) minus the outgoing energy flux, the LW_{out} and SW_{out} calculated using parameters assigned to a plant functional type (PFT) and/or via different canopy radiation transfer models and equations (e.g. the two-stream model and the Beer-Lambert law) (Fisher et al., 2018). Later, *Rn* is partitioned into *LE* and *H*. This partition is determined by atmospheric demand and the amount of water available for evaporation and transpiration (if the water supply is exhausted, energy will ultimately be spent exclusively on *H*). If water is available, *LE* will be driven by temperature, wind velocity, available radiant energy and will be modulated by G_s and aerodynamic conductance (*Gi*) (Figure 1). The G_s, representing the exchange of CO_2 and H_2O between multiple canopy leaves and the atmosphere, is controlled by meteorological and edaphic conditions given the ecosystem's structure, and by plant trait expressions that determine the photosynthetic capacity (e.g. quality and quantity of leaves and stomatal behavior). Therefore, G_s links the energy, carbon and water cycles and constitutes a key vegetation status descriptor for LSMs.

LSMs calculated the down-regulation factor for stomatal conductance due to soil water stress (FSW) (also known as the β term) following Oleson et al. (2008) (CLM3.5) and Castanho et al. (2016) (ED2, IBIS, and JULES). The FSW factor ranges from 0 (maximum stress) to 1 (no stress).

Model diagnostic variables complied with radiation energy and water conservation equations (Equation 6 and 7). The energy balance residual was always smaller than 1 W m^{-2}:

$$SW_{down} - SW_{out} + LW_{down} - LW_{out} - H - LE - G = \Delta S_b + \Delta S_h \qquad \text{Equation 9}$$

And the water balance residual was less than 1×10^{-6} kg m^{-2} s^{-1}, defined by:

$$Prec - ET - R - GW + F = (\Delta_{\mathrm{intercept}} + \Delta_{srfstor} + \Delta_{soilmoist})/dt \qquad \text{Equation 10}$$

where R is surface runoff, GW is subsurface runoff, F is recharge from rivers, and the $\Delta_{intercept}$, $\Delta_{srfstor}$ and $\Delta_{soilmoist}$ are changes in interception, surface storage, and soil moisture, respectively (all values in units of kg m^{-2} s^{-1}).

2.6. Calculating seasonality and comparing models to observations

For each hour on the 16-day period we used all available measurements (minimum four observations per hour) (Figure S7). We calculated the mean of the average daily cycle (minimum 22/24 hours of the cycle were required for calculation of seasonal mean). This method avoids assigning less weight to those periods where we have fewer measurements. For example, at K34 precipitation was common in the late afternoon; therefore, *LE*, *H*, and other measurements that depend on the sonic anemometer were unavailable during rainfall events (Figure S9). Seasonal *WUE* ($GEP_{day\&dry}/ ET_{day\&dry}$) and ET/ET_{ref} were calculated using 16-day ratios. The average annual cycle was calculated from all available 16-day periods when at least two measurements were available (2-years of data for each period).

Models were compared to observations based on the timing and amplitude metrics of their annual cycle. Correlation coefficient (*r*), root-mean-square difference of model-observations (RMSE), and the ratio of their variances were determined for the 16-day multiple years' time series and the difference in amplitude and timing of the seasonal cycle were summarized using the unitless normalized standard deviation calculated as the ratio between model (σ_m) and observations (σ) standard deviation via Taylor diagrams (Taylor, 2001) (see Figure 3e for its interpretation). Sites missing from figures indicate that the model overestimated the seasonality of observations and σ was greater than two.

We used Type II linear regressions between fluxes, parameters and variables to understand and quantify the relationships between flux drivers and meteorological variables (e.g. *H vs*. *Rn*) and between ecosystem characteristics and processes (e.g. *LAI vs*. albedo), thus acknowledging both variables carried some degree of uncertainty. To describe the statistical significance of regressions, we calculated p-values and the coefficient of determination (r^2), and the Akaike's Information Criterion (AIC), among other descriptors. We compared the resulting linear models to simulations (benchmark) to identify key flux drivers and determine when and how LSMs can be under-utilizing the available variable information (Abramowitz, 2005; Best et al., 2015).

3. Results

3.1. Seasonal meteorology and evapotranspiration (*ET*)

All sites showed contrasting degrees of seasonality in terms of rain, temperature, insolation, and/or day-length; including differences in the amplitude of the radiation and precipitation annual cycles and the timing metrics that define the start, end, peak and dry season length (Figure 3). Mean annual precipitation at RJA and K67 was close to 2000 mm compared to 2500 mm at CAX and K34. The dry season varied in length and strength from the 1-month long at K34 to the 5-month at K67 and RJA (Figure 3). Although the dry season at K34 only lasted for one month (August), there was a period from July to October when the precipitation was lower than the annual mean and when we observed above average incoming radiation values (similar seasonality to K67 and CAX). The number and intensity of precipitation events was different: (1) CAX with frequent-low intensity rainfall (>=250 events month^{-1} of <0.5 mm hr^{-1}), (2) strong seasonal changes at RJA (dry-season with few lower than 0.5 mm hr^{-1} intensity events and wet-seaso with ~50 events higher than 2.5 mm hr^{-1}), and (3) K67 and K34 close to aseasonal intensities (2.5 mm hr^{-1}); however, there were fewer events at K67 (<=50 events month^{-1}) compared to K34 (<=100 events month^{-1}) (Figure S9).

The observed annual cycle of *ET* showed three different patterns across forests: (1) maximum water vapor flux at the beginning of the dry season declining as the season progressed at the two wettest locations (K34 and CAX); (2) a well-defined *ET* cycle, with a middle of the dry-season peak at K67; and (3) an aseasonal *LE* flux at the southern forest of RJA (Figure 3c and 4a). Modeled *ET* showed seasonal synchronicity with observations at the two wettest sites (K34 and CAX); however, LSMs overestimated the dry-season flux by 150-20 mm month^{-1} (Figure 3c). At K67 and RJA, models exaggerated the amplitude of the water flux seasonal cycle by 180-20 mm month^{-1}. At these drier locations, LSM's predicted reductions in dry season *ET* that were generally driven by the available soil moisture, as demonstrated by the statistically significant relationship between flux and the plant available water model diagnostic FSW (p-value<0.01 r^2 from 0.1 (IBIS) to 0.7 (ED2) at K67 and 0.3 (ED2) to 0.7 (CLM3.5) at RJA) (Figure 3d and S10). By contrast, observations showed available energy driving *ET* at all sites (Table S3). The slope of the regression between seasonal *LE vs. Rn* (type II, zero intercept) was ~0.6 (Figure S11) (r^2 = 0.7 at CAX, 0.8 at K34, 0.5 at K67 and 0.1 at RJA). Seasonal T_{air} and *LE* showed a significant positive correlation (r^2 = 0.42, p-value<0.01) at only one site, K67 (Table S3). The ET_{day} was close to constant (7.7 mm day^{-1}) at the southern forest of RJA. RJA was the only forest where we observed no significant correlation between *Rn* and *ET* (r^2<0.1, p-value=0.9) however, the linear model had a low RMSE value (7.78 W m^{-2}). Moreover, all site regressions between Rn_{day} and LE_{day} showed RJA observations following the general trend (Figure 8).

3.2. Partition of net radiation into turbulent fluxes

At the equatorial Amazon forests (K34, CAX, and K67), the 16-day cycle of *H* showed a maximum at the beginning and a minimum at the end of the dry season (Figure 4b). By contrast, *H* was close to aseasonal at RJA (a slight increase by the middle of the dry period). Models were able to capture the seasonal cycle of *H* at CAX; however, the dry-season *H* was underestimated by most of the LSMs at K34. LSMs overestimated *LE* and were out of phase with observations at K67 and RJA (Figure 4b). At K34 and RJA the relationship between observed *H* and *LE* was weak (r^2<0.2, p-value<0.01) and significant at CAX and K67 (r^2=0.6, p-value<0.01) (Figure S11). At RJA and CAX measurements of *Rn* explained 50% of the *H* seasonal variability. Moreover, *H* was significantly correlated with *Rn,* the slope (zero intercept) varying from 0.12 at K67, 0.15 at CAX and RJA, to 0.22 at K34 (r^2 ~ 0.4, p-value<0.01) (Figure S11).

Observations showed that Bowen ratio values were nearly constant at ~0.32 for K34 (highest) and at ~0.21 for RJA and K67 (lowest among forests). We found that the Bowen ratio for the four LSMs was lower than the observed value at the two wettest locations (K34 and CAX) and above measurements at the two driest forests (K67 and RJA). Simulations showed a strong increase in Bowen ratio during the dry season at K67 (IBIS and ED2) and at RJA (all models) (Figure 4c).

Hourly and seasonal observations showed a good seasonal energy balance closure (slope $LE + H$ *vs.* Rn) ranging from 90% (CAX), 88% (K67 and K34) to 83% (RJA) (Figure S1 and S2). By comparison, FLUXNET sites have an average imbalance of ~20% (Wilson et al., 2002). Where profile temperature data were available, the introduction of canopy and biomass heat storage improved the overall hourly balance, especially the energy closure at dawn and dusk (see supplemental material, Figure S3). The Δ showed a statistically significant correlation to Rn ($\Delta \sim 0.1 Rn$, $r^2 > 0.8$, p-value<0.01) and no correlation to turbulence, T_{air} or rainfall (Figure S3 and S4). Therefore, we had no indication of lost fluxes due to advection (low u_*) or errors associated to turbulence bursts (high u_*). At CAX, frequent rainfall events made EC measurements challenging, and extensive periods of data needed to be removed (causing gaps in many regressions and figures). Rainfall events at CAX were less intense, however more frequent than at any other site (see Figure S9).

3.3. Radiation balance: Outgoing longwave (LW_{out}) and reflected shortwave (SW_{out}) radiation

The SW_{out} is determined by the surface reflectance (e.g. we see low SW_{out} values in dark bodies, and high values in bright bodies) and its relation to SW_{down} is measured as albedo (α) (Figure 5). Seasonality of α showed modest increases as the dry-season progressed at all sites and was in-phase with the radiation seasonal cycle (Figure S15). Peak α values (when forest was at its brightest) were observed by the middle of the dry season at the equatorial Amazon sites (CAX, K34, and K67) and at the end of the dry period at RJA (Figure 6a). The average α was 0.12 at RJA, K34 and K67 and 0.09 at CAX. Negative regressions between precipitation and α (the forest was darkest at the peak of the wet season) were statistically significant at all forests (p-values <0.01 with r^2 values up to 0.4 at K67 and K34) (Figure S13). The forest characteristics showed some degree of correlation: (1) low *LAI* to high α (negative slope) at CAX, and (2) high NPP_{leaf} to high canopy brightness (positive slope) at K67, RJA, and K34 (Figure S14). However, at all sites, the timing of maximum α did correlate with peak leaf-flush greenness index phenocam observations (e.g. Lopes et al., 2016). Models overestimated α annual mean across sites and underestimated the amplitude of the α seasonal cycle.

Observations showed mean monthly values of SW_{out} close to 20 W m^{-2} at most forests (Figure 5a). The models captured the seasonal cycle of SW_{out} at all sites except RJA. The SW_{out} was significantly correlated with SW_{down} (r^2 = 0.9 at K34 and RJA, 0.7 at K67 and r^2 = 0.5 at CAX; p-values <0.01), with the slope of their linear relationship increasing from wet to dry forests, such as 0.12 at K34 and CAX, 0.13 at K67 and 0.14 at RJA (Figure S15). Seasonal LW_{out} was significantly correlated with LW_{down}, however R^2 values were low ($r^2 = 0.34$ at K34, 0.5 at K67 and $r^2 = 0.2$ at CAX and RJA, p-values <0.01) with a positive slope at K34 and RJA and a negative regression (LW_{down} increased faster than LW_{out} and surface-canopy temperature warming at a lower rate than the air) at CAX and K67 (Figure S17). At K67, CAX, and RJA, models captured the amplitude of the seasonal LW_{out} cycle, however at K34 the LW_{out} all models' simulations were out of phase with observations (Figure 5b).

The amplitude of the annual surface emissivity (ε_s) cycle representing the ability of the surface to emit longwave radiation, showed high dry-season values at RJA and CAX (Figure 6b). By contrast at CAX, observations showed low wet season ε_s values. At K34 and K67 observed ε_s were higher than 0.98 and close to 0.95 at RJA. We found statistically significant correlations ($p<0.01$, r^2 range 0.3 to 0.8) between ε_s and rainfall (positive) and T_{air} (negative) at K34 and vice versa at CAX -- no significant correlation was observed at K67 and RJA (Figure S13). LSMs generally did not capture the magnitude or seasonality of ε_s, and no LSM aligned with observations across all sites (Figure 6b). Assuming constant ε_s values of ~0.99 in agreement with satellite measurements (Figure S8), showed models either overestimated T_{skin} (~1 to 5°C) or underestimated ε_s (Figure S12).

3.4. Ecosystem characteristics and contributions to the water and energy flux seasonality

The ratio between observed ET and ET_{ref} can be used to identify the periods when ET does not show any signs of water-supply limitation and the flux is mostly driven by atmospheric demand

and solar radiation (Figure 3c and S19). Only during the wettest months at K34 we observed *ET* equivalent to ET_{ref} (ET/ET_{ref} ~100%) and ~70% during the driest period (Figure 7a). In general, the slope of the regression between *ET* and ET_{ref} varied from 0.66 (RJA) to 0.74 (K67 and K34), with statistically significant differences between wet and dry season values only seen at RJA and K34 (Figure S19).

The vegetation control over *ET*, here represented by G_s, showed different degrees of seasonality and trends across forests (Figure 7b); nevertheless minimum values were observed at various times during the dry-season at all sites: (1) At CAX the dry-season G_s was close to 0.4 mmol m^{-2} s^{-1} and up to 1.4 mmol m^{-2} s^{-1} -- the highest G_s values were observed at this site; (2) at K34 and K67, the G_s gradually decreased from the transition wet-to-dry period to reach minimum values at the onset of the rainy season. (3) RJA experienced a reduction in G_s mid wet-season to mid dry-season (an all site minima of 3 mmol m^{-2} s^{-1}). Models were able to capture G_s at most forests, however they underestimated the amplitude of the annual cycle at K34 and CAX (Figure 7b). The tradeoff between losing water through transpiration and gaining carbon showed different patterns across sites, suggesting leaf-level adaptations and ecosystem-level variation. For example, seasonal G_s showed a negative relationship to incoming radiation at K34, RJA, and during the dry season of K67 (r^2 <0.3, p-value<0.01). By contrast, higher SW_{down} correlated to high G_s at the very seasonal forest of CAX (where we observed the highest wet-period rainfall values among the four forests) and during the wet-season at K67 (Figure 8b and S20). In general, G_s was positively related to precipitation (Figure S21).

The ratio between ecosystem carbon-uptake and transpiration-dominated *ET*, here presented as *WUE* was correlated to G_s at CAX (negative, r^2=0.25, p-value<0.01) and RJA (positive, r^2=0.48, p-value<0.01) (Figure S22). A significant regression was observed at K67 only if *WUE* was lagged 2-months (minimum *WUE* preceded minimum G_s) (Figure 7b). The *WUE* changes were non-significantly correlated to G_s at K34. Minimum *WUE* values were observed at the beginning of the dry season at equatorial sites (CAX, K34 and K67) and at the end of the dry period at RJA. The largest values of *WUE*, indicative of the highest photosynthetic rate per water use, were observed at different times for different sites when precipitation was > 100 mm month^{-1} (start of at K34 and K67 and end of the wet season at RJA all at ~2.6 gC mm^{-1}) (Figure 7c). Most models were able to correctly estimate seasonal values of *WUE* and G_s, some overestimating G_s values at K34 and *WUE* at K67.

We used the Bowen ratio to describe the dominant type of heat transfer across the forests -- where *LE* clearly dominated the turbulent flux (*H*<0.2 *LE*). The relationship between Bowen ratio and G_s showed that at relatively high Bowen values > 0.3, the G_s reached a minimum of ~0.35 mmol m^{-2} s^{-1} (no further reductions were observed) (Figure 8a).

4. Discussion

This study identified three main tropical forest properties (relationships among fluxes and between fluxes and vegetation characteristics) that if understood and implemented in LSMs equations and/or benchmarking exercises could reduce the differences between observations and model estimates of seasonal *ET, Rn* and *H* exchange: (1) Turbulent flux partitioning (e.g. high correlation between *Rn* and both turbulent fluxes, and nearly aseasonal Bowen ratio values), (2) representation of canopy reflectance and emissivity (e.g. albedo's annual cycle showed significantly lower absolute values and greater than expected amplitudes) and (3) endogenous ecosystem or physiology-related seasonality (e.g., leaf-level stomatal and *WUE* dynamics driven by leaf ontogeny and demography). These processes are related to surface energy properties, canopy-atmosphere water dynamics, their interactions, and more importantly the coupling between energy-carbon and water exchange. Here, we discuss some of our findings and suggest future observational and modeling work to improve simulations of tropical water and energy fluxes.

4.1. Determinants and distribution of net radiation into turbulent fluxes

Observations showed *ET* to be driven by radiation rather than by moisture availability as predicted by models. The R_n was able to explain more than 60% of the 16-day *LE* values and although we report a low r^2 for the *LE vs*. *Rn* regression at the southern forest of RJA, the coefficient of determination was driven by the low amplitude of the seasonal *LE* and *Rn* flux rather than the linear regressions not being able to predict *LE*.

Analysis of variability of the observed Bowen number annual cycle showed a nearly aseasonal ratio (~0.3 at the wet sites of K34 and CAX, and 0.21 at the dry sites K67 and RJA, Figure 4c). This suggests a proportional scaling of the forest's energy balance at each location (*H* was a constant fraction of *LE*). There was a relationship between the direction of bias in Bowen ratio estimates and site annual precipitation. LSMs overestimated dry-season Bowen values at the driest locations of K67 and RJA and underestimated the ratio at the wettest forests of K34 and CAX (models overestimated *LE* and underestimated *H*) (similar to Best et al., 2015; Haughton et al., 2016; Morales et al., 2005). The expectation of a higher Bowen ratio (increase importance of *H* over *LE*) at the drier sites did not apply at these tropical forests and could be explained by: (1) LSMs had a negative bias in dry-season *Rn*. (2) Models underestimated dry season *LE,* probably based on the incorrect assumption that water limitation (supply) rather than radiation (demand) drove the water flux (Federer, 1982). (3) LSMs may have difficulties simulating access to soil water at clay soils (e.g. K67) and although some recent model improvements have addressed this issue (e.g. ED2 see Longo et al., 2019a), measurements of field capacity and hydraulic conductivity were unavailable at our and other similar study sites. (4) Transpiration estimates may require to include processes related with plant hydraulics, like the addition of stem-water and other additional storage terms (e.g., CLM5 see Yan et al., 2020). (5) The time of rainfall, precipitation intensity and number of events (here we report significant differences among forest sites), rather than absolute precipitation values; may significantly influence the *H/LE* partition. Thus as rainfall characteristics and forest canopy structure (see item 6) can be key in defining how much water would be intercepted (directly evaporated), drained, and/or infiltrated (stored and later supplied). (6) Models may be assuming excess *E* from leaves surfaces (e.g. because of the high *LAI* forest values) and not enough water would be reaching the soil for infiltration during the wet season. This "water deficit" would be carried out into the dry season, limiting the moisture available for transpiration and artificially increasing *H*.

4.2. Representation of canopy reflectance (albedo) and thermal properties

Although significant, the differences between modeled-observed *ET* cannot be explained solely by the way models partition *H* and *LE* fluxes (Haughton et al., 2016). This study shows that correct turbulent flux estimations require reliable R_n estimates. Most LSMs were able to capture the seasonal cycle of R_n. Thus, SW_{down} was provided to all models as a meteorological driver and dominated R_n. However, at CAX and RJA, both model LW_{out} and SW_{out} were higher than observations and consequently, seasonal values of *Rn* were underestimated. In some instances, the model-observation alignment was the result of obtaining the right answer for the incorrect reasons (e.g. LSMs overestimated SW_{out} and underestimated LW_{out} at K34). Models that consistently estimated higher than observed LW_{out} values may have to address the following issues: (1) the vegetation storage pool/heat capacity may be too low and/or (2) underestimated transpiration values, both causing T_{skin} to be too high. Additional measurements (e.g. thermal cameras, sapflow sensors, soil moisture profiles, and H_2O isotopes) would be necessary to measure T_{skin}, to infer the relationships between *LE, H* and vegetation temperature and as to understand the mechanisms driving the relations between LW_{down} and LW_{out}.

Biases in LSMs *Rn* can also be attributed to SW_{out} calculations. Observed low albedos did contrast with model simulations resulting in more reflective (brighter) forest surfaces. Models underestimated the amount of canopy absorbed energy and may be imposing an “artificial” cooling effect. Surface albedo will be highly dependent on the leaf spectral properties and in general, canopy reflectance models relate higher *LAI* values to low albedo values (e.g. PROSAIL (Féret et al., 2017) assumes albedos ~0.2 for a *LAI*>4) or albedos are parameterized as a constant (Hollinger et al., 2010). Nevertheless, we observed opposite sign regressions between

LAI and albedo at CAX. Thus, indicating that α was not only driven by the quantity of leaves, but by leaf quality and vegetation reflective surfaces (e.g. wood and epiphylls) (Chavana-Bryant et al., 2016; Wu et al., 2017). Across the Amazon, leaf phenology has shown to be a key driver of *ET* and carbon uptake (Albert et al., 2018; Chen et al., 2020; Manoli et al., 2018; Restrepo-Coupe et al., 2013; Wu et al., 2017) and should be incorporated/improved on the derivation of energy, radiation and water fluxes, as well.

4.3. Ecosystem characteristics and their contributions to the water and energy flux seasonality

Our results showed that when the *H* was higher than 20% *LE*, the G_s reached a minimum of ~0.35 mmol m^{-2} s^{-1}, with no further reductions. Indicating that the vegetation continued to transpire at the same or higher rate under relatively high Bowen ratio conditions. This finding may be not surprising as Stahl et al. (2013) found that during low precipitation periods 50% of a sample of 65 large tropical trees relied on soil water below 1-m depth, and others have reported hydraulic redistribution, stem-water storage and additional processes that may explain forests access to water during the dry-season (Christoffersen et al., 2014; Oliveira et al., 2005; Yan et al., 2020). Moreover, the gradual dry season decrease in G_s (as similarly reported in Christoffersen et al. (2014) and Costa et al. (2010)) and increase in *LE* observed at the equatorial forests, highlights the very significant role of evaporation during this period. However, only seasonal inventories of leaf age and traits, and evaporation *vs.* transpiration measurements (e.g. H and O isotopes) will offer models validation data to avoid misrepresentation of the plant water exchange (e.g. under/over estimating photosynthesis and water use efficiency) (Lawrence et al., 2007).

Leaf-level stomatal conductance (g_s) is expected to maximize carbon uptake while also reducing water loss from leaves (or reducing the carbon cost of hydraulic failure) when water is limiting (Anderegg et al., 2018; Medlyn et al., 2011; Sperry et al., 2017), and generally is site-specific and driven by adaptation to the different atmospheric seasonal drivers (Brum et al., 2018). Ecosystem level vegetation controls (e.g. *LAI* and leaf age and position across the canopy profile) determine the water flux, rate of photosynthesis and the "acceptable" degree of water stress the forest can tolerate during the dry season (Albert et al., 2018; Restrepo-Coupe et al., 2013; Wu et al., 2017, 2017). Similar to G_s, at all four forests we observed contrasting degrees of seasonality in terms of *WUE* (with a range of ±25% of all year mean) and its timing metrics. Like *GEP*, across equatorial forests *WUE* increased as the dry season progressed and vice versa at RJA. At ecosystem scale we found that the regression between *WUE* and G_s was not statistically significant at K34 and K67, negatively correlated at CAX and positively at RJA (Figure S22). The lack of correlation between G_s and *WUE* would be driven by seasonal differences in intercellular CO_2 concentrations, atmospheric pressure and humidity, vegetation growth temperature and other canopy characteristics (Lin et al., 2015; Medlyn et al., 2011, 2012). For example, higher *VPD* can increase transpiration and reduce *WUE* without any change in G_s and vice versa.

4.4. Considerations for model improvement

This paper describes the seasonal patterns of different energy and water flux constituents and examines the relationships between them and different forest characteristics and climate variables at four tropical forests. We compared eddy covariance and biometric measurements to LSM simulations, as models represent our current understanding of the different atmosphere-biosphere processes at global and continental scales and are the ideal tool to predict vegetation responses to changes in climate. Our analysis highlights ***forest phenology*** as a significant driver of vegetation-atmosphere exchange and in particular, our data showed LSMs: (1) underestimated the amount of solar radiation the forests absorb and dry-season increases because we lack information regarding the relationship between leaf density and reflectance properties at high *LAI* values; (2) similarly, interception and direct evaporation may be overestimated at high *LAI* forests, and consequently LSMs may be underestimating infiltration and transpiration fluxes, overestimating canopy temperature, and consequently driving LSMs output (3) to inaccurate estimations of LW_{out} (e.g., reducing the soil moisture content and increased canopy temperature would lead to unrealistically high T_{skin} and hence incorrect estimates of LW_{out}) and SW_{out} (e.g. if we incorrectly characterize forest structure albedo will be too high). This seasonal bias on the outgoing flux (emissivity and albedo) dominated the model-observation *Rn* differences and will have an effect in the estimation of *H, LE* fluxes and the Bowen ratio. Our findings can be used to benchmark LSMs and develop more robust plant functional type parametrization. Improvements in model development will translate into better predictions of future surface-atmosphere exchange.

Acknowledgments

This research was funded by the Gordon and Betty Moore Foundation "Simulations from the Interactions between Climate, Forests, and Land Use in the Amazon Basin: Modeling and Mitigating Large Scale Savannization" project, the National Aeronautics and Space Administration (NASA) LBA CD-32, NASA LBA-DMIP project (NNX09AL52G), and NASA-ROSES (NNX17AF65G). N.R.C. acknowledges the support from the City of Toronto Children and Human Services, Dr. Debra Wunch, Dr. Dylan Jones, and the Department of Physics at the University of Toronto. B.O.C. was funded in part by the U.S. DOE (BER) NGEE-Tropics project to LANL. L.M.M acknowledges the UK Natural Environment Research Council funding (UK Earth System Modelling Project, UKESM, Grant NE/N017951/1). L.P.A. was supported by a Voss postdoctoral fellowship at the Institute at Brown for Environment and Society. M.L. was supported by the NASA postdoctoral program, administered by the Universities Space Research Association under contract with NASA. Research carried out at the JPL-California Institute of Technology, was under a contract with NASA. The authors would like to thank the staff of each tower site for their technical support and extensive fieldwork.

References

Abramowitz, G. (2005). Towards a benchmark for land surface models. *Geophysical Research Letters*, *32*(22). https://doi.org/10.1029/2005GL024419

Albert, L. P., Wu, J., Prohaska, N., Camargo, P. B. de, Huxman, T. E., Tribuzy, E. S., Ivanov, V. Y., Oliveira, R. S., Garcia, S., Smith, M. N., Junior, R. C. O., Restrepo‐Coupe, N., Silva, R. da, Stark, S. C., Martins, G. A., Penha, D. V., & Saleska, S. R. (2018). Age-dependent leaf physiology and consequences for crown-scale carbon uptake during the dry season in an Amazon evergreen forest. *New Phytologist*, *219*(3), 870–884. https://doi.org/10.1111/nph.15056

Anderegg, W. R. L., Wolf, A., Arango‐Velez, A., Choat, B., Chmura, D. J., Jansen, S., Kolb, T., Li, S., Meinzer, F. C., Pita, P., Dios, V. R. de, Sperry, J. S., Wolfe, B. T., & Pacala, S. (2018). Woody plants optimise stomatal behaviour relative to hydraulic risk. *Ecology Letters*, *21*(7), 968–977. https://doi.org/10.1111/ele.12962

Aragão, L. E. O. C., Malhi, Y., Barbier, N., Lima, A., Shimabukuro, Y., Anderson, L., & Saatchi, S. (2008). Interactions between rainfall, deforestation and fires during recent years in the Brazilian Amazonia. *Philosophical Transactions of the Royal Society of London B: Biological Sciences*, *363*(1498), 1779–1785. https://doi.org/10.1098/rstb.2007.0026

Aragão, L. E. O. C., Malhi, Y., Roman-Cuesta, R. M., Saatchi, S., Anderson, L. O., & Shimabukuro, Y. E. (2007). Spatial patterns and fire response of recent Amazonian droughts. *Geophysical Research Letters*, *34*, 5 PP. https://doi.org/200710.1029/2006GL028946

Baker, I. T., Prihodko, L., Denning, A. S., Goulden, M., Miller, S., & Rocha, H. R. da. (2008). Seasonal drought stress in the Amazon: Reconciling models and observations. *Journal of Geophysical Research*, *113*(G1), 1–10. https://doi.org/10.1029/2007JG000644

Baldocchi, D. D., Hincks, B. B., & Meyers, T. P. (1988). Measuring Biosphere-Atmosphere Exchanges of Biologically Related Gases with Micrometeorological Methods. *Ecology*, *69*(5), 1331–1340. https://doi.org/10.2307/1941631

Berry, J., Wolf, A., Campbell, J. E., Baker, I., Blake, N., Blake, D., Denning, A. S., Kawa, S. R., Montzka, S. A., Seibt, U., Stimler, K., Yakir, D., & Zhu, Z. (2013). A coupled model of the global cycles of carbonyl sulfide and CO2: A possible new window on the carbon cycle. *Journal of Geophysical Research: Biogeosciences*, *118*(2), 842–852. https://doi.org/10.1002/jgrg.20068

Best, M. J., Abramowitz, G., Johnson, H. R., Pitman, A. J., Balsamo, G., Boone, A., Cuntz, M., Decharme, B., Dirmeyer, P. A., Dong, J., Ek, M., Guo, Z., Haverd, V., van den Hurk, B. J. J., Nearing, G. S., Pak, B., Peters-Lidard, C., Santanello, J. A., Stevens, L., & Vuichard, N. (2015). The Plumbing of Land Surface Models: Benchmarking Model Performance. *Journal of Hydrometeorology*, *16*(3), 1425–1442. https://doi.org/10.1175/JHM-D-14-0158.1

Best, M. J., Pryor, M., Clark, D. B., Rooney, G. G., Essery, R. . L. H., Ménard, C. B., Edwards, J. M., Hendry, M. A., Porson, A., Gedney, N., Mercado, L. M., Sitch, S., Blyth, E., Boucher, O., Cox, P. M., Grimmond, C. S. B., & Harding, R. J. (2011). The Joint UK Land Environment Simulator (JULES), model description – Part 1: Energy and water fluxes. *Geosci. Model Dev.*, *4*(3), 677–699. https://doi.org/10.5194/gmd-4-677-2011

Bonan, G. B. (2008). Forests and Climate Change: Forcings, Feedbacks, and the Climate Benefits of Forests. *Science*, *320*(5882), 1444–1449. https://doi.org/10.1126/science.1155121

Bony, S., Bellon, G., Klocke, D., Sherwood, S., Fermepin, S., & Denvil, S. (2013). Robust direct effect of carbon dioxide on tropical circulation and regional precipitation. *Nature Geoscience*, *6*(6), 447–451. https://doi.org/10.1038/ngeo1799

Brando, P. M., Goetz, S. J., Baccini, A., Nepstad, D. C., Beck, P. S. A., & Christman, M. C. (2010). Seasonal and interannual variability of climate and vegetation indices across the

Amazon. *Proceedings of the National Academy of Sciences of the United States of America*, *107*(33), 14685–14690. https://doi.org/10.1073/pnas.0908741107

Brum, M., Vadeboncoeur, M. A., Ivanov, V., Asbjornsen, H., Saleska, S., Alves, L. F., Penha, D., Dias, J. D., Aragão, L. E. O. C., Barros, F., Bittencourt, P., Pereira, L., & Oliveira, R. S. (2018). Hydrological niche segregation defines forest structure and drought tolerance strategies in a seasonal Amazon forest. *Journal of Ecology*. https://doi.org/10.1111/1365-2745.13022

Brutsaert, W. (1982). *Evaporation Into the Atmosphere: Theory, History and Applications*. http://www.powells.com/biblio?isbn=9789027712479

Burba, G. (2010). *A brief practical guide to eddy covariance flux measurements: Principles and workflow examples for scientific and industrial applications /*. LI-COR,.

Castanho, A. D. de A., Galbraith, D., Zhang, K., Coe, M. T., Costa, M. H., & Moorcroft, P. (2016). Changing Amazon biomass and the role of atmospheric CO2 concentration, climate, and land use. *Global Biogeochemical Cycles*, *30*(1), 18–39. https://doi.org/10.1002/2015GB005135

Chagnon, F. J. F., & Bras, R. L. (2005). Contemporary climate change in the Amazon. *Geophysical Research Letters*, *32*(13), L13703. https://doi.org/10.1029/2005GL022722

Chavana-Bryant, C., Malhi, Y., Wu, J., Asner, G. P., Anastasiou, A., Enquist, B. J., Cosio Caravasi, E. G., Doughty, C. E., Saleska, S. R., Martin, R. E., & Gerard, F. F. (2016). Leaf aging of Amazonian canopy trees as revealed by spectral and physiochemical measurements. *The New Phytologist*. https://doi.org/10.1111/nph.13853

Chen, X., Maignan, F., Viovy, N., Bastos, A., Goll, D., Wu, J., Liu, L., Yue, C., Peng, S., Yuan, W., Conceição, A. C. da, O'Sullivan, M., & Ciais, P. (2020). Novel Representation of Leaf Phenology Improves Simulation of Amazonian Evergreen Forest Photosynthesis in a Land Surface Model. *Journal of Advances in Modeling Earth Systems*, *12*(1), e2018MS001565. https://doi.org/10.1029/2018MS001565

Christoffersen, B. O., Restrepo-Coupe, N., Arain, M. A., Baker, I. T., Cestaro, B. P., Ciais, P., Fisher, J. B., Galbraith, D., Guan, X., Gulden, L., van den Hurk, B., Ichii, K., Imbuzeiro, H., Jain, A., Levine, N., Miguez-Macho, G., Poulter, B., Roberti, D. R., Sakaguchi, K., … Saleska, S. R. (2014). Mechanisms of water supply and vegetation demand govern the seasonality and magnitude of evapotranspiration in Amazonia and Cerrado. *Agricultural and Forest Meteorology*, *191*(0), 33–50. https://doi.org/10.1016/j.agrformet.2014.02.008

Clark, D. B., Mercado, L. M., Sitch, S., Jones, C. D., Gedney, N., Best, M. J., Pryor, M., Rooney, G. G., Essery, R. L. H., Blyth, E., Boucher, O., Harding, R. J., Huntingford, C., & Cox, P. M. (2011). The Joint UK Land Environment Simulator (JULES), model description – Part 2: Carbon fluxes and vegetation dynamics. *Geosci. Model Dev.*, *4*(3), 701–722. https://doi.org/10.5194/gmd-4-701-2011

Costa, M. H., Biajoli, M. C., Sanches, L., Malhado, A. C. M., Hutyra, L. R., Rocha, H. R. da, Aguiar, R. G., & Araújo, A. C. de. (2010). Atmospheric versus vegetation controls of Amazonian tropical rain forest evapotranspiration: Are the wet and seasonally dry rain forests any different? *Journal of Geophysical Research: Biogeosciences*, *115*(G4). https://doi.org/10.1029/2009JG001179

da Rocha, H. R., Goulden, M. L., Miller, S. D., Menton, M. C., Pinto, L. D. V. O., de Freitas, H. C., & e Silva Figueira, A. M. (2004). Seasonality of Water and Heat Fluxes over a

Tropical Forest in Eastern Amazonia. *Ecological Applications*, *14*(sp4), 22–32. https://doi.org/10.1890/02-6001

da Rocha, H. R., Manzi, A. O., Cabral, O. M., Miller, S. D., Goulden, M. L., Saleska, S. R., R.-Coupe, N., Wofsy, S. C., Borma, L. S., Artaxo, P., Vourlitis, G., Nogueira, J. S., Cardoso, F. L., Nobre, A. D., Kruijt, B., Freitas, H. C., von Randow, C., Aguiar, R. G., & Maia, J. F. (2009). Patterns of water and heat flux across a biome gradient from tropical forest to savanna in Brazil. *Journal of Geophysical Research: Biogeosciences*, *114*(G1), G00B12. https://doi.org/10.1029/2007JG000640

Davidson, E. A., de Araújo, A. C., Artaxo, P., Balch, J. K., Brown, I. F., C. Bustamante, M. M., Coe, M. T., DeFries, R. S., Keller, M., Longo, M., Munger, J. W., Schroeder, W., Soares-Filho, B. S., Souza, C. M., & Wofsy, S. C. (2012). The Amazon basin in transition. *Nature*, *481*(7381), 321–328. https://doi.org/10.1038/nature10717

de Goncalves, L. G. de, Baker, I., Christoffersen, B., Costa, M., Restrepo-Coupe, N., Rocha, H. da, Saleska, S., & Nobre Muza, M. (2009). *The Large Scale Biosphere-Atmosphere Experiment in Amazônia, Model Intercomparison Project (LBA-MIP) protocol*.

Eva, H. D., & Huber (eds), O. (2005). *A Proposal for Defining the Geographical Boundaries of Amazonia: Synthesis of the results from an Expert Consultation Workshop organized by the European Commission in collaboration with the Amazon Cooperation Treaty Organization—JRC Ispra, 7-8 June 2005*. Office for Official Publications of the European Communities, Luxemburg.

Federer, C. A. (1982). Transpirational supply and demand: Plant, soil, and atmospheric effects evaluated by simulation. *Water Resources Research*, *18*(2), 355–362.

https://doi.org/10.1029/WR018i002p00355

Féret, J.-B., Gitelson, A. A., Noble, S. D., & Jacquemoud, S. (2017). PROSPECT-D: Towards modeling leaf optical properties through a complete lifecycle. *Remote Sensing of Environment*, *193*, 204–215. https://doi.org/10.1016/j.rse.2017.03.004

Fisher, J. B., Huntzinger, D. N., Schwalm, C. R., & Sitch, S. (2014). Modeling the Terrestrial Biosphere. *Annual Review of Environment and Resources*, *39*(1), 91–123. https://doi.org/10.1146/annurev-environ-012913-093456

Fisher, R. A., Koven, C. D., Anderegg, W. R. L., Christoffersen, B. O., Dietze, M. C., Farrior, C. E., Holm, J. A., Hurtt, G. C., Knox, R. G., Lawrence, P. J., Lichstein, J. W., Longo, M., Matheny, A. M., Medvigy, D., Muller‐Landau, H. C., Powell, T. L., Serbin, S. P., Sato, H., Shuman, J. K., … Moorcroft, P. R. (2018). Vegetation demographics in Earth System Models: A review of progress and priorities. *Global Change Biology*, *24*(1), 35–54. https://doi.org/10.1111/gcb.13910

Fisher, R. A., Williams, M., Costa, D., Lola, A., Malhi, Y., Costa, D., F, R., Almeida, S., & Meir, P. (2007). The response of an Eastern Amazonian rain forest to drought stress: Results and modelling analyses from a throughfall exclusion experiment. *Global Change Biology*, *13*(11), 2361–2378. https://doi.org/10.1111/j.1365-2486.2007.01417.x

Foken, T. (2008). The energy balance closure problem: An overview. *Ecological Applications: A Publication of the Ecological Society of America*, *18*(6), 1351–1367.

Foken, T., Aubinet, M., & Leuning, R. (2012). The Eddy Covariance Method. In M. Aubinet, T. Vesala, & D. Papale (Eds.), *Eddy Covariance* (pp. 1–19). Springer Netherlands. https://doi.org/10.1007/978-94-007-2351-1_1

Foley, J. A., Prentice, I. C., Ramankutty, N., Levis, S., Pollard, D., Sitch, S., & Haxeltine, A. (1996). An integrated biosphere model of land surface processes, terrestrial carbon balance, and vegetation dynamics. *Global Biogeochemical Cycles*, *10*(4), 603–628. https://doi.org/10.1029/96GB02692

Freire, G. A. P., Ventura, D. J., Fotopoulos, I. G., Rosa, D. M., Aguiar, R. G., & Araújo, A. C. de. (2020). DINÂMICA DE SERAPILHEIRA EM UMA ÁREA DE FLORESTA DE TERRA FIRME, AMAZÔNIA OCIDENTAL. *Nativa*, *8*(3), 323–328. https://doi.org/10.31413/nativa.v8i3.9155

Fu, R., Yin, L., Li, W., Arias, P. A., Dickinson, R. E., Huang, L., Chakraborty, S., Fernandes, K., Liebmann, B., Fisher, R., & Myneni, R. B. (2013). Increased dry-season length over southern Amazonia in recent decades and its implication for future climate projection. *Proceedings of the National Academy of Sciences*, *110*(45), 18110–18115. https://doi.org/10.1073/pnas.1302584110

Getirana, A. C. V., Dutra, E., Guimberteau, M., Kam, J., Li, H.-Y., Decharme, B., Zhang, Z., Ducharne, A., Boone, A., Balsamo, G., Rodell, M., Toure, A. M., Xue, Y., Peters-Lidard, C. D., Kumar, S. V., Arsenault, K., Drapeau, G., Ruby Leung, L., Ronchail, J., & Sheffield, J. (2014). Water Balance in the Amazon Basin from a Land Surface Model Ensemble. *Journal of Hydrometeorology*, *15*(6), 2586–2614. https://doi.org/10.1175/JHM-D-14-0068.1

Gotangco Castillo, C. K., Levis, S., & Thornton, P. (2012). Evaluation of the New CNDV Option of the Community Land Model: Effects of Dynamic Vegetation and Interactive Nitrogen on CLM4 Means and Variability*. *Journal of Climate*, *25*(11), 3702–3714.

https://doi.org/10.1175/JCLI-D-11-00372.1

Goudriaan, J. (1986). A simple and fast numerical method for the computation of daily totals of crop photosynthesis. *Agricultural and Forest Meteorology*, *38*(1–3), 249–254. https://doi.org/doi: DOI: 10.1016/0168-1923(86)90063-8

Hagos, S., & Leung, L. R. (2011). On the Relationship between Uncertainties in Tropical Divergence and the Hydrological Cycle in Global Models. *Journal of Climate*, *25*(1), 381–391. https://doi.org/10.1175/JCLI-D-11-00058.1

Harper, A. B., Denning, A. S., Baker, I. T., Branson, M. D., Prihodko, L., & Randall, D. A. (2010). Role of deep soil moisture in modulating climate in the Amazon rainforest. *Geophysical Research Letters*, *37*(5). https://doi.org/10.1029/2009GL042302

Haughton, N., Abramowitz, G., Pitman, A. J., Or, D., Best, M. J., Johnson, H. R., Balsamo, G., Boone, A., Cuntz, M., Decharme, B., Dirmeyer, P. A., Dong, J., Ek, M., Guo, Z., Haverd, V., van den Hurk, B. J. J., Nearing, G. S., Pak, B., Santanello, J. A., … Vuichard, N. (2016). The Plumbing of Land Surface Models: Is Poor Performance a Result of Methodology or Data Quality? *Journal of Hydrometeorology*, *17*(6), 1705–1723. https://doi.org/10.1175/JHM-D-15-0171.1

Held, I. M., & Soden, B. J. (2006). Robust Responses of the Hydrological Cycle to Global Warming. *Journal of Climate*, *19*(21), 5686–5699. https://doi.org/10.1175/JCLI3990.1

Hollinger, D. Y., Ollinger, S. V., Richardson, A. D., Meyers, T. P., Dail, D. B., Martin, M. E., Scott, N. A., Arkebauer, T. J., Baldocchi, D. D., Clark, K. L., Curtis, P. S., Davis, K. J., Desai, A. R., Dragoni, D., Goulden, M. L., Gu, L., Katul, G. G., Pallardy, S. G., U, K. T. P., … Verma, S. B. (2010). Albedo estimates for land surface models and support for a new paradigm based on foliage nitrogen concentration. *Global Change Biology*, *16*(2), 696–710. https://doi.org/10.1111/j.1365-2486.2009.02028.x

Jasechko, S., Sharp, Z. D., Gibson, J. J., Birks, S. J., Yi, Y., & Fawcett, P. J. (2013). Terrestrial water fluxes dominated by transpiration. *Nature*, *496*(7445), 347–350. https://doi.org/10.1038/nature11983

Jin, M., & Liang, S. (2006). An Improved Land Surface Emissivity Parameter for Land Surface Models Using Global Remote Sensing Observations. *Journal of Climate*, *19*(12), 2867–2881. https://doi.org/10.1175/JCLI3720.1

Kato, S., Loeb, N. G., Rose, F. G., Doelling, D. R., Rutan, D. A., Caldwell, T. E., Yu, L., & Weller, R. A. (2012). Surface Irradiances Consistent with CERES-Derived Top-of-Atmosphere Shortwave and Longwave Irradiances. *Journal of Climate*, *26*(9), 2719–2740. https://doi.org/10.1175/JCLI-D-12-00436.1

Keller, M., Alencar, A., Asner, G. P., Bobby Braswell, Bustamante, M., Davidson, E., Feldpausch, T., Fernandes, E., Goulden, M., Kabat, P., Kruijt, B., Luizão, F., Miller, S., Markewitz, D., Nobre, A. D., Nobre, C. A., Filho, N. P., Rocha, H. da, Dias, P. S., … Vourlitis, G. L. (2004). Ecological Research in the Large-Scale Biosphere-Atmosphere Experiment in Amazonia: Early Results. *Ecological Applications*, *14*(4), S3–S16.

Kucharik, C. J., Foley, J. A., Delire, C., Fisher, V. A., Coe, M. T., Lenters, J. D., Young‐Molling, C., Ramankutty, N., Norman, J. M., & Gower, S. T. (2000). Testing the performance of a dynamic global ecosystem model: Water balance, carbon balance, and vegetation structure. *Global Biogeochemical Cycles*, *14*(3), 795–825. https://doi.org/10.1029/1999GB001138

Lawrence, D. M., Thornton, P. E., Oleson, K. W., & Bonan, G. B. (2007). The Partitioning of Evapotranspiration into Transpiration, Soil Evaporation, and Canopy Evaporation in a GCM: Impacts on Land–Atmosphere Interaction. *Journal of Hydrometeorology*, *8*(4), 862–880. https://doi.org/10.1175/JHM596.1

Lee, J.-E., Oliveira, R. S., Dawson, T. E., & Fung, I. (2005). Root functioning modifies seasonal climate. *Proceedings of the National Academy of Sciences*, *102*(49), 17576–17581. https://doi.org/10.1073/pnas.0508785102

Li, Y., Zhao, M., Motesharrei, S., Mu, Q., Kalnay, E., & Li, S. (2015). Local cooling and warming effects of forests based on satellite observations. *Nature Communications*, *6*(1), 6603. https://doi.org/10.1038/ncomms7603

Lin, Y.-S., Medlyn, B. E., Duursma, R. A., Prentice, I. C., Wang, H., Baig, S., Eamus, D., Dios, V. R. de, Mitchell, P., Ellsworth, D. S., Beeck, M. O. de, Wallin, G., Uddling, J., Tarvainen, L., Linderson, M.-L., Cernusak, L. A., Nippert, J. B., Ocheltree, T. W., Tissue, D. T., … Wingate, L. (2015). Optimal stomatal behaviour around the world. *Nature Climate Change*, *5*(5), 459–464. https://doi.org/10.1038/nclimate2550

Liou, K. N. (2002). *An Introduction to Atmospheric Radiation* (2nd ed., Vol. 84). Academic Press. https://www.elsevier.com/books/an-introduction-to-atmospheric-radiation/liou/978-0-12-451451-5

Liu, Z., Ballantyne, A. P., & Cooper, L. A. (2019). Biophysical feedback of global forest fires on surface temperature. *Nature Communications*, *10*(1), 214. https://doi.org/10.1038/s41467-018-08237-z

Longo, M., Knox, R. G., Levine, N. M., Alves, L. F., Bonal, D., Camargo, P. B., Fitzjarrald, D. R., Hayek, M. N., Restrepo‐Coupe, N., Saleska, S. R., Silva, R. da, Stark, S. C., Tapajós, R. P., Wiedemann, K. T., Zhang, K., Wofsy, S. C., & Moorcroft, P. R. (2018). Ecosystem heterogeneity and diversity mitigate Amazon forest resilience to frequent extreme droughts. *New Phytologist*, *219*(3), 914–931. https://doi.org/10.1111/nph.15185

Longo, M., Knox, R. G., Levine, N. M., Swann, A. L. S., Medvigy, D. M., Dietze, M. C., Kim, Y., Zhang, K., Bonal, D., Burban, B., Camargo, P. B., Hayek, M. N., Saleska, S. R., Silva, R. da, Bras, R. L., Wofsy, S. C., & Moorcroft, P. R. (2019). The biophysics, ecology, and biogeochemistry of functionally diverse, vertically and horizontally heterogeneous ecosystems: The Ecosystem Demography model, version 2.2 – Part 2: Model evaluation for tropical South America. *Geoscientific Model Development*, *12*(10), 4347–4374. https://doi.org/10.5194/gmd-12-4347-2019

Longo, M., Knox, R. G., Medvigy, D. M., Levine, N. M., Dietze, M. C., Kim, Y., Swann, A. L. S., Zhang, K., Rollinson, C. R., Bras, R. L., Wofsy, S. C., & Moorcroft, P. R. (2019). The biophysics, ecology, and biogeochemistry of functionally diverse, vertically and horizontally heterogeneous ecosystems: The Ecosystem Demography model, version 2.2 – Part 1: Model description. *Geoscientific Model Development*, *12*(10), 4309–4346. https://doi.org/10.5194/gmd-12-4309-2019

Lopes, A. P., Nelson, B. W., Wu, J., Graça, P. M. L. de A., Tavares, J. V., Prohaska, N., Martins, G. A., & Saleska, S. R. (2016). Leaf flush drives dry season green-up of the Central Amazon. *Remote Sensing of Environment*, *182*, 90–98. https://doi.org/10.1016/j.rse.2016.05.009

Manoli, G., Ivanov, V. Y., & Fatichi, S. (2018). Dry-Season Greening and Water Stress in Amazonia: The Role of Modeling Leaf Phenology. *Journal of Geophysical Research: Biogeosciences*, *123*(6), 1909–1926. https://doi.org/10.1029/2017JG004282

Mauder, M., Genzel, S., Fu, J., Kiese, R., Soltani, M., Steinbrecher, R., Zeeman, M., Banerjee, T., Roo, F. D., & Kunstmann, H. (2018). Evaluation of energy balance closure adjustment methods by independent evapotranspiration estimates from lysimeters and hydrological simulations. *Hydrological Processes*, *32*(1), 39–50. https://doi.org/10.1002/hyp.11397

Medlyn, B. E., Duursma, R. A., Eamus, D., Ellsworth, D. S., Prentice, I. C., Barton, C. V. M., Crous, K. Y., Angelis, P. de, Freeman, M., & Wingate, L. (2012). Reconciling the optimal and empirical approaches to modelling stomatal conductance. *Global Change Biology*, *18*(11), 3476–3476. https://doi.org/10.1111/j.1365-2486.2012.02790.x

Medlyn, B. E., Duursma, R. A., Eamus, D., Ellsworth, D. S., Prentice, I. C., Barton, C. V. M., Crous, K. Y., Angelis, P. D., Freeman, M., & Wingate, L. (2011). Reconciling the optimal and empirical approaches to modelling stomatal conductance. *Global Change Biology*, *17*(6), 2134–2144. https://doi.org/10.1111/j.1365-2486.2010.02375.x

Medvigy, D., Wofsy, S. C., Munger, J. W., Hollinger, D. Y., & Moorcroft, P. R. (2009). Mechanistic scaling of ecosystem function and dynamics in space and time: Ecosystem Demography model version 2. *Journal of Geophysical Research: Biogeosciences*, *114*(G1), G01002. https://doi.org/10.1029/2008JG000812

Metcalfe, D. B., Meir, P., Aragão, L. E. O. C., Malhi, Y., Costa, A. C. L. da, Braga, A., Gonçalves, P. H. L., Athaydes, J. de, Almeida, S. S. de, & Williams, M. (2007). Factors controlling spatio-temporal variation in carbon dioxide efflux from surface litter, roots, and soil organic matter at four rain forest sites in the eastern Amazon. *Journal of Geophysical Research*, *112*(G4), 1–9. https://doi.org/200710.1029/2007JG000443

Moderow, U., Aubinet, M., Feigenwinter, C., Kolle, O., Lindroth, A., Mölder, M., Montagnani, L., Rebmann, C., & Bernhofer, C. (2009). Available energy and energy balance closure at four coniferous forest sites across Europe. *Theoretical and Applied Climatology*, *98*(3), 397–412. https://doi.org/10.1007/s00704-009-0175-0

Morales, P., Sykes, M. T., Prentice, I. C., Smith, P., Smith, B., Bugmann, H., Zierl, B., Friedlingstein, P., Viovy, N., Sabaté, S., Sánchez, A., Pla, E., Gracia, C. A., Sitch, S., Arneth, A., & Ogee, J. (2005). Comparing and evaluating process-based ecosystem model predictions of carbon and water fluxes in major European forest biomes. *Global Change Biology*, *11*(12), 2211–2233. https://doi.org/10.1111/j.1365-2486.2005.01036.x

NASA. (2019). *Clouds and the Earth's Radiant Energy System Information and Data (CERES)*. http://ceres.larc.nasa.gov/

Oleson, K. W., Niu, G.-Y., Yang, Z.-L., Lawrence, D. M., Thornton, P. E., Lawrence, P. J., Stöckli, R., Dickinson, R. E., Bonan, G. B., Levis, S., Dai, A., & Qian, T. (2008). Improvements to the Community Land Model and their impact on the hydrological cycle. *Journal of Geophysical Research*, *113*(G1), 1–26. https://doi.org/10.1029/2007JG000563

Oliveira, R. S., Dawson, T. E., Burgess, S. S. O., & Nepstad, D. C. (2005). Hydraulic redistribution in three Amazonian trees. *Oecologia*, *145*(3), 354–363. https://doi.org/10.1007/s00442-005-0108-2

Peters, T. (2016). Water Balance in Tropical Regions. In L. Pancel & M. Köhl (Eds.), *Tropical Forestry Handbook* (pp. 391–403). Springer.

https://doi.org/10.1007/978-3-642-54601-3_40

Pitman, A. J. (2003). The evolution of, and revolution in, land surface schemes designed for climate models. *International Journal of Climatology*, *23*(5), 479–510. https://doi.org/10.1002/joc.893

Powell, T. L., Galbraith, D. R., Christoffersen, B. O., Harper, A., Imbuzeiro, H. M. A., Rowland, L., Almeida, S., Brando, P. M., da Costa, A. C. L., Costa, M. H., Levine, N. M., Malhi, Y., Saleska, S. R., Sotta, E., Williams, M., Meir, P., & Moorcroft, P. R. (2013). Confronting model predictions of carbon fluxes with measurements of Amazon forests subjected to experimental drought. *New Phytologist*, *200*(2), 350–365. https://doi.org/10.1111/nph.12390

Reed, D. E., Frank, J. M., Ewers, B. E., & Desai, A. R. (2018). Time dependency of eddy covariance site energy balance. *Agricultural and Forest Meteorology*, *249*, 467–478. https://doi.org/10.1016/j.agrformet.2017.08.008

Restrepo-Coupe, N., da Rocha, H. R., da Araujo, A. C., Borma, L. S., Christoffersen, B., Cabral, O. M. R., de Camargo, P. B., Cardoso, F. L., da Costa, A. C. L., Fitzjarrald, D. R., Goulden, M. L., Kruijt, B., Maia, J. M. F., Malhi, Y. S., Manzi, A. O., Miller, S. D., Nobre, A. D., von Randow, C., Sá, L. D. A., … Saleska, S. R. (2013). What drives the seasonality of photosynthesis across the Amazon basin? A cross-site analysis of eddy flux tower measurements from the Brasil flux network. *Agricultural and Forest Meteorology*, *182–183*, 128–144.

Restrepo-Coupe, N., Levine, N. M., Christoffersen, B. O., Albert, L. P., Wu, J., Costa, M. H., Galbraith, D., Imbuzeiro, H., Martins, G., da Araujo, A. C., Malhi, Y. S., Zeng, X., Moorcroft, P., & Saleska, S. R. (2017). Do dynamic global vegetation models capture the seasonality of carbon fluxes in the Amazon basin? A data-model intercomparison. *Global Change Biology*, *23*(1), 191–208. https://doi.org/10.1111/gcb.13442

Rice, A. H., Pyle, E. H., Saleska, S. R., Hutyra, L. R., Palace, M., Keller, M., Camargo, P. B. de, Portilho, K., Marques, D. F., & Wofsy, S. C. (2004). Carbon balance and vegetation dynamics in an old-growth Amazonian forest. *Ecological Applications*, *14*(4), S55–S71.

Sellers, P. J. (1985). Canopy reflectance, photosynthesis and transpiration. *International Journal of Remote Sensing*, *6*(8), 1335–1372. https://doi.org/10.1080/01431168508948283

Sena, E. T., Dias, M. A. F. S., Carvalho, L. M. V., & Dias, P. L. S. (2018). Reduced Wet-Season Length Detected by Satellite Retrievals of Cloudiness over Brazilian Amazonia: A New Methodology. *Journal of Climate*, *31*(24), 9941–9964. https://doi.org/10.1175/JCLI-D-17-0702.1

Shuttleworth, W. J. (1988). Evaporation from Amazonian Rainforest. *Proceedings of the Royal Society of London. Series B, Biological Sciences*, *233*(1272), 321–346.

Silva Dias, M. a. F., Rutledge, S., Kabat, P., Silva Dias, P. L., Nobre, C., Fisch, G., Dolman, A. J., Zipser, E., Garstang, M., Manzi, A. O., Fuentes, J. D., Rocha, H. R., Marengo, J., Plana-Fattori, A., Sá, L. D. A., Alvalá, R. . c. S., Andreae, M. O., Artaxo, P., Gielow, R., & Gatti, L. (2002). Cloud and rain processes in a biosphere-atmosphere interaction context in the Amazon Region. *Journal of Geophysical Research: Atmospheres*, *107*(D20), 8072. https://doi.org/10.1029/2001JD000335

Sperry, J. S., Venturas, M. D., Anderegg, W. R. L., Mencuccini, M., Mackay, D. S., Wang, Y., & Love, D. M. (2017). Predicting stomatal responses to the environment from the optimization of photosynthetic gain and hydraulic cost. *Plant, Cell & Environment*, *40*(6), 816–830. https://doi.org/10.1111/pce.12852

Spracklen, D. V., Baker, J. C. A., Garcia-Carreras, L., & Marsham, J. H. (2018). The Effects of Tropical Vegetation on Rainfall. *Annual Review of Environment and Resources*, *43*(1), 193–218. https://doi.org/10.1146/annurev-environ-102017-030136

Stahl, C., Hérault, B., Rossi, V., Burban, B., Bréchet, C., & Bonal, D. (2013). Depth of soil water uptake by tropical rainforest trees during dry periods: Does tree dimension matter? *Oecologia*, *173*(4), 1191–1201. https://doi.org/10.1007/s00442-013-2724-6

Stockli, R., Rutishauser, T., Dragoni, D., O'Keefe, J., Thornton, P., Jolly, M., Lu, L., & Denning, A. (2008). Remote sensing data assimilation for a prognostic phenology model. *Journal of Geophysical Research-Biogeosciences*, *113*(G4). https://doi.org/10.1029/2008JG000781

Tan, Z.-H., Zhao, J.-F., Wang, G.-Z., Chen, M.-P., Yang, L.-Y., He, C.-S., Restrepo-Coupe, N., Peng, S.-S., Liu, X.-Y., da Rocha, H. R., Kosugi, Y., Hirano, T., Saleska, S. R., Goulden, M. L., Zeng, J., Ding, F.-J., Gao, F., & Song, L. (2019). Surface conductance for evapotranspiration of tropical forests: Calculations, variations, and controls. *Agricultural and Forest Meteorology*, *275*, 317–328. https://doi.org/10.1016/j.agrformet.2019.06.006

Taylor, K. E. (2001). Summarizing multiple aspects of model performance in a single diagram. *Journal of Geophysical Research*, *106*(D7), PP. 7183-7192. https://doi.org/200110.1029/2000JD900719

Trenberth, K. E., Fasullo, J. T., & Kiehl, J. (2009). Earth's Global Energy Budget. *Bulletin of the American Meteorological Society*, *90*(3), 311–324.

https://doi.org/10.1175/2008BAMS2634.1

Wan, Z., Hook, S., & Hulley, G. (2015). MOD11A2 MODIS/Terra Land Surface Temperature/Emissivity 8-Day L3 Global 1km SIN Grid V006. *Distributed by NASA EOSDIS Land Processes DAAC*. https://doi.org/10.5067/MODIS/MOD11A2.006

Wehr, R., & Saleska, S. R. (2015). An improved isotopic method for partitioning net ecosystem–atmosphere CO2 exchange. *Agricultural and Forest Meteorology*, *214–215*, 515–531. https://doi.org/10.1016/j.agrformet.2015.09.009

Wehr, Richard, & Saleska, S. R. (2020). Calculating Canopy Stomatal Conductance from Eddy Covariance Measurements, in Light of the Energy Budget Closure Problem. *Biogeosciences Discussions*, 1–16. https://doi.org/10.5194/bg-2020-154

Wehr, Richard, & Saleska, S. R. (2021). Calculating canopy stomatal conductance from eddy covariance measurements, in light of the energy budget closure problem. *Biogeosciences*, *18*(1), 13–24. https://doi.org/10.5194/bg-18-13-2021

Wei, Z., Yoshimura, K., Wang, L., Miralles, D. G., Jasechko, S., & Lee, X. (2017). Revisiting the contribution of transpiration to global terrestrial evapotranspiration. *Geophysical Research Letters*, *44*(6), 2792–2801. https://doi.org/10.1002/2016GL072235

Wilson, K., Goldstein, A., Falge, E., Aubinet, M., Baldocchi, D., Berbigier, P., Bernhofer, C., Ceulemans, R., Dolman, H., Field, C., Grelle, A., Ibrom, A., Law, B. E., Kowalski, A., Meyers, T., Moncrieff, J., Monson, R., Oechel, W., Tenhunen, J., … Verma, S. (2002). Energy balance closure at FLUXNET sites. *Agricultural and Forest Meteorology*, *113*(1–4), 223–243. https://doi.org/10.1016/S0168-1923(02)00109-0

Wofsy, S., Goulden, M., & Munger, J. W. (1993). Net Exchange of CO2 in a Mid-Latitude

Forest. *Science*, *260*, 1314–1317.

Worden, J., Noone, D., Bowman, K., Beer, R., Eldering, A., Fisher, B., Gunson, M., Goldman, A., Herman, R., Kulawik, S. S., Lampel, M., Osterman, G., Rinsland, C., Rodgers, C., Sander, S., Shephard, M., Webster, C. R., & Worden, H. (2007). Importance of rain evaporation and continental convection in the tropical water cycle. *Nature*, *445*(7127), 528–532. https://doi.org/10.1038/nature05508

Wu, J., Guan, K., Hayek, M., Restrepo-Coupe, N., Wiedemann, K. T., Xu, X., Wehr, R., Christoffersen, B. O., Miao, G., da Silva, R., de Araujo, A. C., Oliviera, R. C., Camargo, P. B., Monson, R. K., Huete, A. R., & Saleska, S. R. (2017). Partitioning controls on Amazon forest photosynthesis between environmental and biotic factors at hourly to interannual timescales. *Global Change Biology*, *23*(3), 1240–1257. https://doi.org/10.1111/gcb.13509

Yan, B., Mao, J., Dickinson, R. E., Thornton, P. E., Shi, X., Ricciuto, D. M., Warren, J. M., & Hoffman, F. M. (2020). Modelling tree stem-water dynamics over an Amazonian rainforest. *Ecohydrology*, *13*(1), e2180. https://doi.org/10.1002/eco.2180

Yanagi, S. N. M., & Costa, M. H. (2011). Simulations of tropical rainforest albedo: Is canopy wetness important? *Anais Da Academia Brasileira de Ciências*, *83*(4), 1171–1180. https://doi.org/10.1590/S0001-37652011005000047

List of Figures

Figure 1. Parameters and mechanisms that govern ecosystem water fluxes (evapotranspiration) and their seasonality included in this study. Here classified as: water availability, vegetation response, radiation balance, and distribution of turbulent fluxes. Colored lines show which drivers interact with which parameters/mechanisms.

Figure 2. Locations of eddy covariance tower study sites in the Amazon Basin *sensu-stricto* (Eva & Huber (eds), 2005). Mean monthly net radiation (W m^{-2}) from the Clouds and the Earth's Radiant Energy System v4.0 (CERES) (Kato et al., 2012) for the years 2003 to 2018 (NASA, 2019).

Figure 3. Annual cycle 16-day average observed climatic drivers (a) precipitation (*Precip;* mm $month^{-1}$) (gray bars), air temperature (T_{air}; degC) (blue line left y-axis) and (b) incoming shortwave (SW_{down}; W m^{-2}) (black line right y-axis) and longwave radiation (LW_{down}; W m^{-2}) (blue line left y-axis). (c) Modeled and observed daytime evapotranspiration (ET_{day}, mm $month^{-1}$), dashed line corresponds to the reference evapotranspiration (model *ET* driven only by meteorology); and (d) model ecosystem-scale of model soil moisture 'stress' (*FSW*, where 1 = no stress). From left to right study sites (from wettest to driest) near Manaus (K34), Caxiuanã (CAX), Santarém (K67), and Reserva Jaru southern (RJA) forests. Gray-shaded area is dry season as defined using satellite-derived measures of precipitation (TRMM: 1998-2018). (e) Right hand plots correspond to Taylor diagrams for a statistical summary of model (color coded) fluxes compared to observations of seasonal fluxes (16-day). Missing sites indicate that the

model overestimates the seasonality of observations; the ratio between model (σ_m) to observation standard deviations (σ) is >2. Simulations from ED2 (blue), IBIS (red), CLM3.5 (green), and JULES (purple).

Figure 4. Annual cycle 16-day average observations (black line) and modeled (color lines) of (a) latent heat flux (*LE*; W m^{-2}) -- energy equivalent of evapotranspiration (*ET*; mm d^{-1}), and model results from a linear regression between *LE* and *Rn* (dashed black line). (b) Sensible heat flux (*H*; W m^{-2}) and (c) unitless Bowen ratio (*Bowen* = *H/LE*). From left to right study sites (from wettest to driest) near Manaus (K34), Caxiuanã (CAX), Santarém (K67), and Reserva Jaru southern (RJA) forests. Gray-shaded area is dry season as defined using satellite-derived measures of precipitation (TRMM: 1998-2018). Right hand plots correspond to Taylor diagrams for a statistical summary of model (color coded) fluxes compared to observations of seasonal fluxes (16-day). Missing sites indicate that the model overestimates the seasonality of observations; the ratio between model (σ_m) to observation standard deviations (σ) is >2. Simulations from ED2 (blue), IBIS (red), CLM3.5 (green), and JULES (purple).

Figure 5. Annual cycle 16-day average observations (black line) and modeled (color lines) of (a) outgoing shortwave radiation (SW_{out}; W m^{-2}); (b) outgoing longwave radiation (LW_{out}; W m^{-2}) and (c) net radiation (R_n; W m^{-2}) (black continuous line) and the sum of turbulent fluxes, sensible plus latent heat flux (*H*+*LE*; W m^{-2}) (black dotted line). From left to right study sites (from wettest to driest) near Manaus (K34), Caxiuanã (CAX), Santarém (K67), and Reserva Jaru southern (RJA) forests. Gray-shaded area is dry season as defined using satellite-derived

measures of precipitation (TRMM: 1998-2018). Right hand plots correspond to Taylor diagrams for a statistical summary of model (color coded) fluxes compared to observations of seasonal fluxes (16-day). Missing sites indicate that the model overestimates the seasonality of observations; the ratio between model (σ_m) to observation standard deviations (σ) is >2. Simulations from ED2 (blue), IBIS (red), CLM3.5 (green), and JULES (purple).

Figure 6. Annual cycle 16-day average observations (black line) and modeled (color lines) of (a) albedo -- the ratio of outgoing to incoming shortwave radiation ($\alpha = SW_{out} / SW_{down}$), and (b) surface emissivity (ε_s). From left to right study sites (from wettest to driest) near Manaus (K34), Caxiuanã (CAX), Santarém (K67), and Reserva Jaru southern (RJA) forests. Gray-shaded area is dry season as defined using satellite-derived measures of precipitation (TRMM: 1998-2018). Right hand plots correspond to Taylor diagrams for a statistical summary of model (color coded) fluxes compared to observations of seasonal fluxes (16-day). Missing sites indicate that the model overestimates the seasonality of observations; the ratio between model (σ_m) to observation standard deviations (σ) is >2. Simulations from ED2 (blue), IBIS (red), CLM3.5 (green), and JULES (purple).

Figure 7. Annual cycle 16-day average observations (black line) and modeled (color lines) of (a) ratio between the observed and reference evapotranspiration (ET/ET_{ref}), (b) canopy stomatal conductance (G_s; mmol m^{-2} s^{-1}) and (c) daytime water use efficiency where ET and GEP were sampled during dry conditions (no rain in prior 12 hours) assuming transpiration drives water fluxes ($WUE = GEP_{dry\&dry}/ET_{dry\&dry}$; gC mm^{-1}). From left to right study sites (from wettest to

driest) near Manaus (K34), Caxiuanã (CAX), Santarém (K67), and Reserva Jaru southern (RJA) forests. Gray-shaded area is dry season as defined using satellite-derived measures of precipitation (TRMM: 1998-2018). Right hand plots correspond to Taylor diagrams for a statistical summary of model (color coded) fluxes compared to observations of seasonal fluxes (16-day). Missing sites indicate that the model overestimates the seasonality of observations; the ratio between model (σ_m) to observation standard deviations (σ) is >2. Simulations from ED2 (blue), IBIS (red), CLM3.5 (green), and JULES (purple).

Figure 8. Relationships between seasonal 16-day average values of (a) canopy stomatal conductance (G_s; mm s^{-1}) and the ratio between sensible (H; W m^{-2}) and latent heat flux (LE; W m^{-2}) the unitless Bowen ratio ($Bowen$=H/LE), (b) G_s and daytime net radiation (Rn_{day}; W m^{-2}); (c) daytime LE (LE_{day}; W m^{-2}) and Rn_{day}, and (d) daytime H (H_{day}; W m^{-2}) and Rn_{day}. Panels may include a linear regression for all available data (black line) and single regressions fitted for each site and seasons (color lines): Manaus (K34), Caxiuanã (CAX), Santarém (K67), and Reserva Jaru southern (RJA) forests if statistically significant. Seasons classified using satellite precipitation TRMM values (1996-2018), dry (rainfall <100 mm month^{-1}) and wet-period (> 100 mm month^{-1}).

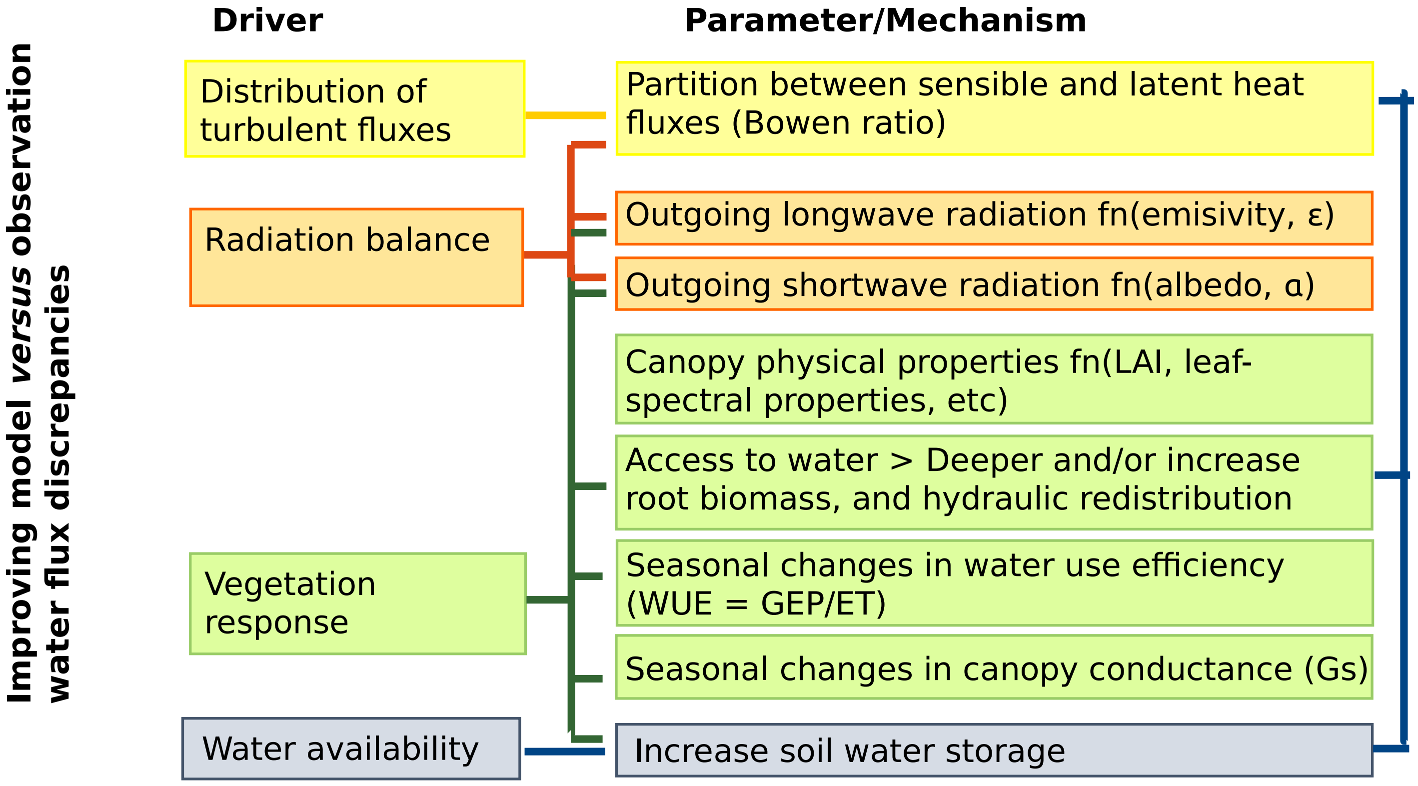

Figure 1. Parameters and mechanisms that govern ecosystem water fluxes (evapotranspiration) and their seasonality included in this study. Here classified as: water availability, vegetation response, radiation balance, and distribution of turbulent fluxes. Colored lines show which drivers interact with which parameters/mechanisms.

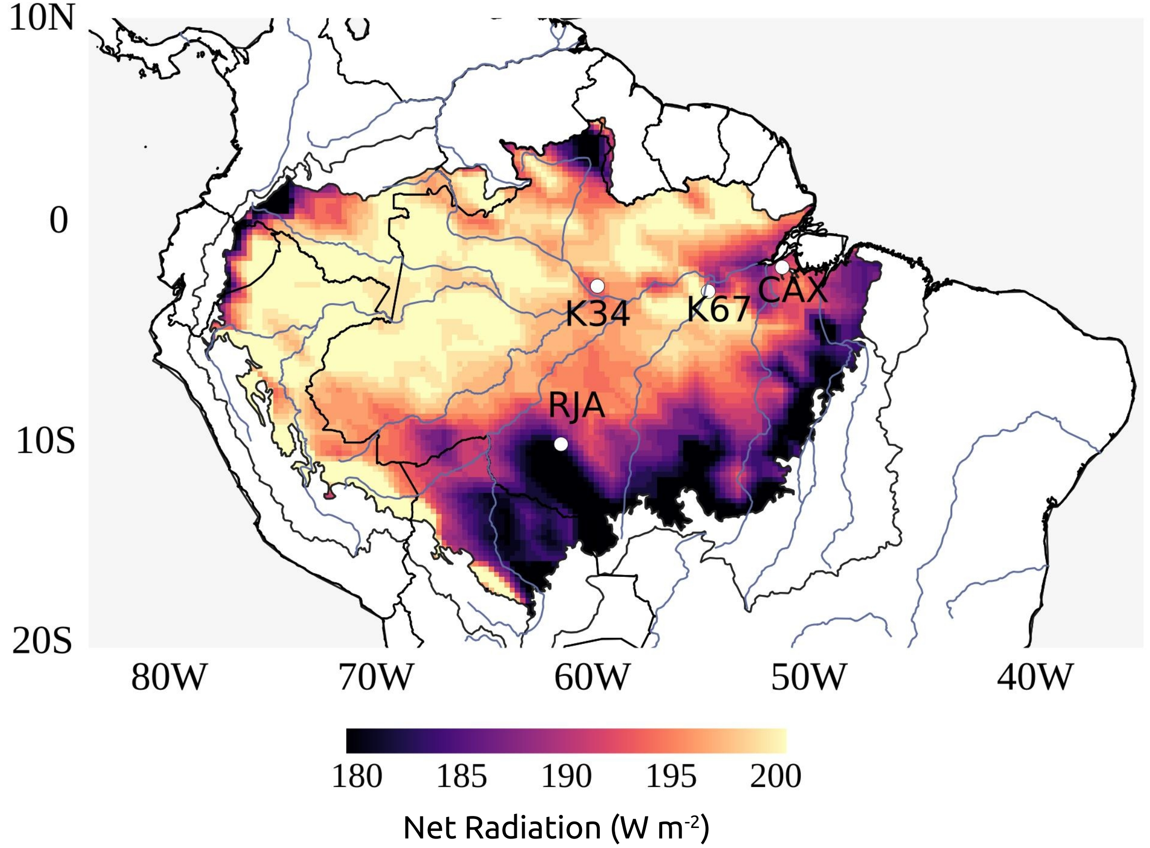

Figure 2: Locations of eddy covariance tower study sites in the Amazon Basin *sensu-stricto* (Eva and Huber (eds), 2005). Mean monthly net radiation (W m^{-2}) from the Clouds and the Earth's Radiant Energy System v4.0 (CERES) (Kato et al., 2012) for the years 2003 to 2018 (NASA, 2019).

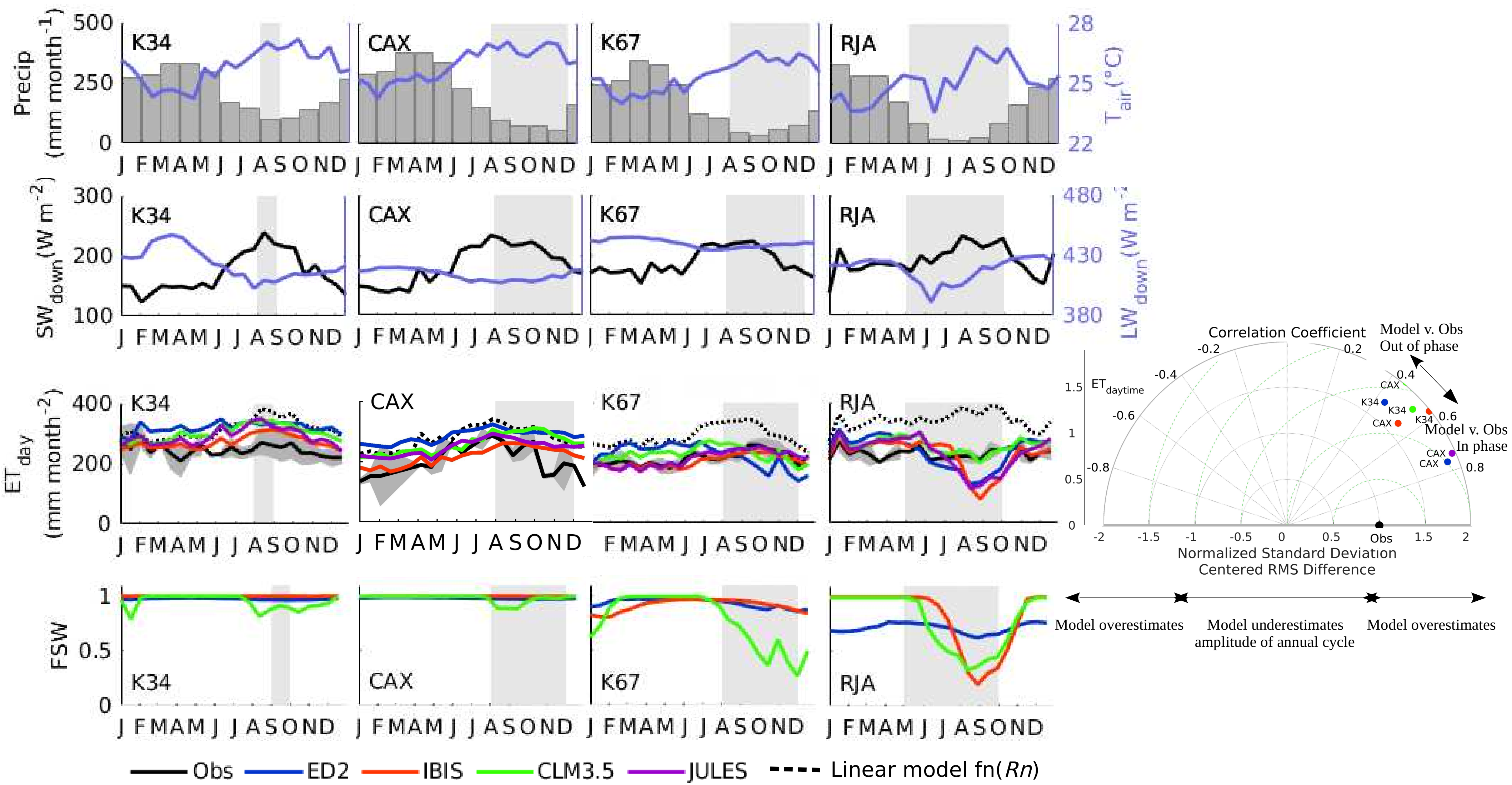

Figure 3: Annual cycle 16-day average (a) observed climatic drivers precipitation (*Precip*; mm month^{-1}) (gray bars), air temperature (T_{air}; ºC) (blue line left y-axis), (b) observed incoming shortwave (Sw_{down}; W m^{-2}) (black line right y-axis) and longwave radiation (LW_{down}; W m^{-2}) (blue line left y-axis), (c) modeled and observed and daytime evapotranspiration (ET_{day}; mm month^{-1}), dashed line corresponds to the reference evapotranspiration (model *ET* driven only by meteorology) and (d) model ecosystem-scale soil moisture 'stress' (FSW, where 1 = no stress). From left to right study sites (from wettest to driest) near Manaus (K34), Caxiuanã (CAX), Santarém (K67), and Reserva Jaru southern (RJA) forests. Gray-shaded area is dry season as defined using satellite-derived measures of precipitation (TRMM: 1998–2018). (e) Right hand plots correspond to Taylor diagram for a statistical summary of model (color coded) fluxes compared to observations of seasonal fluxes (16-day). Missing sites indicate that the model overestimates the seasonality of observations -model standard deviation (σ) normalized by observation σ is >2. Simulations from ED2 (blue), IBIS (red), CLM3.5 (green), and JULES (purple).

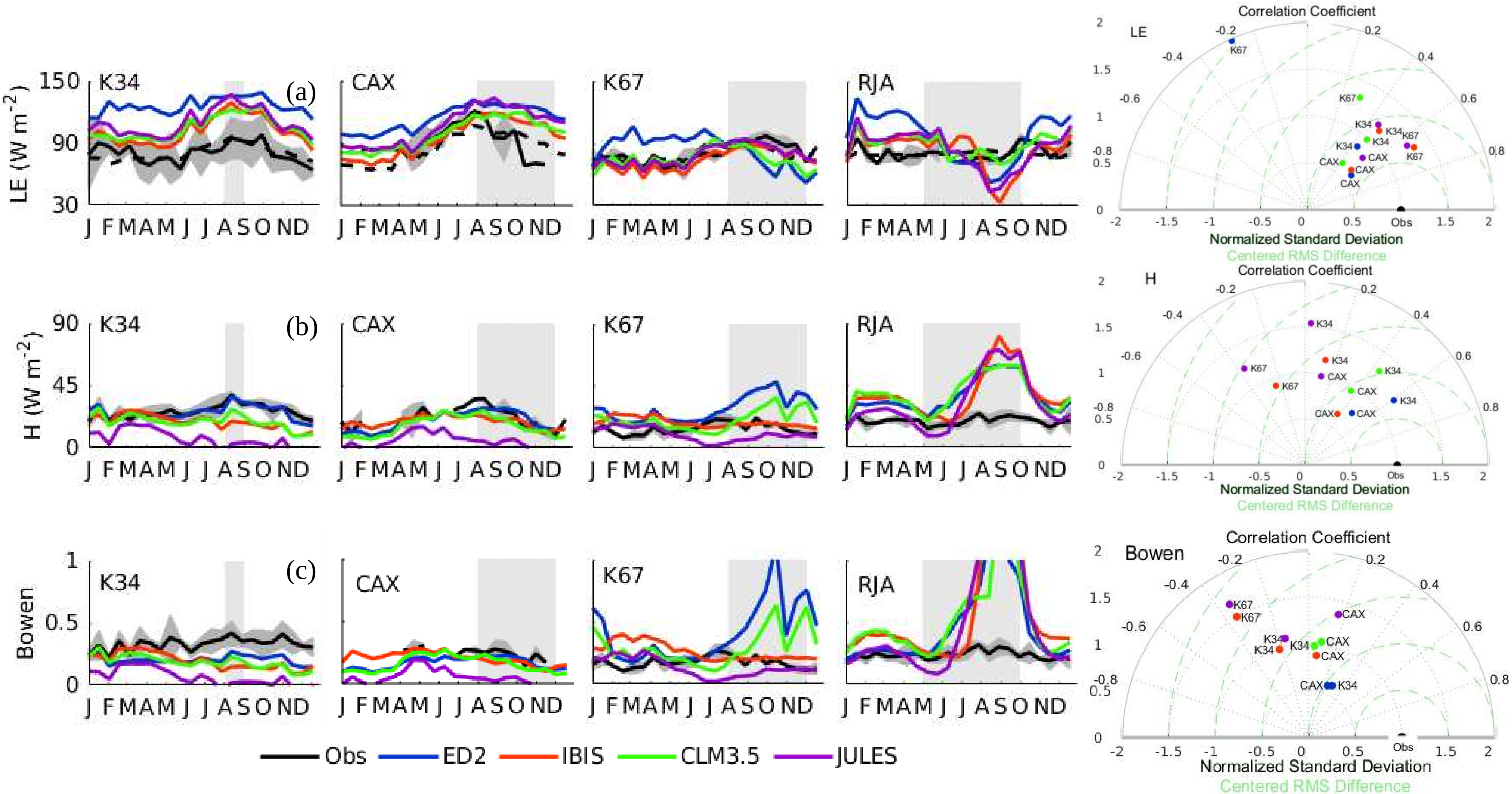

Figure 4: Annual cycle 16-day average (a) latent heat flux (*LE;* W m^{-2}) energy equivalent of evapotranspiration (*ET;* mm d^{-1}), (b) sensible heat flux (*H;* W m^{-2}) and (c) unitless Bowen ratio (*Bowen=H/LE*). From left to right study sites (from wettest to driest) near Manaus (K34), Caxiuanã (CAX), Santarém (K67), and Reserva Jaru southern (RJA) forests. Gray-shaded area is dry season as defined using satellite-derived measures of precipitation (TRMM: 1998–2018). Right hand plots correspond to Taylor diagrams for a statistical summary of model (color coded) fluxes compared to observations of seasonal fluxes (16-day). Missing sites indicate that the model overestimates the seasonality of observations -model standard deviation (σ) normalized by observation σ is >2. Simulations from ED2 (blue), IBIS (red), CLM3.5 (green), and JULES (purple).

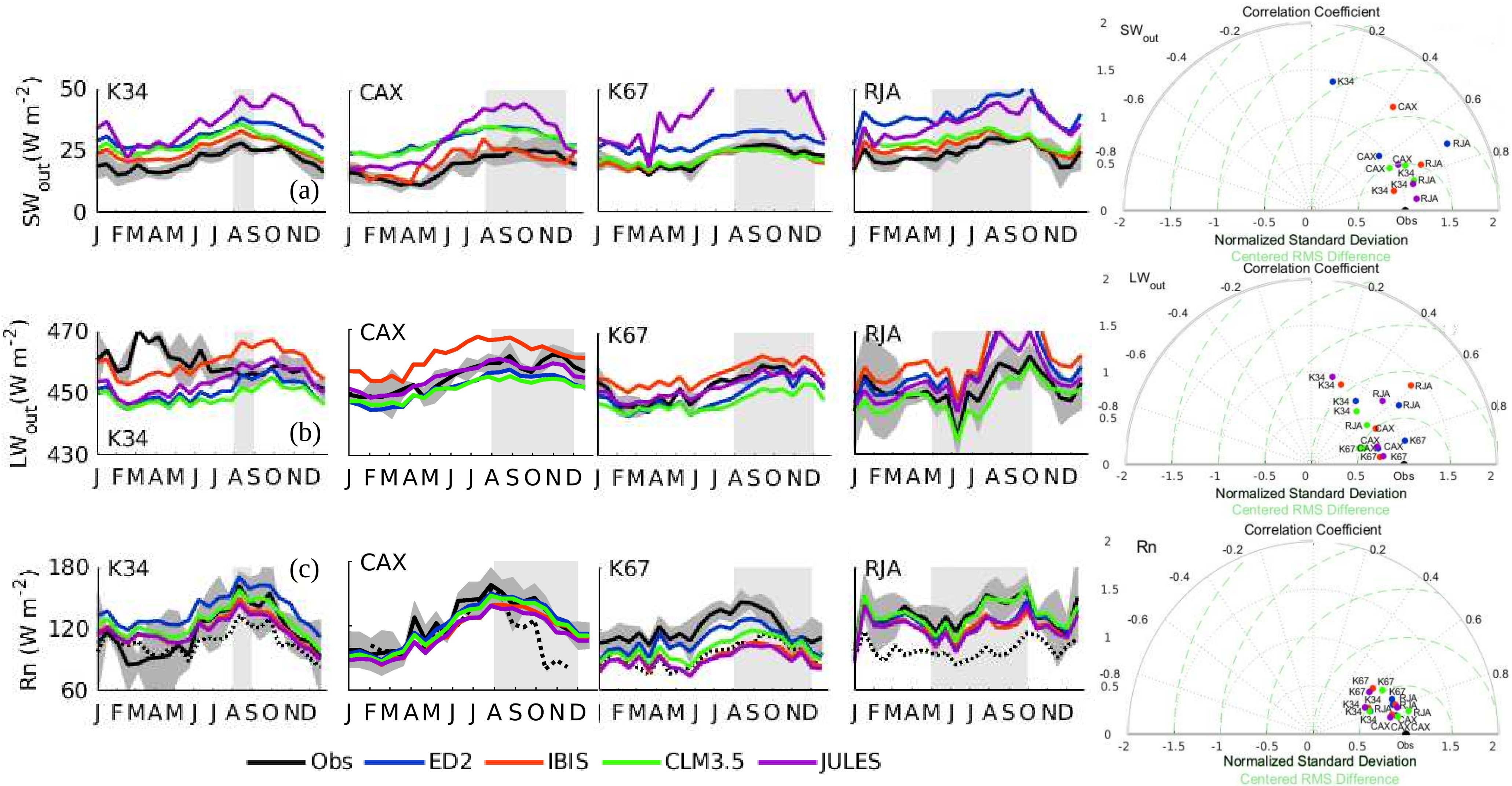

Figure 5: Annual cycle 16-day average (a) outgoing shortwave radiation (SW_{out}; W m^{-2}), (b) outgoing longwave radiation (LW_{out}; W m^{-2}) and (c) net radiation (*Rn;* W m^{-2}) (black continuous line) and the sum of turbulent fluxes, sensible plus latent heat flux (*H+LE*) (black dotted line). From left to right study sites (from wettest to driest) near Manaus (K34), Caxiuanã (CAX), Santarém (K67), and Reserva Jaru southern (RJA) forests. Gray-shaded area is dry season as defined using satellite-derived measures of precipitation (TRMM: 1998–2018). Right hand plots correspond to Taylor diagrams for a statistical summary of model (color coded) fluxes compared to observations of seasonal fluxes (16-day). Missing sites indicate that the model overestimates the seasonality of observations -model standard deviation (σ) normalized by observation σ is >2. Simulations from ED2 (blue), IBIS (red), CLM3.5 (green), and JULES (purple).

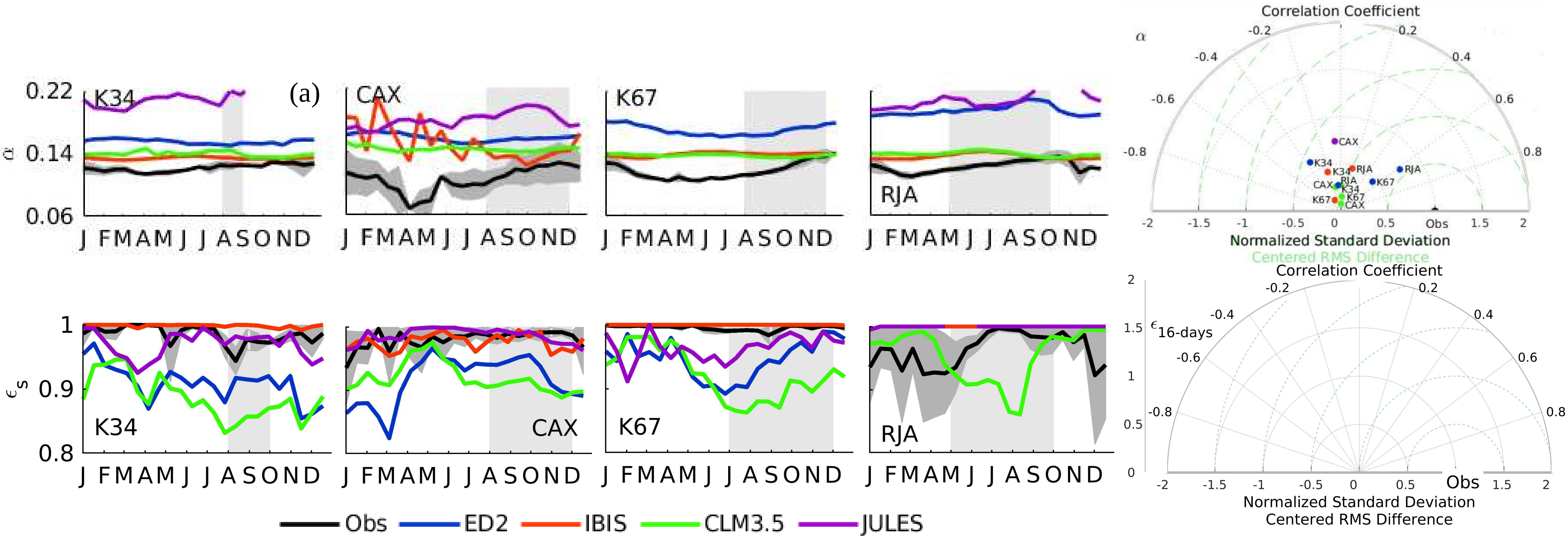

Figure 6: Annual cycle 16-day average (a) albedo defined as the ratio of outgoing to incoming shortwave radiation ($\alpha = SW_{out}/Sw_{down}$) (continuous line) and (b) emissivity (ε). From left to right study sites (from wettest to driest) near Manaus (K34), Caxiuanã (CAX), Santarém (K67), and Reserva Jaru southern (RJA) forests. Gray-shaded area is dry season as defined using satellite-derived measures of precipitation (TRMM: 1998–2018). Right hand plots correspond to Taylor diagrams for a statistical summary of model (color coded) fluxes compared to observations of seasonal fluxes (16-day). Missing sites indicate that the model overestimates the seasonality of observations -model standard deviation (σ) normalized by observation σ is >2. Simulations from ED2 (blue), IBIS (red), CLM3.5 (green), and JULES (purple).

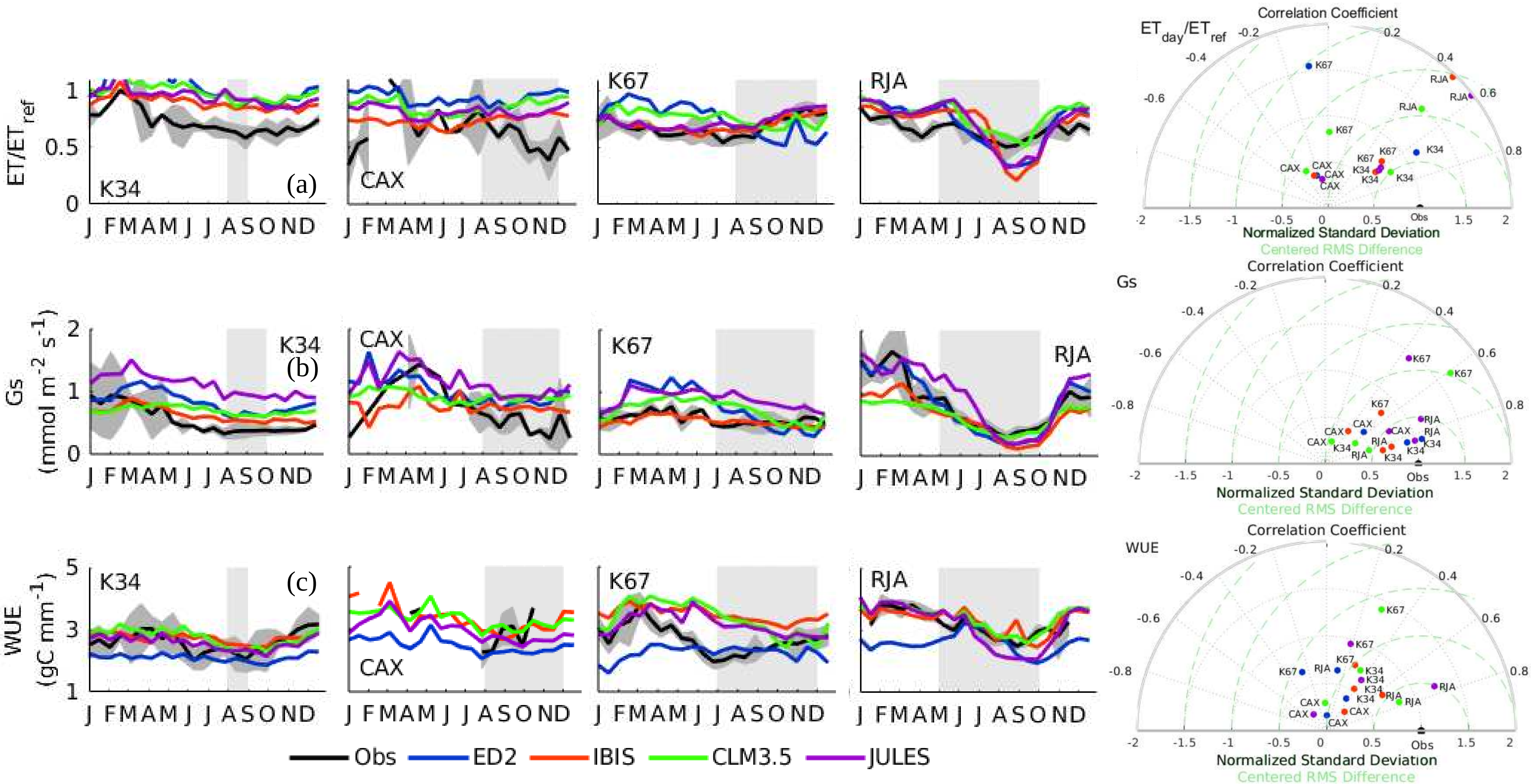

Figure 7: Annual cycle 16-day average (a) ratio between the observed and reference evapotranspiration (ET/ET_{ref}; %); (b) canopy conductance (G_s; mm s^{-1}) and (c) daytime water use efficiency where *ET* was sampled during dry conditions as to sample periods when transpiration (*T*) drives water fluxes ($WUE=GEP_{day\&dry}/ET_{day\&dry}$; gC mm^{-1}). From left to right study sites (from wettest to driest) near Manaus (K34), Caxiuanã (CAX), Santarém (K67), and Reserva Jaru southern (RJA) forests. Gray-shaded area is dry season as defined using satellite-derived measures of precipitation (TRMM: 1998–2018). Right hand plots correspond to Taylor diagrams for a statistical summary of model (color coded) fluxes compared to observations of seasonal fluxes (16-day). Missing sites indicate that the model overestimates the seasonality of observations -model standard deviation (σ) normalized by observation σ is >2. Simulations from ED2 (blue), IBIS (red), CLM3.5 (green), and JULES (purple).

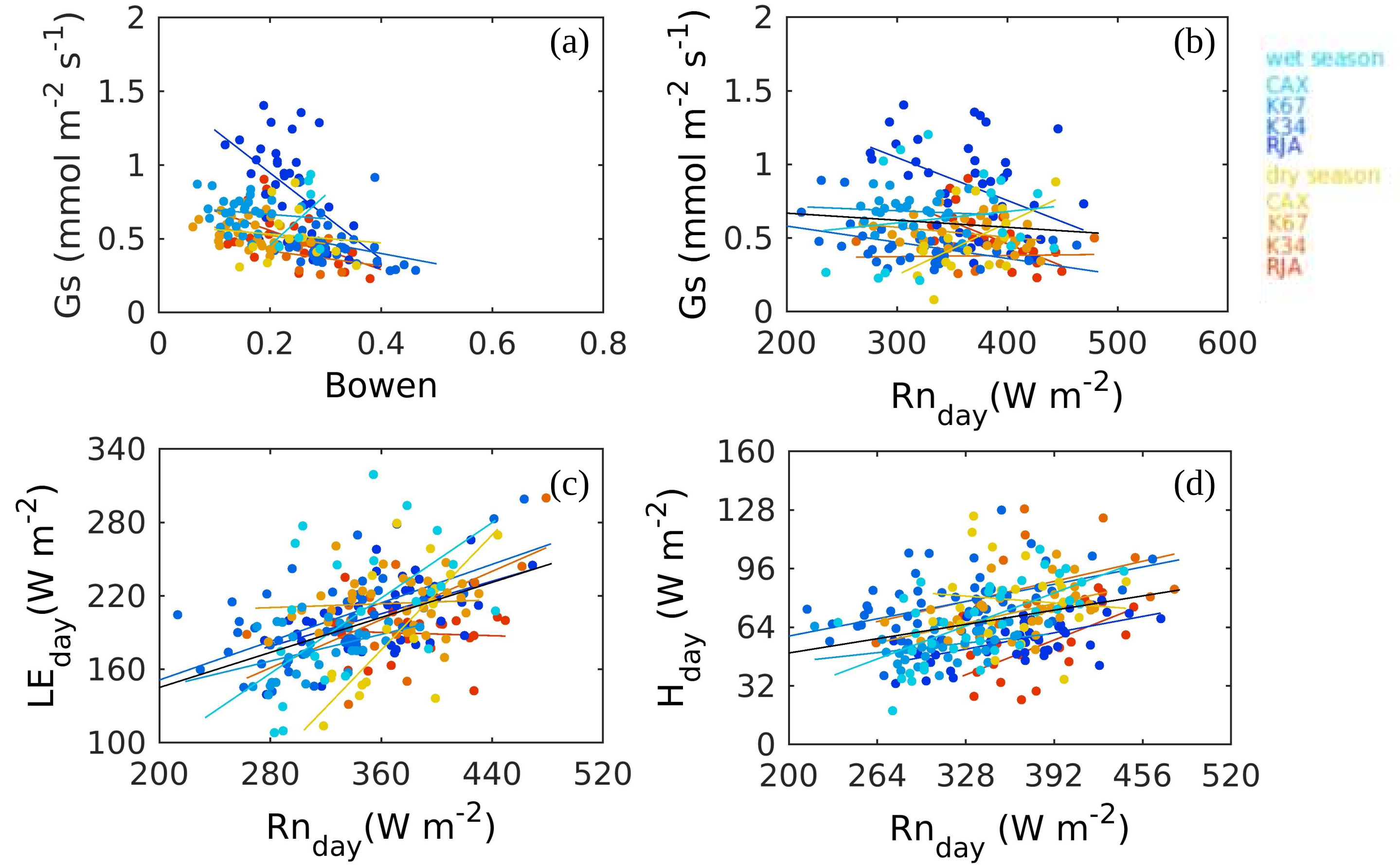

Figure 8: Relationships between seasonal 16-day average values of (a) canopy conductance (G_s; mmol m^{-2} s^{-1}) and the ratio between sensible (H; W m^{-2}) and latent heat flux (LE; W m^{-2}) the unitless Bowen ratio (*Bowen=H/LE*), (b) G_s and daytime net radiation (Rn_{day}; W m^{-2}), (c) daytime LE (LE_{day}; W m^{-2}) and Rn_{day} and (d) daytime H (H_{day}; W m^{-2}) and Rn_{day}. Panels may include a linear regression for all available data (black line) and single regressions fitted for each site and seasons (color lines): Manaus (K34), Caxiuanã (CAX), Santarém (K67), and Reserva Jaru southern (RJA) forests. Seasons classified using satellite precipitation TRMM values (dry ≤ 100 mm month^{-1} and wet-period > 100 mm month^{-1}).

Supporting Information

Understanding water and energy fluxes in the Amazonia:
Lessons from an observation-model intercomparison

Natalia Restrepo-Coupe, Loren P. Albert, Ian Baker, Marcos Longo, Naomi M. Levine, Lina M. Mercado, Alessandro C. da Araujo, Bradley O'Donnell Christoffersen, Marcos H. Costa, David R. Fitzjarrald, David Galbraith, Hewlley Imbuzeiro, Yadvinder Malhi, Celso von Randow, Xubin Zeng, Paul Moorcroft, Scott R. Saleska

Here we present ancillary figures, uncertainty analysis of energy balance closure and other supplementary information.

1. Uncertainty analysis energy balance (EB) closure

The purpose of our analysis was to calculate all components of the energy balance. We measured net radiation (*Rn*; W m^{-2}), latent (*LE*; W m^{-2}) and sensible heat flux (*H*; W m^{-2}), as well as the energy change due to photosynthetic activity (*ΔSc*; W m^{-2}) and the energy balance residual (*Δ*) at all sites. We were able to calculate heat storage change in canopy air (*ΔSh*; W m^{-2}) and biomass (*ΔSb*; W m^{-2}) at three of the four forests (K67, CAX, and RJA).

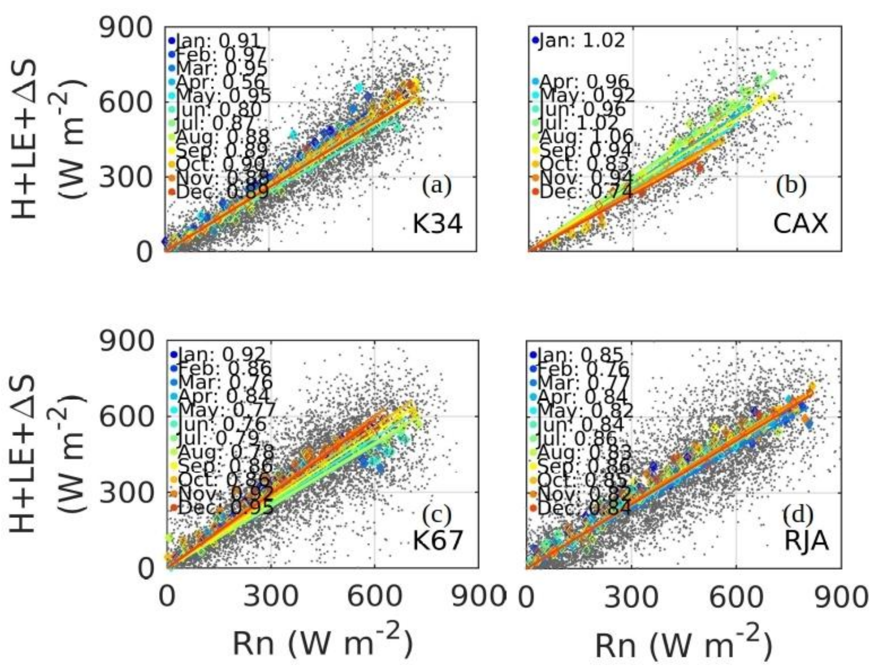

Figure S1. Monthly linear regressions between net radiation (*Rn*; W m^{-2}) and the sum of hourly sensible (*H*; W m^{-2}), latent heat flux (*LE*; W m^{-2}) and change in energy storage; (*ΔS*; W m^{-2}). Where *ΔS* includes the energy change due to photosynthetic activity (*ΔSc*), and when available, change in biomass (*ΔSb*; W m^{-2}) and surface heat storage (*ΔSh*; W m^{-2}). Data grouped per month in 30 bins, each average calculated for a minimum of 10 values and shown in color lines. All hourly measurements as gray dots. Sites from left to right and top to lower panels: Manaus (K34), Caxiuanã (CAX), Santarém (K67) and Jaru (RJA).

The *ΔSc* was defined as the product of *GEP* and the specific energy of conversion due to photosynthesis (1.088×10^4 J gCO_2^{-1}) (Moderow et al., 2009). We calculated *ΔSb* as the product of canopy-specific heat capacity (C_{veg} = 2958 J kg^{-1} K^{-1}), live wet biomass (m_{veg}; kg m^{-2}) and the change in temperature at canopy level ($\Delta T_{cpy}/\Delta t$; K s^{-1}). Where the temperature at canopy level (T_{cpy} ; °C) was measured at 32 m at CAX, 35 m at RJA and 39 m height at K67 (Table S1). At K67 m_{veg} was estimated to be 63 kg m^{-2} (the equivalent of 32.5 kg m^{-2} dry biomass) (M. O. Hunter et al., 2013) and at RJA we used the same value as an acceptable approximation. The m_{veg} was 94.2 kg m^{-2} at CAX (Metcalfe et al., 2007) and 81.2 kg m^{-2} at K34 (Malhi et al., 2009) (Table S1).

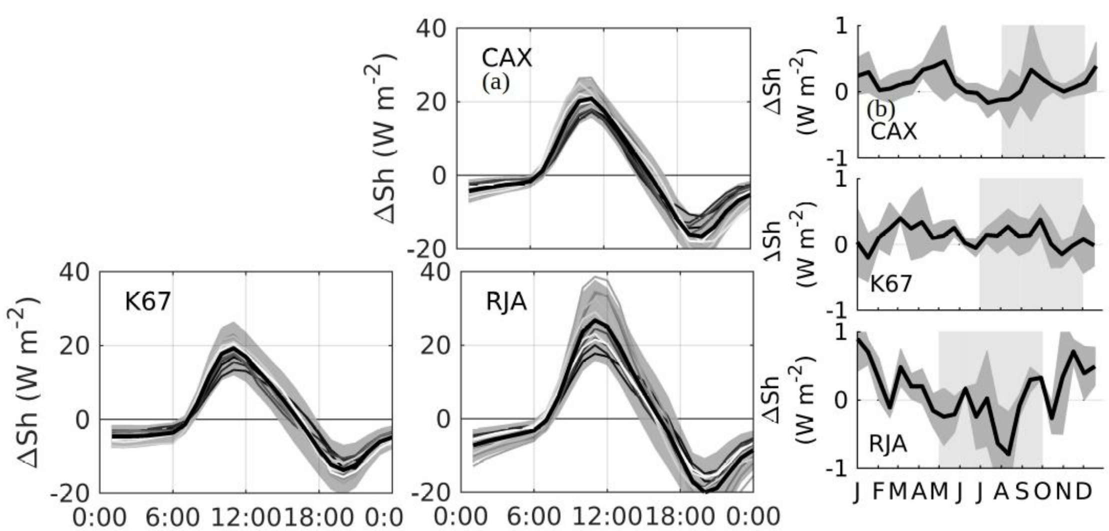

s

Figure S2: (a) Annual mean daily hourly cycle (black thick line) of change in surface heat storage (ΔSh; W m^{-2}). (Monthly average values as gray lines.) (b) Annual monthly cycle of ΔSh. From top to bottom and left to right and top to lower panels study sites (from wettest to driest) Caxiuana (CAX), Santarém (K67), and Reserva Jaru southern (RJA) forests.

No site had available information of bole, branch and leaf temperatures; therefore, our *ΔSb* estimates are an approximation and may underestimating the true value, thus as tropical forest moisture and biomass other than tree biomass (e.g. lianas and understory vegetation) can be significantly high (Figure S2). Moderow et al. (2009) noted that although the daily maximum will be shifted towards the morning hours, the magnitude of the estimated *ΔSb* will be comparable to "true" values (derived from biomass measurements). Similar to Moderow et al. (2009), we found nighttime *ΔSb* and *ΔSh* values were significant compared to *Rn*. At the sites where temperature measurements were available (CAX, RJA and K67) including *ΔSb* and *ΔSh* on the energy balance calculations clearly reduced the magnitude of the imbalance.

The lack of energy balance closure has been mainly attributed to low frequency loss of flux and the failure of a single point measurement to account for the spatial dispersive flux (Barr et al., 1994). Other sources of uncertainty relate to the differences in footprint between the eddy covariance (EC) and radiation sensors (Wilson et al., 2002). Thus as the footprints of all sensors change continuously. For example, leaf angular distribution, leaf clumping and *LAI*, in addition to the sensor height and field of view (FOV) drive the LW_{out} and SW_{out} radiation footprint (Marcolla & Cescatti, 2018; Markkanen et al., 2003). At tall forests, the daily changes in forest structure determine the area of influence of (1) canopy flux and (2) soil radiation -- where the contribution of (2) to the radiometer's footprint is typically larger than (1). By contrast, the shape of the area represented by the EC flux measurements will be driven by the forest structure, wind direction, and turbulence patterns, among other parameters and variables, resulting in larger nighttime and smaller daytime footprints. In general at our sites, the footprint of *LW* and *SW* (~1-2 km radius) would be larger than the EC footprint (~100 - 300 m radius, skewed by the dominant wind direction). However, the forests sites here presented, although heterogeneous (e.g. structure and species diversity), are dense and no other land use or gap fractions near-by may influence the sampled fluxes. We acknowledge this and other sources of error; however, rather than compare footprints, determine signal losses or other technical analysis, we attempt to quantify the uncertainty and probable causes of the energy balance residual.

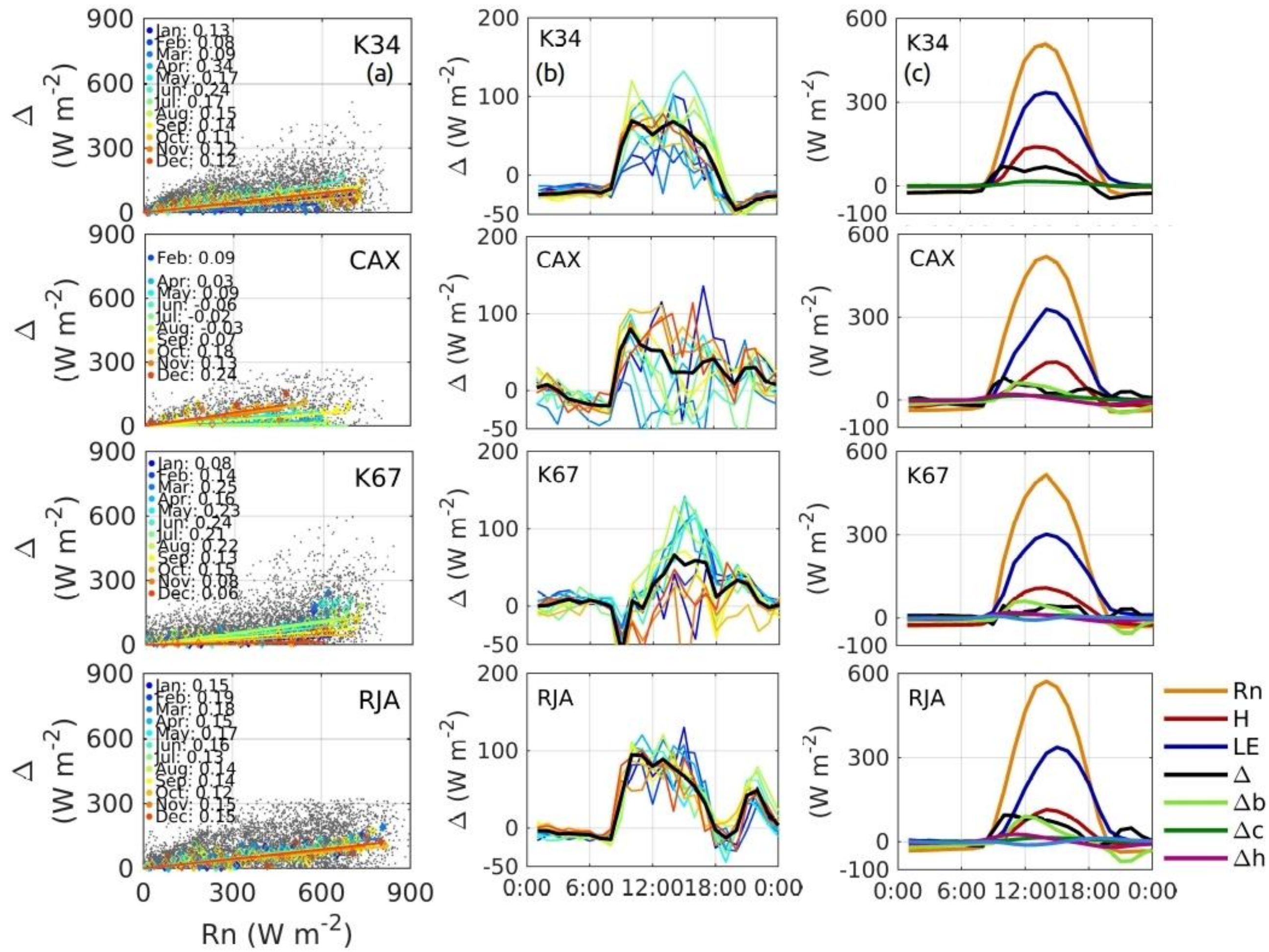

Figure S3. Left column, (a) monthly linear regressions between net radiation (*Rn*; W m^{-2}) and the energy balance imbalance (*Δ*; W m^{-2})*,* monthly regressions from 30 equally spaced bins their range defined by minimum and maximum *Δ* values. (b) Monthly average daily hourly cycle of *Δ* (color lines correspond to different months, black line is the average for all available data). Right column, (c) monthly average daily hourly cycle of *Rn*; W m^{-2})*,* sensible (*H*; W m^{-2}), latent heat flux (*LE*; W m^{-2}), the energy change due to photosynthetic activity (*ΔSc*; W m^{-2}), *Δ,* and when available, change in surface heat storage (*ΔSh*; W m^{-2}) and biomass heat storage (*ΔSb*; W m^{-2}).

We observed no statistically differences in the slope of the energy balance when aggregated by month (Figure S1). However, at CAX seasonal differences in incoming radiation values (e.g. sustained low, January to March, and high, June to October, *Rn* values) did translate in the segregation of the regression values (e.g. 0-400 W m^{-2} Jan-Mar and 200-600 W m^{-2} Jun-Oct). In general, the *Δ* values were small compared to *Rn* (Figure S3a). The daily cycle of the residual followed the available energy, indicating that other unaccounted or underestimate storage terms (e.g. ground heat flux) could contribute to the missing flux (Figure S3b). Moreover, the uncertainty in *Rn* has been quantified to be ±7% or ±20 W m^{-2} (Moderow et al., 2009), at times, close to the *Δ* value.

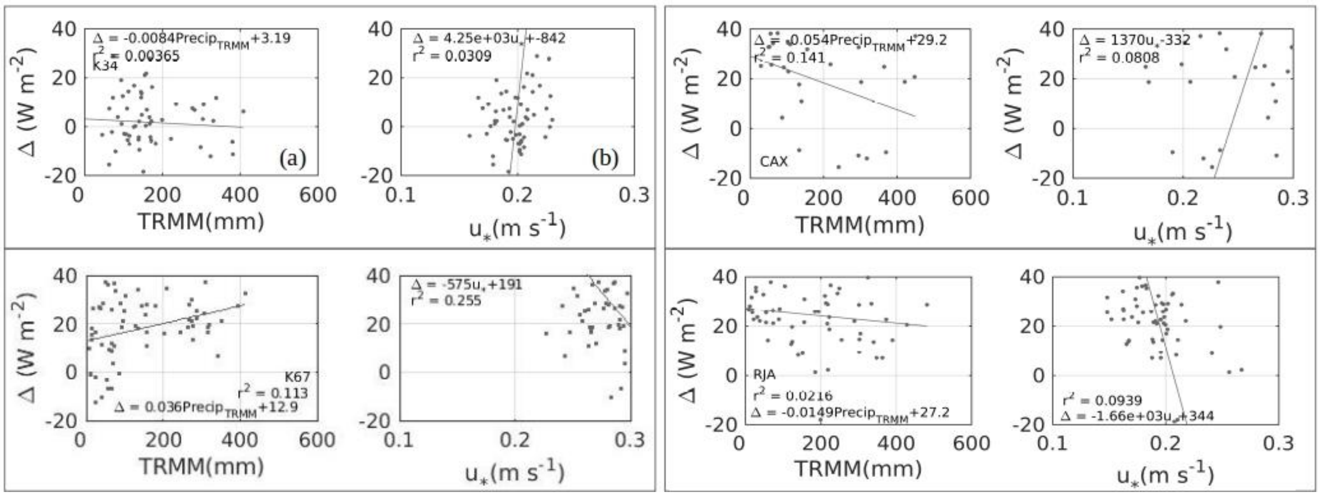

Figure S4. Type II linear regressions between 16-day time series: (a) energy balance closure imbalance (*Δ*; mm $month^{-1}$) and satellite-derived precipitation ($Precip_{TRMM}$; mm $month^{-1}$), (b) *Δ* and friction velocity (u_*; m s^{-1}). Sites from left to right and top to lower panels: Manaus (K34), Caxiuanã (CAX), Santarém (K67) and Jaru (RJA) forests.

To determine possible drivers of the seasonal imbalance we compared *Δ* and precipitation and turbulence and found no statistical significant relation (Figure S4). To evaluate the uncertainty added by *Δ* to our seasonal *LE* and *H* analysis, we compared uncorrected and "corrected" fluxes: where the energy balance closure was forced to hourly values by (1) adding the residual scaled by the seasonal Bowen ratio to *LE* and *H* (e.g. $LE_{corrected} = LE + \Delta$ Bowen, and $H_{corrected} = H + \Delta$ *(1-Bowen)*) (Twine et al., 2000), (2) equally partitioning *Δ* to each flux *(e.g.* $LE_{corrected} = LE + \Delta/2$ and $H_{corrected} = H + \Delta/2$), and (3) assigning all *Δ* to each flux -upper boundary of the confidence interval ($LE_{corrected} = LE + \Delta$, or $H_{corrected} = H + \Delta$) -- where it is believed that large-scale coherent structures not captured by the EC are driven by buoyancy and primarily translate in additional *H* (Charuchittipan et al., 2014). In general, seasonal *Δ* values were comparatively small to *LE* and did not change the amplitude or shape of the annual cycle (Figure S5). By contrast, assigning **all** the imbalance to *H* did change the seasonal mean at CAX and RJA, thus as at tropical forests the *H* is relatively small. However, we can assume that improving measurements of storage fluxes (*ΔSb* and *ΔSh*) and including unaccounted flux components (e.g. *G* and *ΔSle*) may further reduce the *Δ*. The here presented analysis constitutes an advance in determining many of the generally unaccounted storage terms at tropical sites. We are confident that our results and conclusions hold relative to the energy balance closure issues.

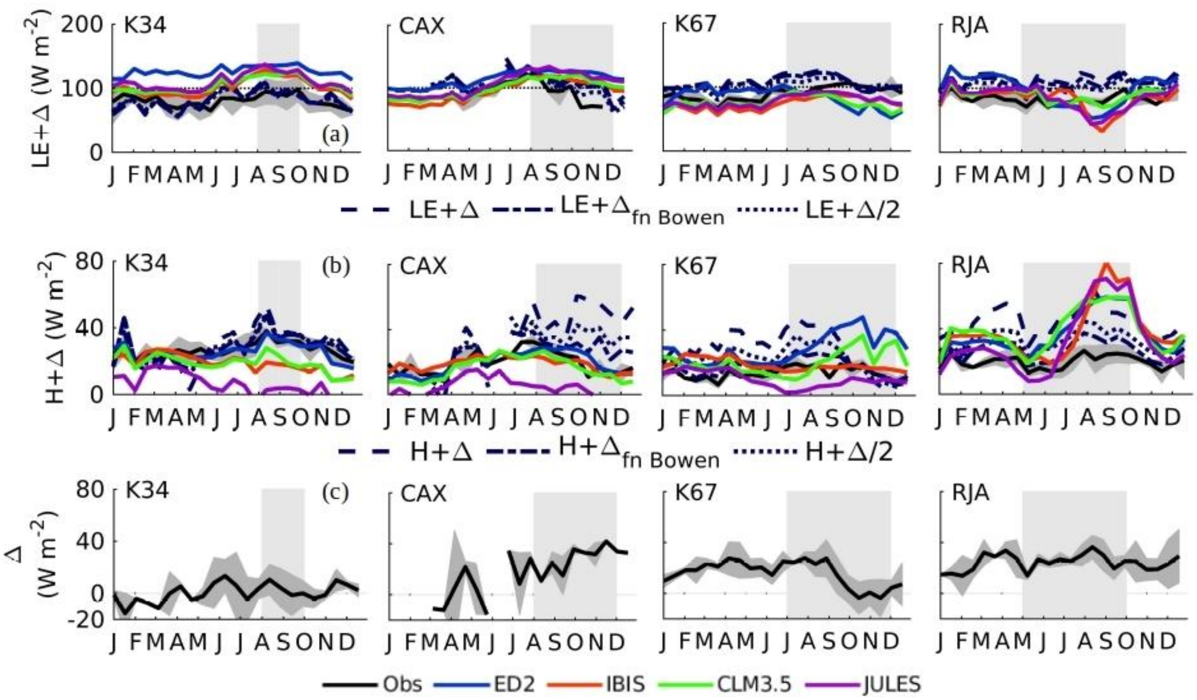

Figure S5. Annual cycle 16-day average (a) latent heat flux (*LE*; W m^{-2}) and the sum of *LE* and the energy balance closure imbalance (*Δ*; W m^{-2}) or half of *Δ* or *Δ* scaled by the Bowen ratio (*Δ* x (1-Bowen)), (b) sensible heat flux (*H*; W m-2), sum of *H* and *Δ* or half of *Δ* or *Δ* scaled by the Bowen ratio (*Δ* x Bowen), and (c) the residual, *Δ,* includes measurement error, ground heat flux, and latent heat storage flux. At K34, the *Δ* includes canopy sensible and biomass storage fluxes. From left to right study sites (from wettest to driest) near Manaus (K34), Caxiuanã (CAX), Santarém (K67), and Reserva Jaru southern (RJA) forests. There is no energy balance residual in model flux data. Light gray-shaded area is dry season as defined using satellite-derived measures of precipitation (TRMM: 1998–2018). Simulations from ED2 (blue), IBIS (red), CLM3.5 (green), and JULES (purple).

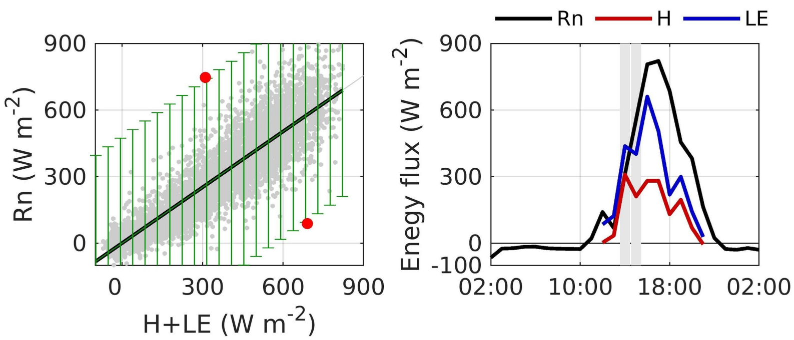

Figure S6. Using the energy balance closure to flag possible errors on the flux dataset. Left panel compares net radiation (*Rn*; W m^{-2}) to the sum of sensible (*H*; W m^{-2}) and latent heat flux (*LE*; W m^{-2}). Values outside two standard deviations from the fitted linear regression were queried as possible outliers (red dots). Left panel shows the daily cycle of *Rn*, *LE,* and *H*, corresponding to the lower red dot (gray bars point to the time to be checked).

……………………………………………………………………………………………………

2. Carbon flux uncertainty and methods

We used the term gross primary productivity (*GPP*) interchangeably with gross ecosystem productivity (*GEP*; gC m^{-2} d^{-1}) and negative gross ecosystem exchange (*GEE*; gC m^{-2} d^{-1}), where *GPP*~*GEP*=-*GEE* (Stoy et al., 2006). The *GEE* was estimated from the measured daytime net ecosystem exchange (*NEE*; gC m^{-2} d^{-1}) by subtracting estimates of ecosystem respiration (R_{eco}; gC m^{-2} d^{-1}), which in turn were derived from nighttime *NEE* ($GEE = -NEE + R_{eco}$). The *NEE* was calculated as the sum of the fluxes measured at the top of the tower and the CO_2 storage flux ($NEE = Fc + S_{CO2}$) and filtered for low turbulence periods (site-specific friction velocity (u_*; m s^{-1}) threshold ($u_{*thresh}$) selected by the boot-strap method). R_{eco} was calculated as the average within a centered 5-day wide moving window, assuming at least 8 valid hours of nighttime *NEE* (we expanded the window up to 30 days until sufficient valid data were included). The selected R_{eco} moving window accounts for sensitivity to seasonally varying soil moisture. No statistically significant relationship between nighttime *NEE* and T_{air} was observed. Daytime R_{eco} was assumed to be equal to nighttime R_{eco}. Uncertainties and errors in characterizing seasonal *GEP* and R_{eco} arise from at least three sources: (1) systematic measurement bias (e.g. photoinhibition, differences between day and night-time footprint and advection as a function of turbulence, re-assimilation of metabolic respiration CO_2 within the leaf, and CO_2 recirculation below the EC system, among others), (2) random sampling error, and (3) variations due to interannual variability in climate or other driver variables. These sources of errors have been explored in previous studies (Restrepo-Coupe et al., 2013, 2017) and continue to be an area of active research. We address some of this uncertainties by removing periods with unrepresentative low fluxes via a conservative $u_{*thresh}$ and by including the standard deviations to the seasonal annual cycles obtained by averaging multiple years of observations.

…………………………………………………………………………………………………

3. Supplementary figures Methods section

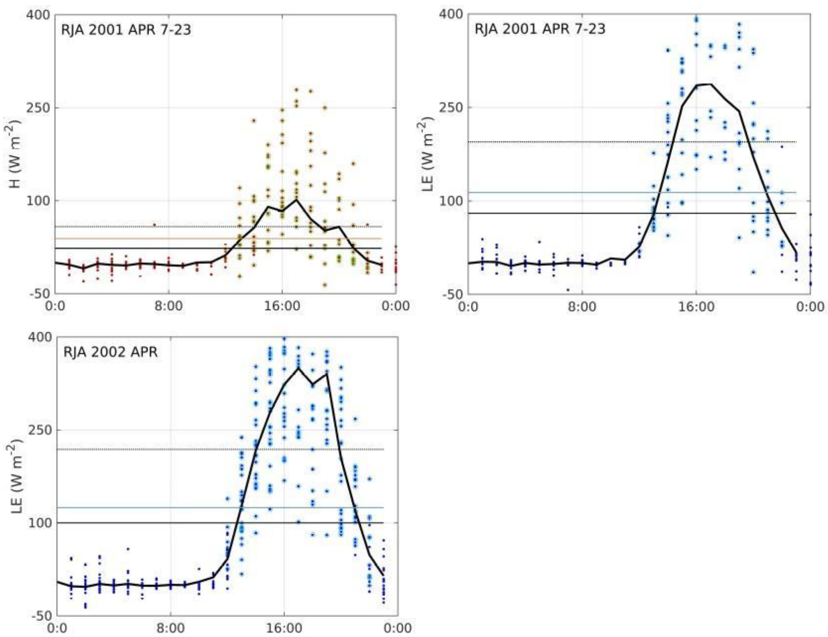

Figure S7: Calculating monthly (lower panel) and seasonal (16-day) values (top panels) based on an average daily cycle (dark continuous line). All observations as color dots and day-time values highlighted. Continuous horizontal lines in black illustrate the mean value for the season using the daily cycle method (dashed line day-time) and horizontal color line show the average of all measurements (a different method) for the period. Example for RJA latent (*LE*; W m^{-2}) and sensible heat flux (*H*; W m^{-2}). The x-axis in Coordinated Universal Time (UTM), where local time = UTC-4 hours.

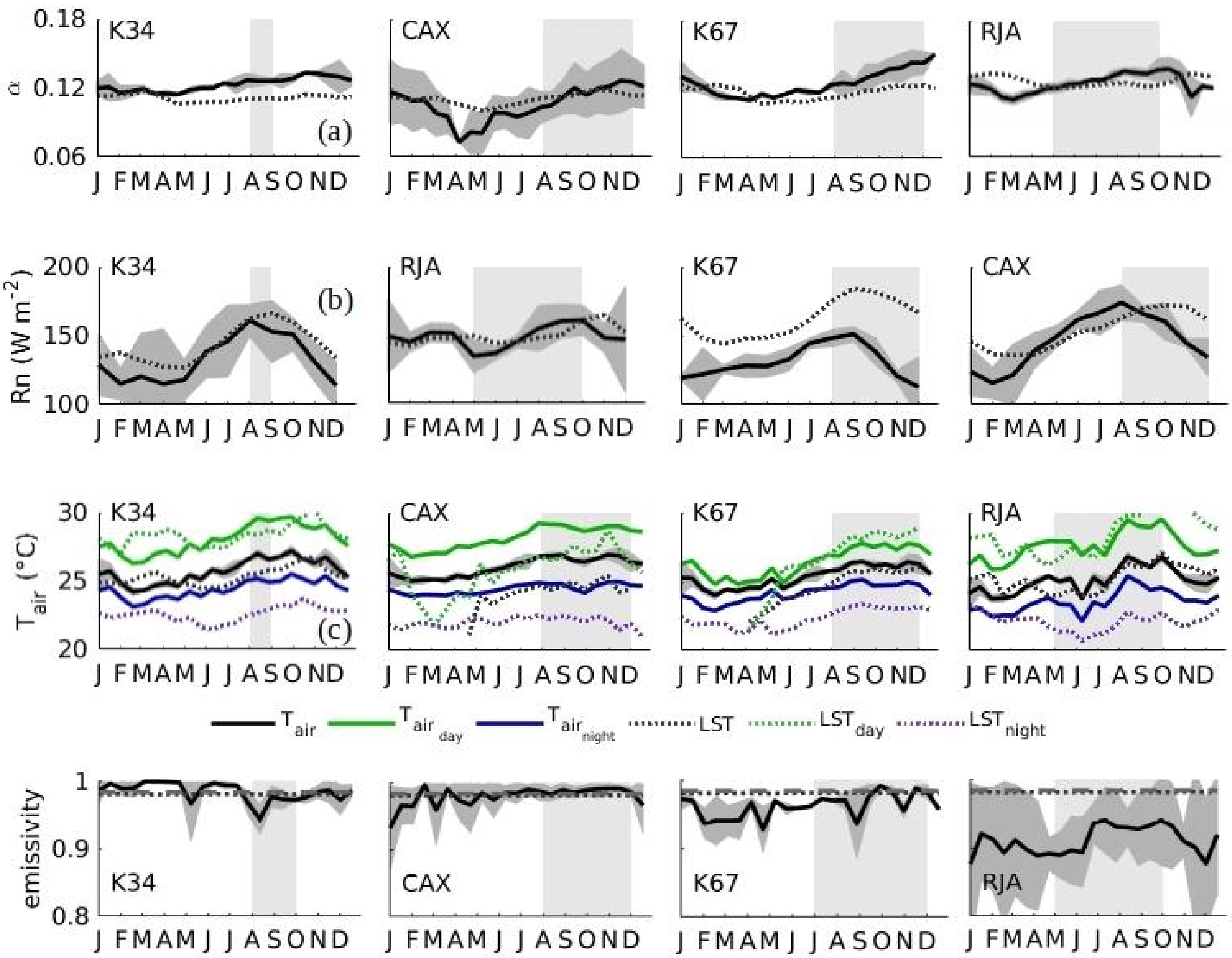

Figure S8. Annual monthly cycle of (a) albedo defined as the ratio of outgoing to incoming shortwave radiation ($\alpha = SW_{out}/SW_{down}$) (continuous line) and MCD43A3 black-sky (direct light) albedo (NASA, 2019) used to constrain some LSM (dashed line) and (b) site measurements of net radiation (*Rn*; W m^{-2}) (continuous line) and Clouds and the Earth's Radiant Energy System v4.0 (CERES) (NASA, 2019) net radiation (dashed line). (c) Observations of air temperature (T_{air}; C) (black continuous lines), day (green lines) and nighttime values (blue lines) compared to the 1 km grid 8-day product MOD11A2 land surface temperature nighttime (22:00 bypass, LST_{night}; °C), day time (10:00 bypass LST_{day}; °C) and the average between LST_{day} and LST_{night}, here labeled as *LST*. (d) Surface emissivity (continuous lines) calculated from observations and MOD11A2 band 32 emissivity (dashed lines). Averages calculated for the site-specific model run years. From left to right study sites (from wettest to driest) near Manaus (K34), Caxiuanã (CAX), Santarém (K67), and Reserva Jaru southern (RJA) forests.

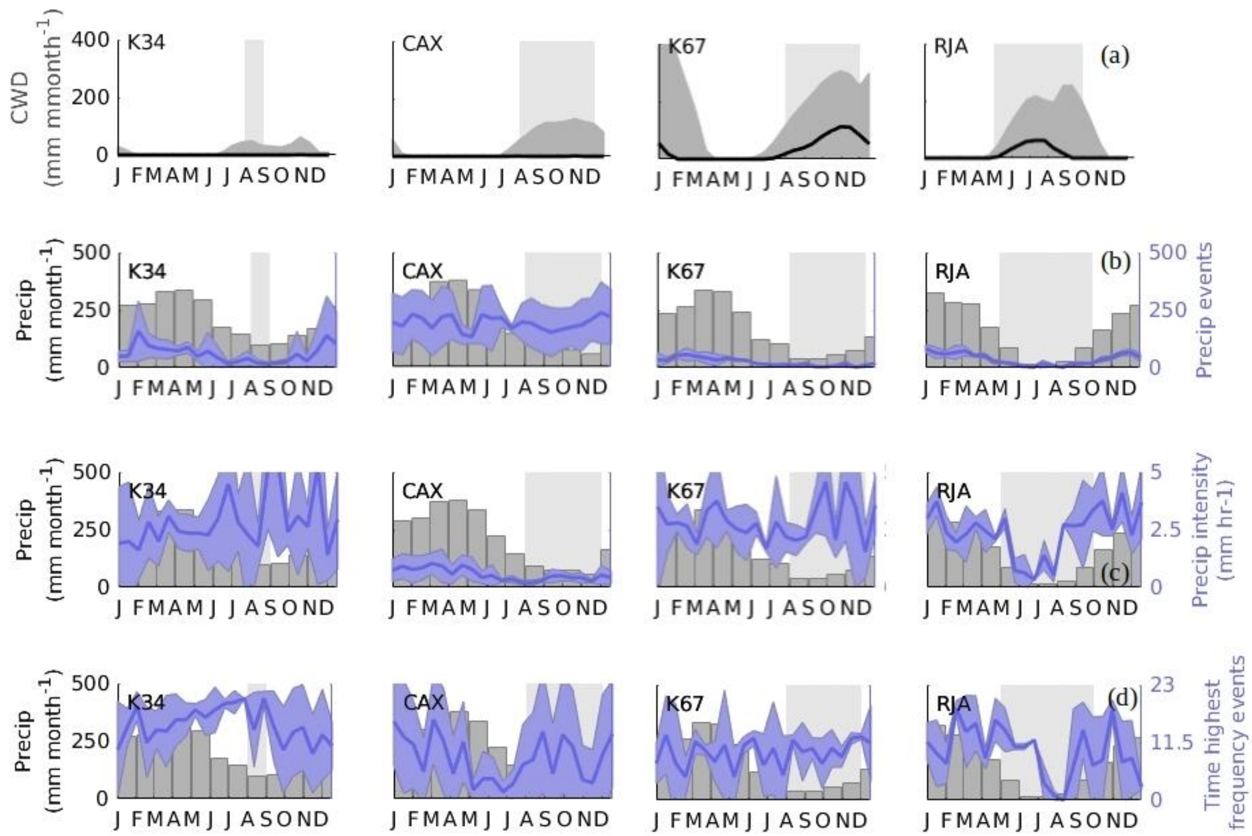

Figure S9. Annual monthly cycle of cumulative water deficit (*CWD*; mm month^{-1}) calculated following Aragão et al. (2007), (b) number of precipitation events; precipitation intensity (mm hour^{-1}), (c) precipitation intensity (mm hour^{-1}) and (d) time of highest frequency of precipitation events.

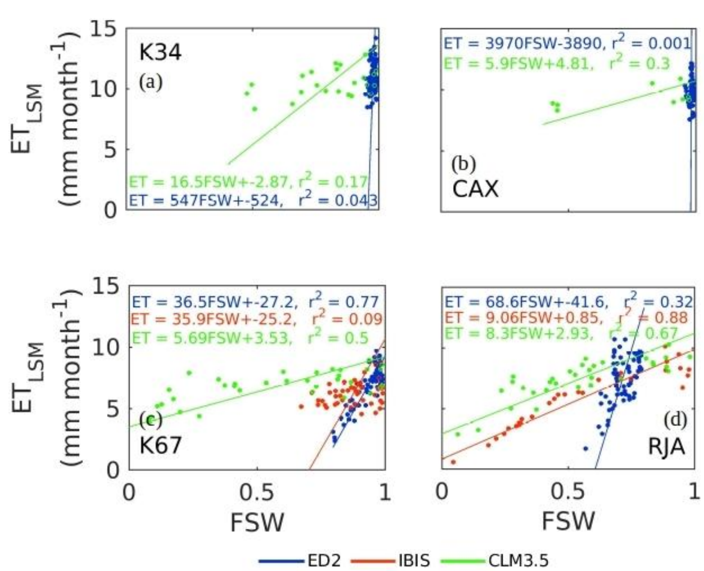

Figure S10. Type II linear regression between 16-day model estimates of evapotranspiration (ET_{LSM}, mm month^{-1}) and plant available water (FSW), where FSW = 1 is no water stress. Top panel (a) Manaus (K34), (b) Caxiuanã (CAX), and lower figures (c) Santarém (K67) and (d) Jaru (RJA) forests. Regression excludes FSW values above 0.99. Simulations from ED2 (blue), IBIS (red), and CLM3.5 (green). No FSW data available for JULES.

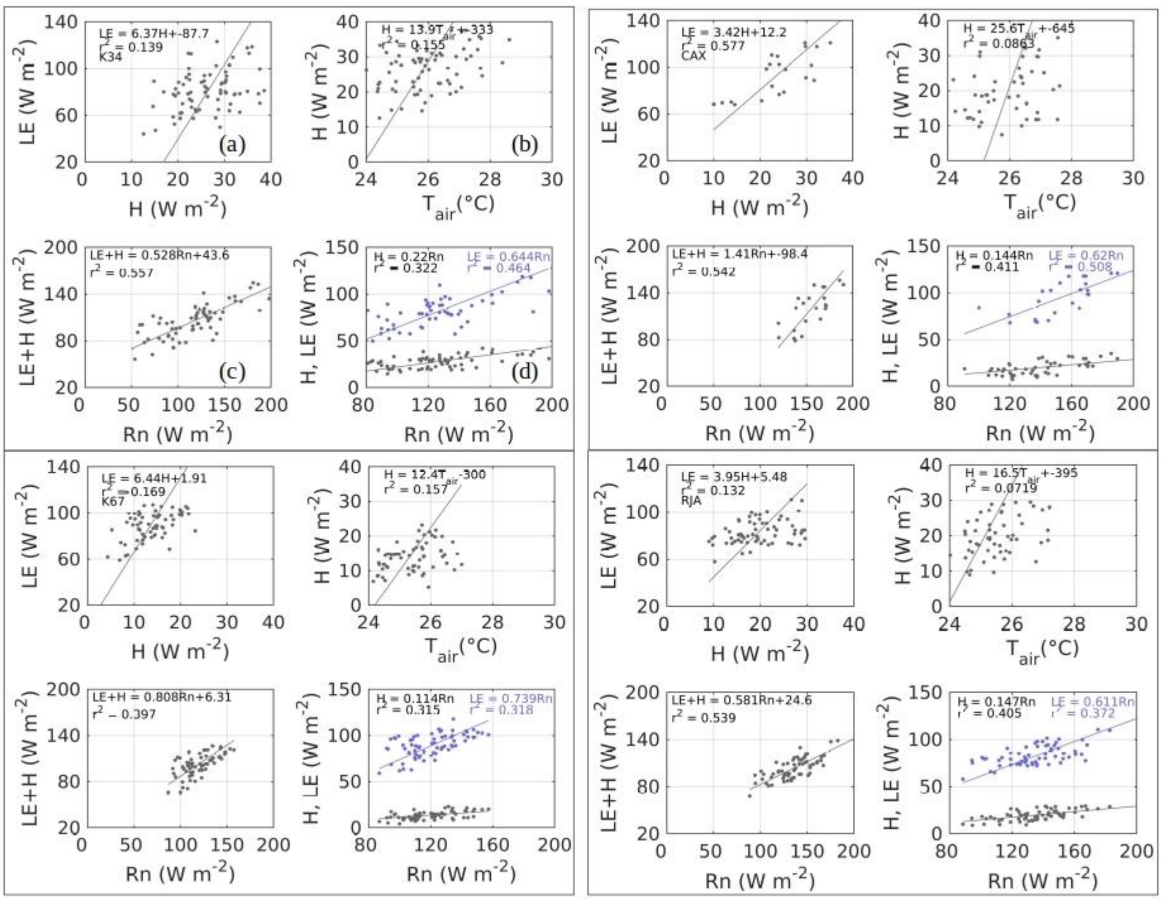

Figure S11. Type II linear regression between 16-day time series for each site: (a) sensible (H; W m^{-2}) and latent heat flux (LE; W m^{-2}); (b) H and air temperature (T_{air}; ºC), (c) H+LE and net radiation (Rn; W m^{-2}); and (d) turbulent fluxes (LE and H) and Rn. Sites from left to right and top to lower panels: Manaus (K34), Caxiuanã (CAX), Santarém (K67) and Jaru (RJA) forests.

……………………………………………………………………………………………….

4. **Skin temperature**

To learn about the possible causes of model-observation divergences in the calculation of LW_{up} and ET, we used calculated skin temperature ($T_{skin\ LW}$; C) from observations by resolving Equation S1, assuming surface emissivity (ε_s) to be ~0.99 (satellite data as in Figure S8 and Hewison (2001)).

$$T_{skin} = \left[\frac{1}{\sigma_{SB}}\left(\frac{LW_{out} - LW_{down}}{\varepsilon_s} + LW_{down}\right)\right]^{1/4} \qquad \text{Equation S1}$$

where LW_{out} is the outgoing (W m^{-2}) and LW_{down} is the incoming longwave radiation (W m^{-2}) The derivation, and σ_{SB} is 5.6704x10^{-8} W m^{-2} K^{-4} the Stefan-Boltzmann constant. We compared the model $T_{skin\ LW}$, vegetation ($T_{vegetation}$; C) and surface temperature ($T_{surface}$; C) to observations of $T_{skin\ LW}$ (Figure S12) and found that models overestimated the skin temperature, excess temperature was significant for day-time values.

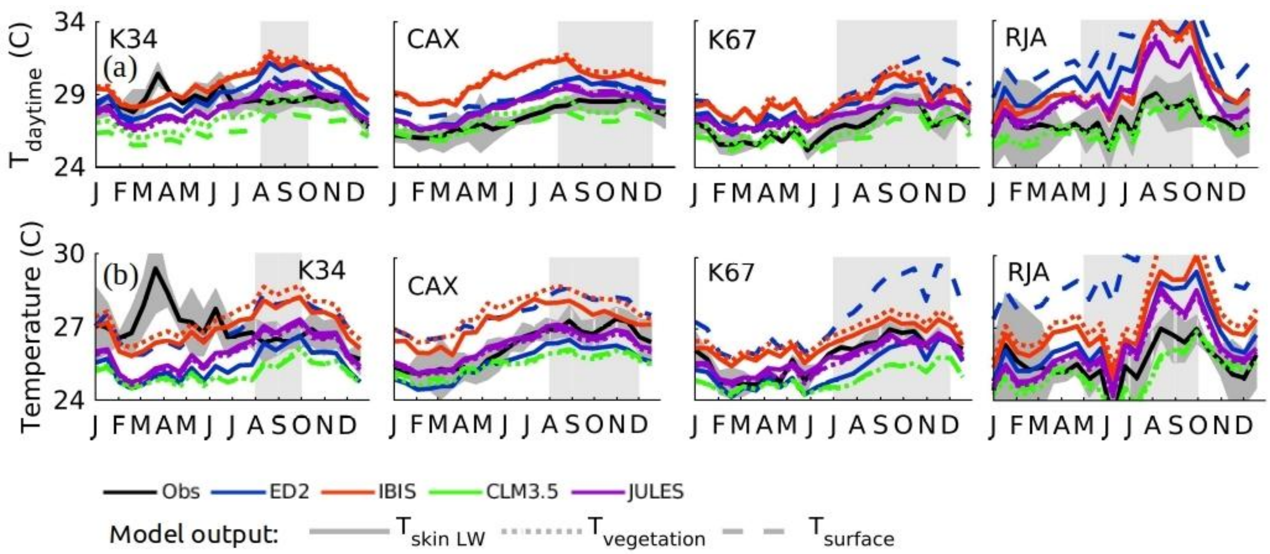

Figure S12. Annual 16-day cycle of skin temperature calculated from longwave radiation measurements and fixed surface emissivity values of 0.99 ($T_{skin\ LW}$; C) (black thick line) (a) daytime values of $T_{skin\ LW}$ and (b) all available observations). Model estimates of $T_{skin\ LW}$, vegetation temperature ($T_{vegetation}$; C) and surface temperature ($T_{surface}$; C). From top to bottom and left to right and top to lower panels study sites (from wettest to driest) Manaus (K34), Caxiuana (CAX), Santarém (K67), and Reserva Jaru (RJA) forests. Light gray-shaded area is dry season as defined using satellite-derived measures of precipitation (TRMM: 1998–2018). Simulations from ED2 (blue), IBIS (red), CLM3.5 (green), and JULES (purple).

…………………………………………………………………………………………………….

5. Regressions informing surface emissivity and albedo seasonal cycles and ancillary analysis

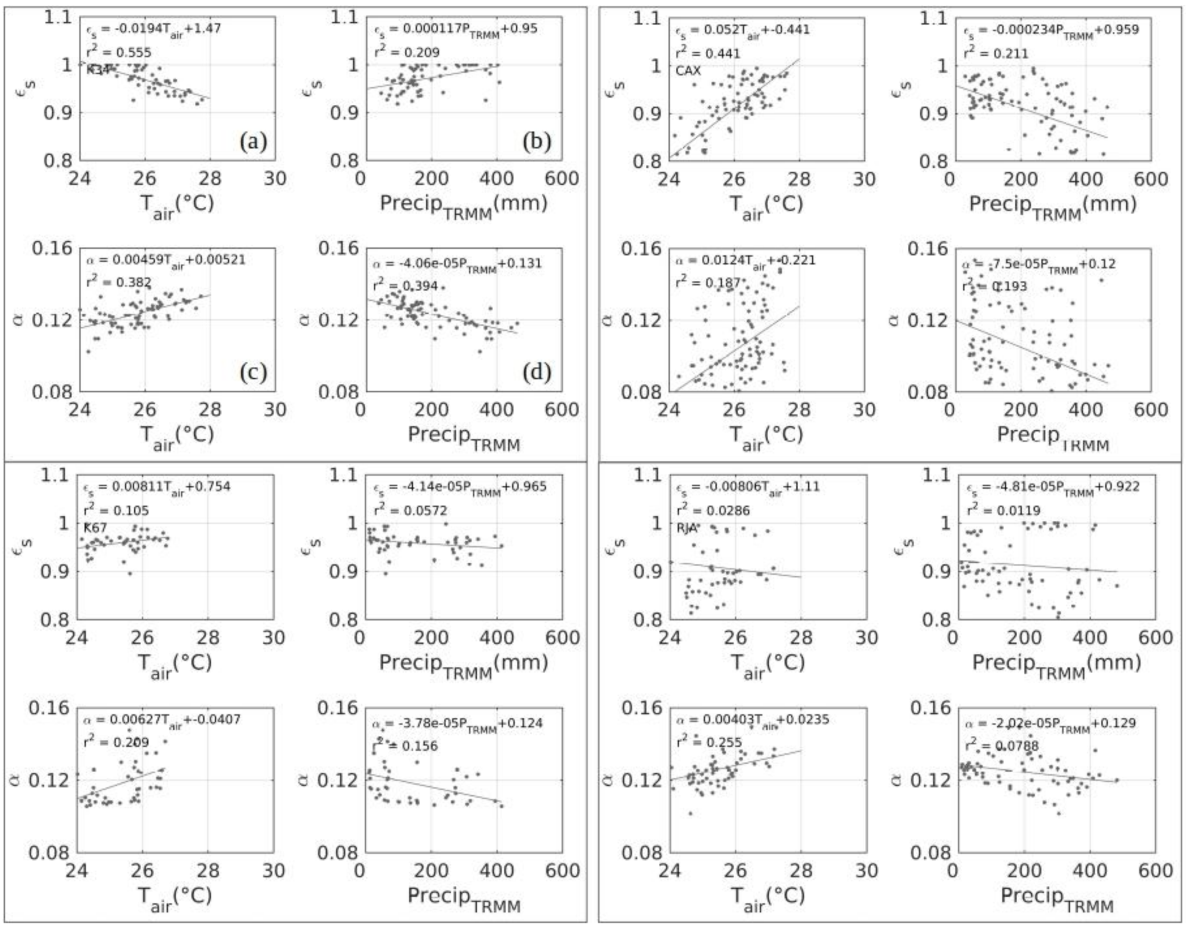

Figure S13. Type II linear regressions between 16-day time series for each site: surface emissivity (ε_s) and air temperature (T_{air}; degC), (b) ε and satellite derived precipitation ($Precip_{TRMM}$; mm month^{-1}), (c) albedo (α) and air temperature (T_{air}; degC), α and (d) and $Precip_{TRMM}$. Sites from left to right and top to lower panels: Manaus (K34), Caxiuanã (CAX), Santarém (K67) and Jaru (RJA) forests.

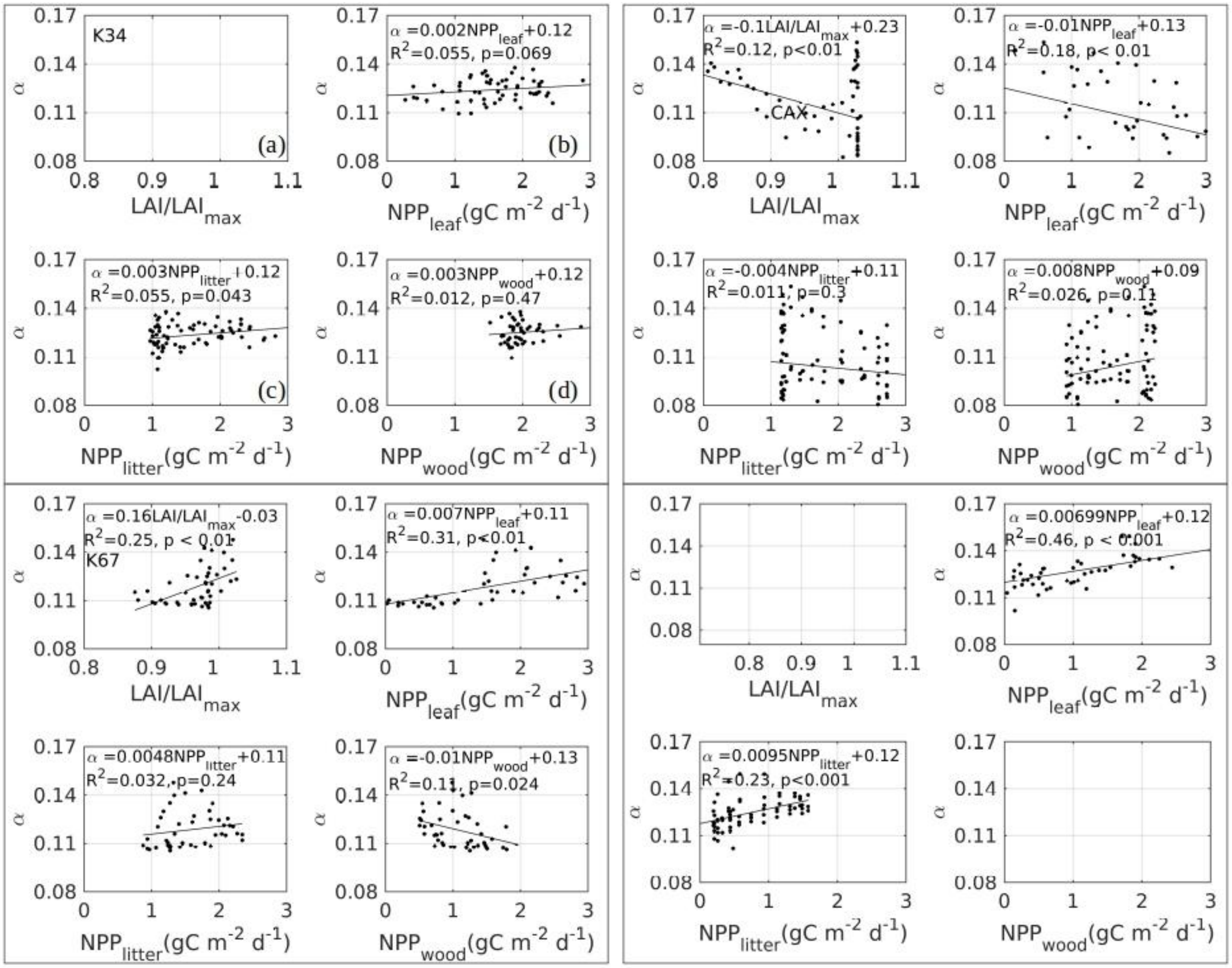

Figure S14: Type II linear regressions between 16-day time series for each site: (a) albedo defined as the ratio of outgoing to incoming shortwave radiation (α=SW_{out}/SW_{down}) (continuous line) and leaf area index (LAI) normalized by its maximum value (LAI/LAI_{max}), (b) net primary productivity allocated to leaves (NPP_{leaf}; gC m^{-2} d^{-1}), (c) net primary productivity from leaf-fall (NPP_{leaf}; gC m^{-2} d^{-1}) and (d) net primary productivity allocated to wood (NPP_{wood}; gC m^{-2} d^{-1}) as in Restrepo-Coupe et al. (2017). No LAI or wood biomass data were available for Jaru (RJA) forest. Lower right panel: Sites from left to right and top to lower panels: Manaus (K34), Caxiuanã (CAX), and Santarém (K67) sites.

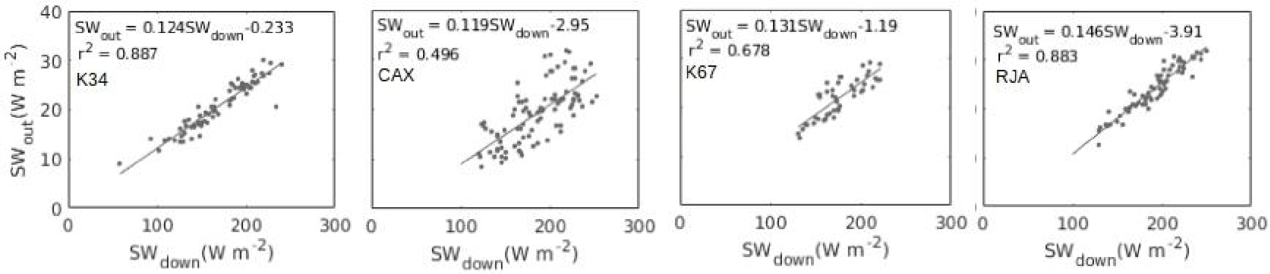

Figure S15: Type II linear regressions between 16-day time series of incoming shortwave radiation (*SW_{down}*; W m^{-2}) and outgoing shortwave (*SW_{out}*; W m^{-2}). From left to right (wettest to driest) near Manaus (K34), Caxiuanã (CAX), Santarém (K67), and Reserva Jaru southern (RJA) forests.

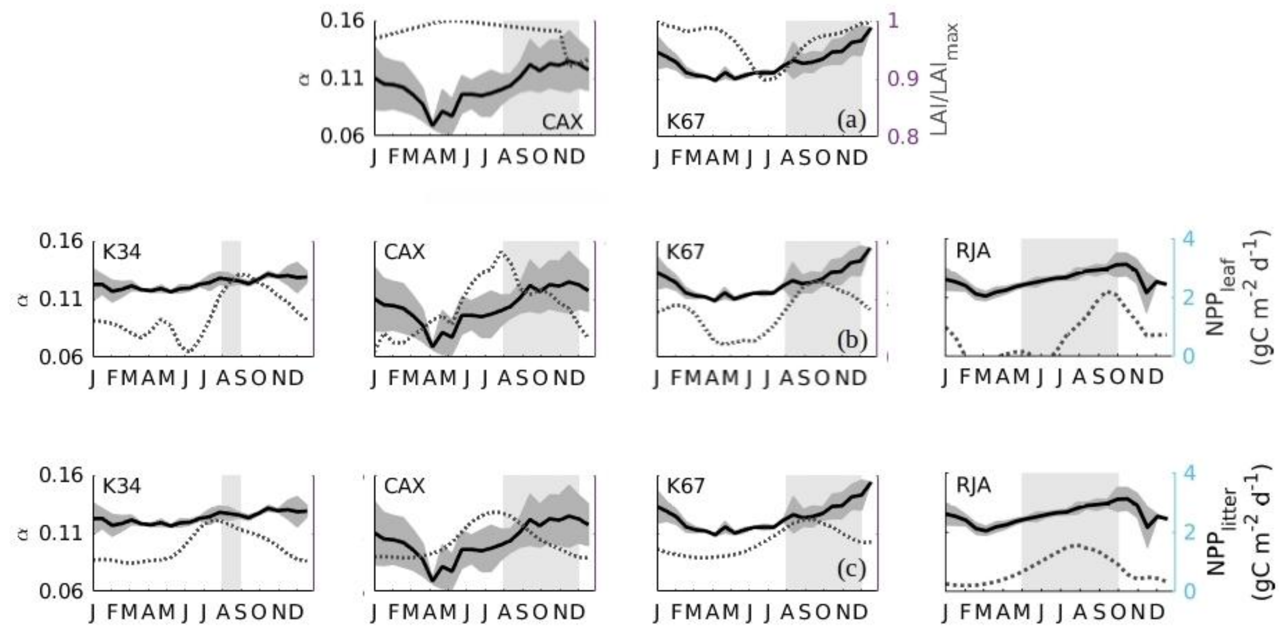

Figure S16. Annual monthly cycle of (a) albedo defined as the ratio of outgoing to incoming shortwave radiation (α=SW_{out}/SW_{down}) (continuous line) and leaf area index (*LAI*) normalized by its maximum value (LAI/LAI_{max}), (b) net primary productivity allocated to leaves (NPP_{leaf}; gC m^{-2} d^{-1}) as in Restrepo-Coupe et al. (2016) (dashed line) and (c) net primary productivity from leaf-fall (NPP_{leaf}; gC m^{-2} d^{-1}) (dashed line). From left to right and top to lower panels study sites (from wettest to driest) near Manaus (K34), Caxiuanã (CAX), Santarém (K67), and Reserva Jaru southern (RJA) forests.

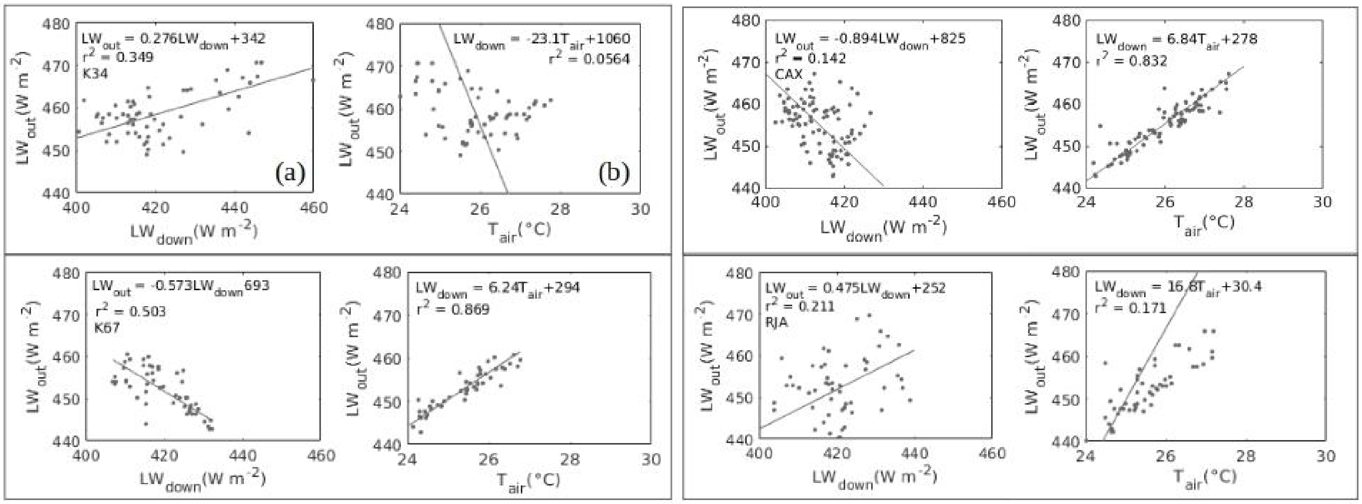

Figure S17. Type II linear regression between 16-day time series for each site: (a) outgoing longwave radiation (LW_{out}; W m^{-2}) and incoming longwave radiation (LW_{down}; W m^{-2}) and (b) LW_{out} and air temperature (T_{air}; ºC). Sites from left to right and top to lower panels: Manaus (K34), Caxiuanã (CAX), Santarém (K67) and Jaru (RJA) forests.

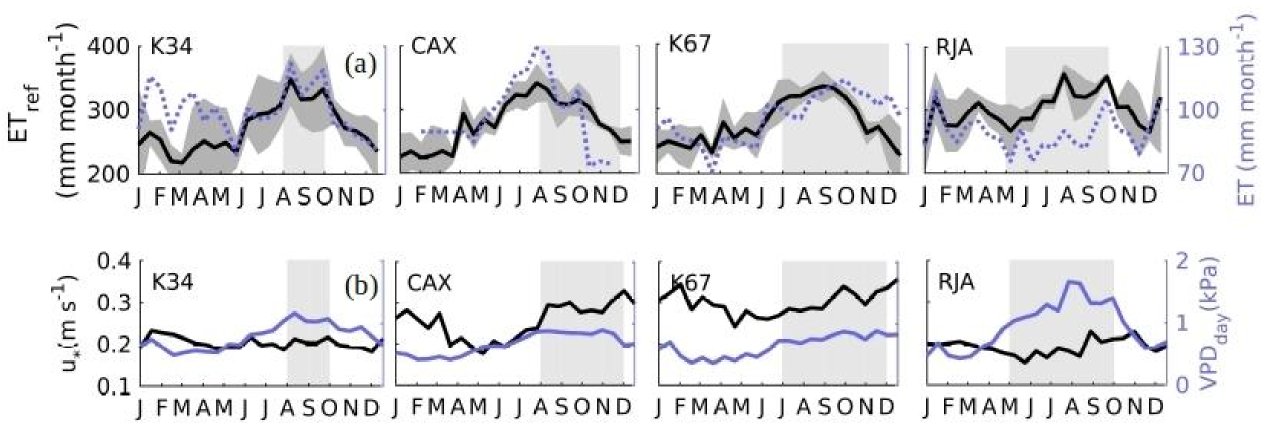

Figure S18. Annual cycle 16-day average (a) evapotranspiration (ET; mm month^{-1}) and reference (driven by radiation, atmospheric demand and temperature) ET (ET_{ref}; mm month^{-1}); and (b) friction velocity (u_*; m s^{-1}) and daytime vapor pressure deficit (VPD_{day}; kPa). From left to right study sites (from wettest to driest) near Manaus (K34), Caxiuanã (CAX), Santarém (K67), and Reserva Jaru southern (RJA) forests. Light gray-shaded area is dry season as defined using satellite-derived measures of precipitation (TRMM: 1998–2018).

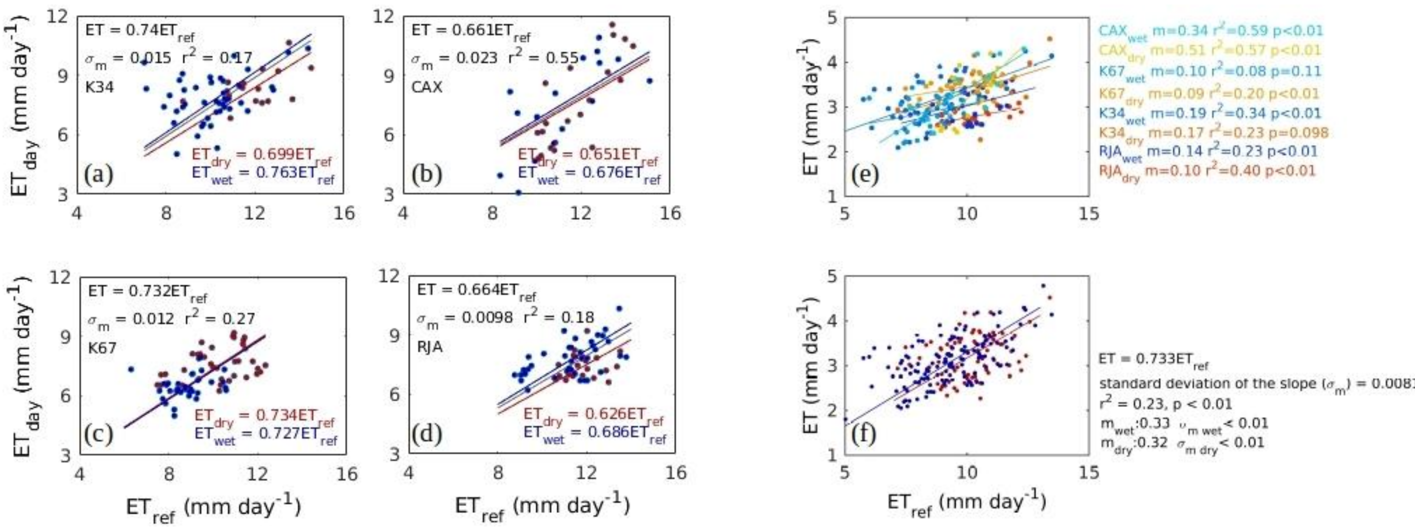

Figure S19. Type II linear regression (without intercept) between 16-day time series for each site (a to d): daytime observed evapotranspiration (ET_{day}; mm day^{-1}) and reference (ET_{ref}; mm day^{-1}), wet (*Precip* > 100 mm month^{-1}) (blue dots and text) and dry-season (*Precip* <= 100 mm month^{-1}) (red dots and text). Includes equations for all available data -- regardless of rainfall conditions (gray text). Sites from left to right and top to lower panels: Manaus (K34), Caxiuanã (CAX), Santarém (K67) and Jaru (RJA) forests. Right panels (e and f) regressions for all sites combined in a single regression. The σ_m is the standard deviation of the regression's slope.

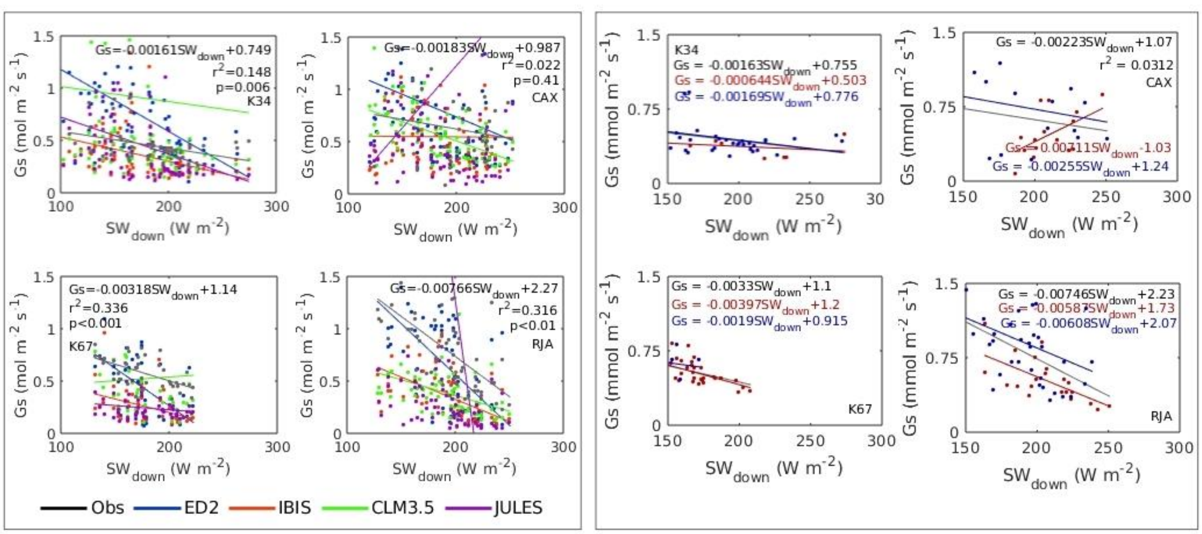

Figure S20. Left side panels: Linear regression between 16-day time series for each site of canopy conductance (*Gs*; mm s^{-1}) vs. incoming shortwave radiation (SW_{down}; W m^{-2}). Right panels: Similar regressions for all data (black text) and wet (Precip > 100 mm month^{-1}) (blue dots and text) and dry-season (*Precip* <= 100 mm month^{-1}) (red dots and text). From left to right and top to lower panels study sites (from wettest to driest) near Manaus (K34), Caxiuanã (CAX), Santarém (K67), and Reserva Jaru southern (RJA) forests. Simulations from ED2 (blue), IBIS (red), CLM3.5 (green), and JULES (purple).

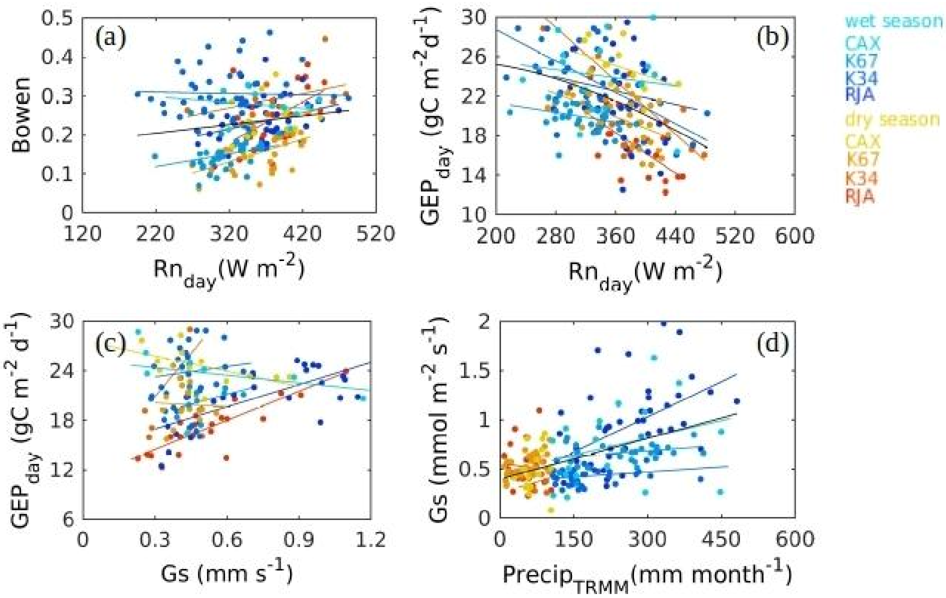

Figure S21. All site regressions between seasonal values of (a) unitless Bowen ratio (*Bowen=H/LE*) and daytime net radiation (Rn_{day}; W m^{-2}), (b) daytime gross primary productivity (GEP_{day}; gC m^{-2} d^{-1}) and Rn_{day}, (c) GEP_{day} and canopy conductance (*Gs*; mm s^{-1}), (d) the ratio of GEP_{day} and *Gs* and Rn_{day} and (e) *Gs* and satellite-derived precipitation from the Tropical Rainfall Mission ($Precip_{TRMM}$; mm $month^{-1}$). Panel b and c include a second degree polynomial and panels a, d and e include a type II linear regression fitted for all sites and periods available: Manaus (K34), Caxiuanã (CAX), Santarém (K67), and Reserva Jaru southern (RJA) forests.

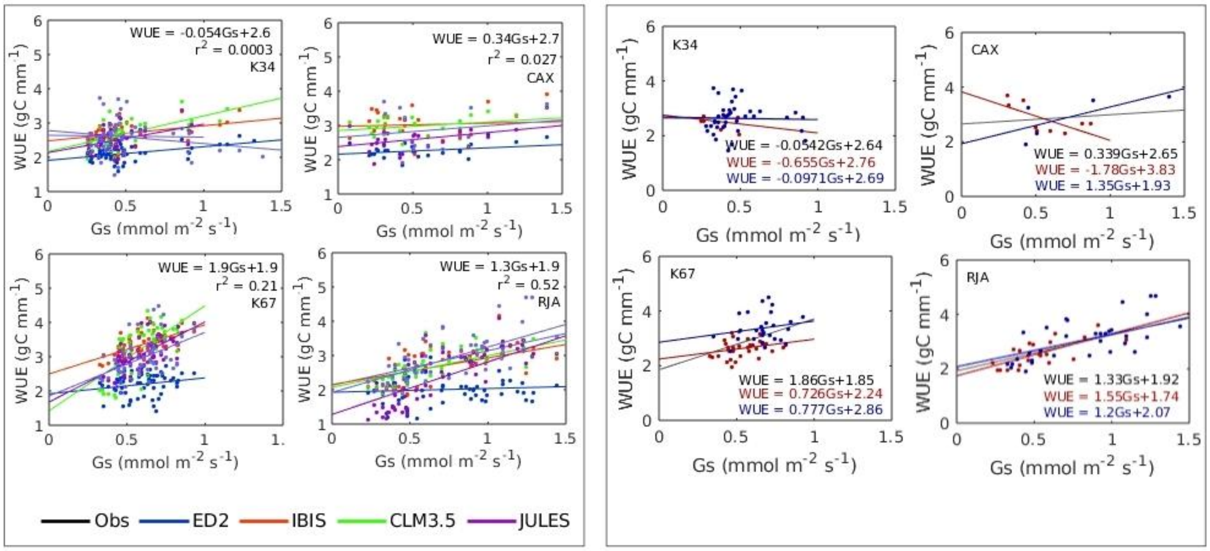

Figure S22: Left side panels: Linear regression between 16-day time series for each site of canopy conductance (*Gs*; mm s^{-1}) vs. daytime water use efficiency where evapotranspiration (*ET*) was sampled during dry conditions, excluding 12 hours after rainfall, as to sample periods when transpiration (*T*) drives water fluxes ($WUE=GEP_{day}/ET_{dry}$, gC mm^{-1}). Right panels: Similar regressions for all data (black text) and wet (*Precip* > 100 mm month^{-1}) (blue dots and text) and dry-season (*Precip* <= 100 mm month^{-1}) (red dots and text). From left to right and top to lower panels study sites (from wettest to driest) near Manaus (K34), Caxiuanã (CAX), Santarém (K67), and Reserva Jaru southern (RJA) forests. Simulations from ED2 (blue), IBIS (red), CLM3.5 (green), and JULES (purple).

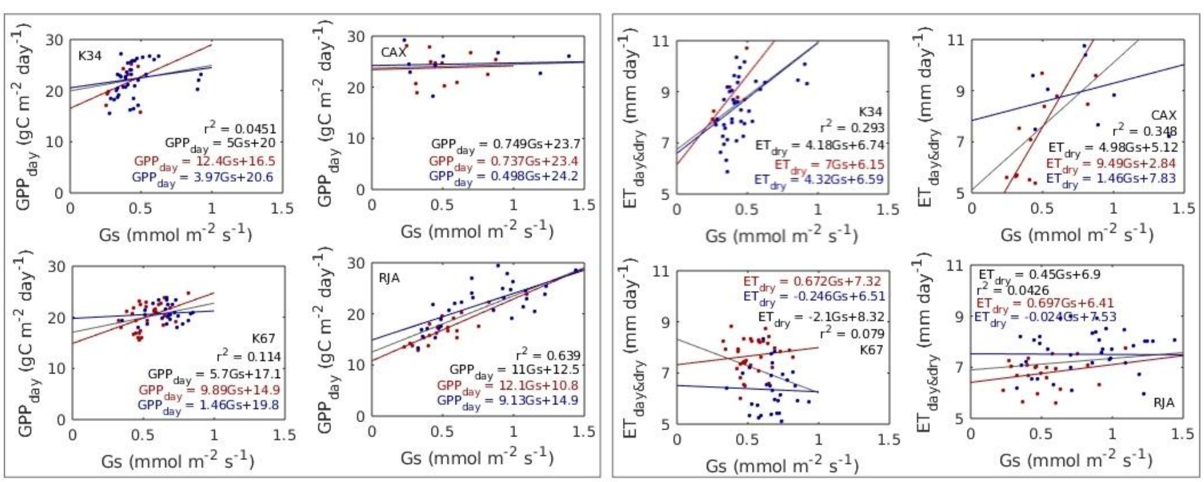

Figure S23. Linear regression between 16-day time series for each site of canopy conductance (Gs, mm s^{-1}) *vs*. daytime gross ecosystem exchange (GPP_{day}; gC m^{-2} d^{-1}) left side, and right hand side evapotranspiration for daytime and excluding periods 12 hours after rainfall ($ET_{dry\&dry}$; mm day^{-1}) for all data (black text) and wet (*Precip*>100 mm $month^{-1}$) (blue dots and text) and dry-season (*Precip*<=100 mm $month^{-1}$) (red dots and text). Sites from left to right and top to lower panels: Manaus (K34), Caxiuanã (CAX), Santarém (K67) and Jaru (RJA) forests.

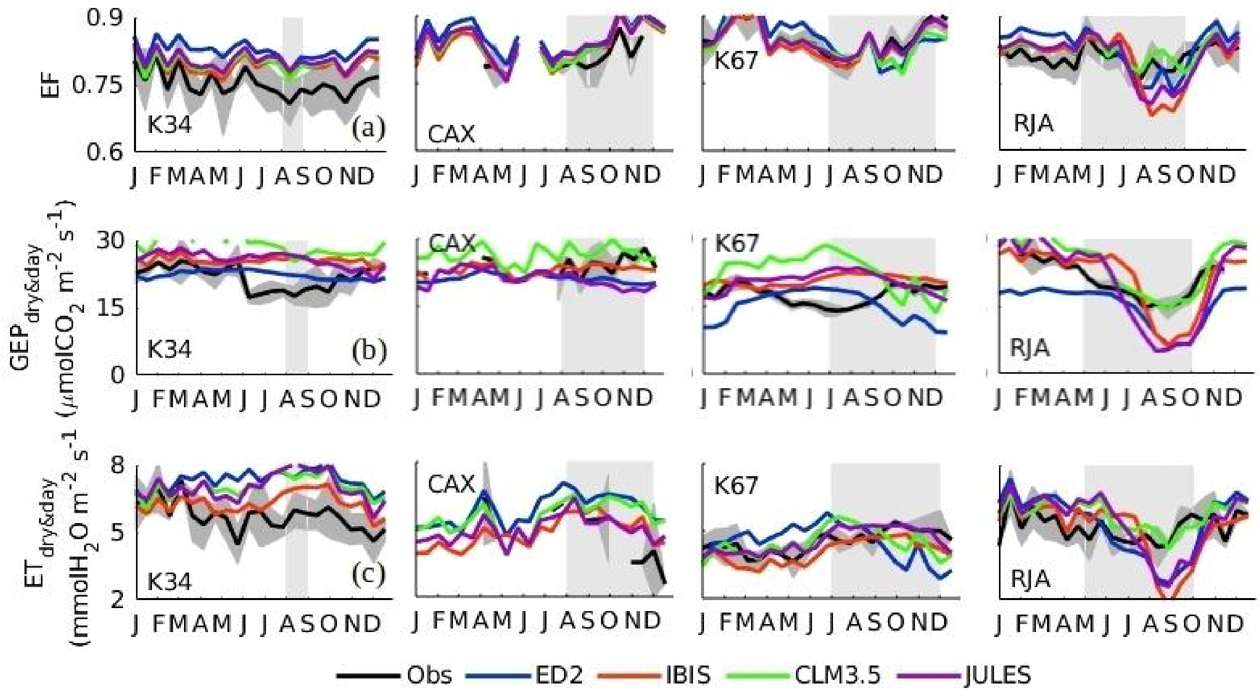

Figure S24: Annual cycle 16-day average (a) evaporative fraction (*EF*), calculated as *EF=LE/(LE+H)*, where *LE* is latent and *H* is sensible heat flux), (b) daytime gross ecosystem photosynthesis (GEP_{day}; μmolCO_2 m^{-2} s^{-1}), and (c) daytime evapotranspiration no precipitation prior 12 hours ($ET_{dry\&day}$; mmolH_2O m^{-2} s^{-1}). From left to right study sites (from wettest to driest) near Manaus (K34), Caxiuanã (CAX), Santarém (K67), and Reserva Jaru southern (RJA) forests. Light gray-shaded area is dry season as defined using satellite-derived measures of precipitation (TRMM: 1998–2018). Simulations from ED2 (blue), IBIS (red), CLM3.5 (green), and JULES (purple).

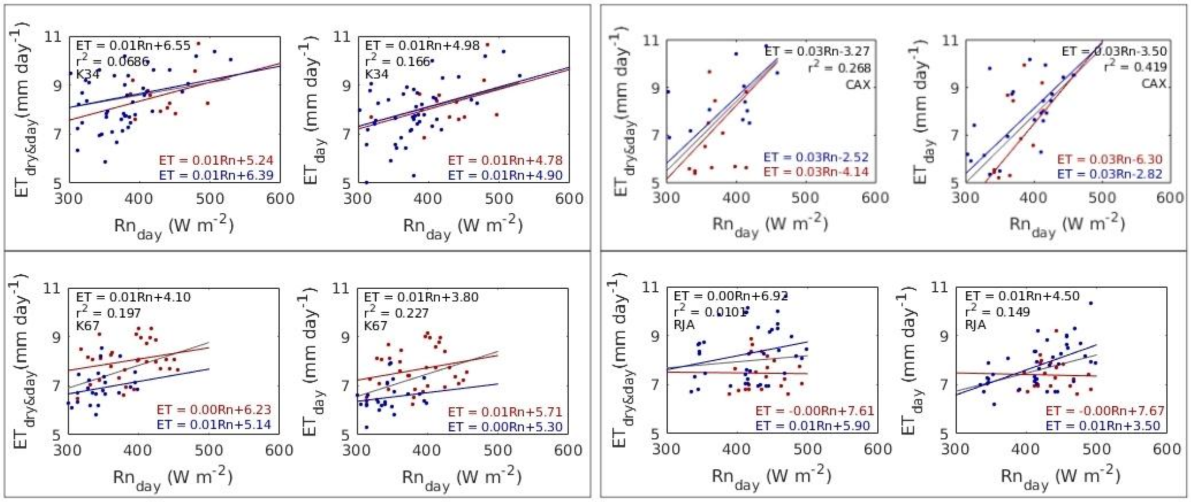

Figure S25. Type II linear regression between 16-day time series for each site of evapotranspiration (*ET*) during day and no precipitation the previous 12 hours (*Gs*; mm s^{-1}) vs. incoming shortwave radiation (SW_{down}; W m^{-2}). Right panels: Similar regressions for all data (black text) and wet (*Precip* > 100 mm month^{-1}) (blue dots and text) and dry-season (*Precip* <= 100 mm month^{-1}) (red dots and text). From left to right and top to lower panels study sites (from wettest to driest) near Manaus (K34), Caxiuanã (CAX), Santarém (K67), and Reserva Jaru southern (RJA) forests.

……………………………………………………………………………………………………

6. Sensitivity analysis variables used to calculate ecosystem canopy conductance (G_s) by the flux gradient method

Here we review the sensitivity of the canopy conductance values (G_s; mmol m^{-2} s^{-1}) to the various variables used in its calculation (highlighted in green). We present the flux-gradient method as described by Wehr and Saleska (2015; 2020), where G_s is calculated as:

$$Gs = \frac{100Pa}{Rm\,(T_L + 273.15)\; rsV} \qquad \text{Equation S2}$$

where T_L is the internal leaf temperature [°C], R_m is the molar gas constant (8.314472 J mol^{-1} C^{-1}) and rsV stomatal resistance to water vapor (s m^{-1}) calculated:

$$rsV = \frac{esat(T_L) - ea}{R_m\,(Tair + 273.15)\,F_{H2O}} - rbV \qquad \text{Equation S3}$$

where, $esat_{(TL)}$ is saturation vapor pressure (Pa) at temperature T_L, e_a is the actual vapor pressure (Pa), F_{H2Odry} is flux of transpired water vapor (mol m^{-2} s^{-1}) ($ET_{dry} = \lambda \times 18.015 \times 10^3 F_{H2Odry}$) and rbV is the leaf boundary layer resistance to water vapor (s m^{-1}). The rbV was calculated using the Schmidt number for water vapor (Scv=0.67), the Prandtl number for air (P_r=0.71), the fraction of the leaf surface area that contains stomata (f=0.5, assuming the forest to be dominated by hypostomatous leaves, only one side has stomata):

$$r_{bV} = \frac{1}{f} r_{bH} \left(\frac{Scv}{P_r}\right)^{2/3} \qquad \text{Equation S4}$$

where rbH is the canopy flux weighted leaf boundary layer (s m^{-1}):

$$r_{bH} = \frac{150}{LAI} \left(\frac{L\,exp(\alpha_u(1-(h_{cpy}/h))}{u_{cpy}}\right)^{1/2} \qquad \text{Equation S5}$$

where LAI is the leaf area index, L is the characteristic leaf dimension (m) (Malhado et al., 2009), α_u is the extinction coefficient for the assumed exponential wind profile (α_u= 4.39-(3.97 exp$^{(-0.258\,LAI)}$), h_{cpy} is mean top canopy height (m), h is the anemometer height (m) and u_{cpy} is the mean wind speed at top canopy height (m s^{-1}) ($u_{cpy} = ws/exp((\alpha_u\,h_{cpy}/h)-1)$). The rbH was used to derive T_L as follows:

$$T_L = T_{air} + \frac{H\,rbH}{\rho_a C_p} \qquad \text{Equation S6}$$

where ρ_a is the mean air density (kg m^{-3}), and C_p is the specific heat of air at constant pressure (J kg^{-1} K^{-1}). Calculations of G_s were restricted to the periods where ET_{dry} was available (ET

dominated by *T* rather than *E*).

ID	Abbreviation	Scenario
1	Base	L = 0.09, seasonal measurements of *LAI* and correspondent extinction coefficients, *LE* and *H* uncorrected for EB imbalance, T_L, *rsV* calculated following Equations S2-S6.
2	LAI50	Fixed *LAI* values at 5.0
3	LAI55	Fixed *LAI* values at 5.53 (minimum of seasonal values)
4	LAI65	Fixed *LAI* values at 6.48 (maximum of seasonal values)
5	LAI60	Fixed *LAI* values at 6.09 (average of seasonal values)
6	Leaf013	Characteristic leaf (or needle cluster) dimension, L = 0.13
7	Leaf007	Characteristic leaf (or needle cluster) dimension, L = 0.07
8	α_u34	Fixed extinction coefficient 3.4 (minimum of seasonal values)
9	α_u37	Fixed extinction coefficient 3.65 (maximum of seasonal values)
10	α_u13	Scaled extinction coefficient 130%
11	α_u08	Extinction coefficient 70%
12	TLless1	Leaf temperature -1 C, where T_L>> $esat_{(TL)}$ is saturation vapor pressure at T_L>> rsV
13	TL095	Scaled leaf temperature -5% of calculated T_L, where T_L>> $esat_{(TL)}$ >> rsV
14	TL105	Scaled leaf temperature +5% of calculated T_L, where T_L>> $esat_{(TL)}$ >> rsV
15	TLplus1	Leaf temperature +1 C, where T_L>> $esat_{(TL)}$ >> rsV
16	LEΔ	F_{H2O} + all EB imbalance (Δ) >> $esat_{(TL)}$ >> rsV
17	LE Bowen Δ	F_{H2O} + EB imbalance scaled by the Bowen ratio (LE +Δ(1-Bowen))
18	H Δ	H + all EB imbalance (Δ)
19	H Bowen Δ	H + EB imbalance (Δ) scaled by the Bowen ratio (LE +Δ Bowen)
20	ws07	Wind speed scaled by 70%, *ws*>>u_{cpy}>>*rbH*
21	ws13	Wind speed scaled by 130%, *ws*>>u_{cpy}>>*rbH*

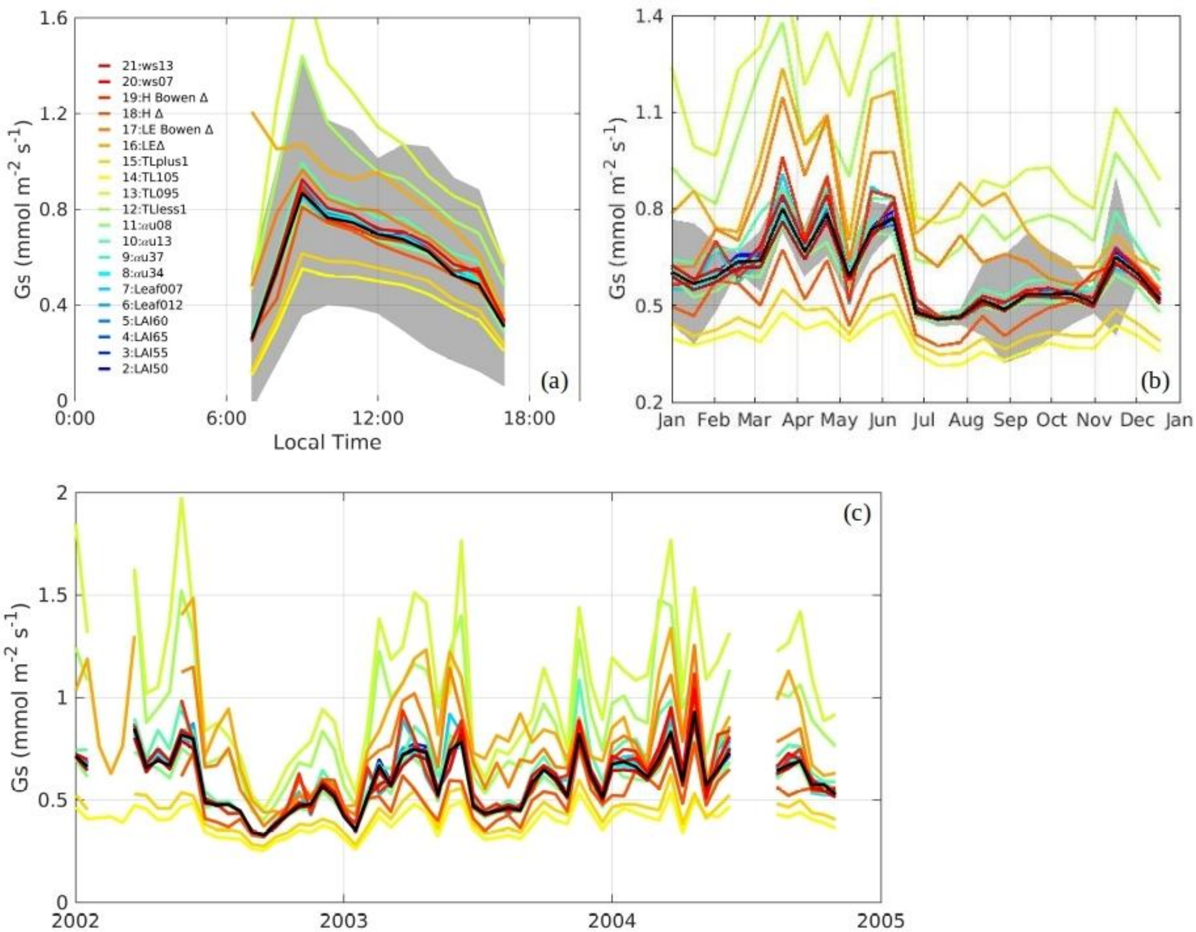

Figure S26 (a) Average daily canopy conductance (*Gs*; mmol m^{-2} s^{-1}) cycle, all data available, (b) average annual seasonal *Gs* cycle and (c) 16-day seasonal Gs at K67.

We found that the G_s model was very sensitive to T_L --the underestimation of T_L (lower than calculated T_L) (scenario 12 and 13) will translate in the overestimation of G_s and vice versa (scenario 14 and 15). Although T_L is driven by *H* and indirectly by *LAI*, *L*, wind speed and extinction coefficient (via the *rbH*), significant changes to these parameters resulted in *Gs* calculations not statistically different from the base model. As expected, adding the EB imbalance to the *LE* did increase the absolute G_s values (scenario 16 and 17), however, it did not change the amplitude or timing of the seasonal cycle.

ID	**RJA**	**K34**	**K67**	**CAX**
Lat	-10.083	-2.608	-2.857	-1.718
Lon	-61.931	-60.209	-54.959	-51.460
Site elevation (masl)	191	130	130	130
Anemometer height (m)	61.1	51.9	64.1	51.5
Canopy height (m)	35	30	40	35
u_* threshold (m s^{-1})	0.0823	0.1305	0.2212	0.0736
u_* confidence interval (m s^{-1})	0.062	0.1091	0.2005	0.0423
	0.1027	0.1519	0.2518	0.1048
Temp. profile heights (m)	62.7, 45, 35, 25, 2.7 and 0.05		62.24, 53.04, 39.41, 28.71, 19.57, 10.42, 3.05 and 0.91	51.1, 32, 16 and 1
LAI [selected in bold letters]	4.63 (1993) (leaf litter fall method) (Pyle et al., 2008). **5.5 (1999)** (optical method and LI-COR, LI-2000) (Pyle et al., 2008)) 4 (method na) (Rice et al., 2004)	**Dry season: 5 Wet season: 6 (method na)** (Malhi et al., 2002) 5.6 ± 0.2 (hemiphoto) (Malhi et al., 2009) 4.7 (allometric relation at Jacaranda) (Malhi et al., 2009)	4.5 and 5.9 (2003) (Licor LAI-2000) (Domingues et al., 2005). **Jan-Dec: 4.98, 4.94, 5.00, 4.85, 5.00, 4.98, 4.97, 5.18, 5.23, 5.22, 5.23, 5.24 (Dec 2003 Nov 2004) (Licor LAI-2000)** (Costa & Cohen, 2013, p. 15)**. Jan-Dec: 6.4, 6.2, 6.1, 6.0, 5.9, 6.1, 5.7, 5.8, 6.0, 6.3, 6.1, 5.9 (Jul 2000-Sep 2004)** (LAI-2000 at control site at partial exclusion of prec experiment) (Nepstad et al., 2002). 6.4 (hemiphoto) (Malhi et al., 2009).	5–6 (method na) [Ref: P. Meir at (Iwata et al., 2005)] **5.3 ± 0.1** (hemiphoto) (Malhi et al., 2009)
Total AG Biomass (kg m^{-2})		40.61 (Malhi et al., 2009)	39.9 ± 1.6 ** (2001) (Rice et al., 2004) 41.22 (Malhi et al., 2009) 32.5 (Maria O. Hunter et al., 2015)	47.14 (Metcalfe et al., 2007)
Root depth (m)	Roots have been found to a depth of 1.65 m, and living roots down to 3 m depth have been reported (Andreae et al., 2002)		> 12 m (Nepstad et al., 2002)	

Soil type	Sandy-loam: medium textured red-yellow podzol (Andreae et al., 2002) loamy sand, giving way to a sandy-clay-loam at 0.6 m, over granitic bed-rock at a depth of 1.2 m [Ref:2] Brazil; typic paleudult (Andreae et al., 2002) FAO: orthic acrisol (Andreae et al., 2002)	Plateau 58%, lowlands 42% (10 km radius) The tertiary sediments covered by clayey Oxisols on the plateaus and sandy Spodosols on the valley bottoms (Araújo et al., 2002) FAO: clay-rich ferralsols @ plateau & podzols @ river valleys (Malhi et al., 2009) USDA: oxisol @ plateau & spodosols @ river valleys (Malhi et al., 2009)	Oxisol (Haplustox) (Oliveira et al., 2005)	Sandy-loam: medium textured red-yellow podzol (Andreae et al., 2002) loamy sand, giving way to a sandy-clay-loam at 0.6 m, over granitic bed-rock at a depth of 1.2 m (Malhi et al., 2006) Brazil; typic paleudult (Andreae et al., 2002) FAO: orthic acrisol (Andreae et al., 2002)
USD-1A texture classes: Sand (%)	80 (Andreae et al., 2002)	41.5 (Chambers et al., 2001)	18 (Keller et al., 2005) §§1.79 (Williams et al., 2002)	77 [Control plot] 83 [Dry plot] (Metcalfe et al., 2007)
Silt (%)	10 (Andreae et al., 2002)	12.9 (Chambers et al., 2001)	2 (Keller et al., 2005) §§7.71 (Williams et al., 2002)	5 [Control plot] 4 [Dry plot] (Metcalfe et al., 2007)
Clay (%)	10 (Andreae et al., 2002)	45.6 (Chambers et al., 2001)	80 (Keller et al., 2005) §§90.50 (Williams et al., 2002)	18 [Control plot] 13 [Dry plot] (Metcalfe et al., 2007)

Table S1. Brasil flux sites descriptions.

Dynamic vegetation model (DVGM)				ED2	CLM3.4	IBIS	JULES
Energy and Water Cycles							
Radiation fluxes	Is Reflectance / Transmittance / Absorptance (choose what applies)		Based on driver data / Computed by model	Computed by model	Computed by model	Computed by model	Computed by model
	Is Reflectance / Transmittance / Absorptance computed at different wavebands for the solar radiation?		Yes / No / N/A	Yes	Yes	Yes	Yes
	Does model calculate canopy radiation transfer?		Yes / No / N/A	Yes	Yes	Yes	Yes
	What radiation transfer scheme does the model uses?	3-D	Yes / No / N/A	Yes	No	No	No
		2-stream	Yes / No / N/A	Yes	Yes	Yes	Yes
		Beers law	Yes / No / N/A	No	No	No	No
		Albedo	Yes / No / N/A	Yes	No	No	Yes
		Other (specify)		Yes	N/A	N/A	N/A
	Does model represent canopy gaps with respect to canopy radiative transfer?		Yes / No / N/A	Yes	No	Yes	No
Energy fluxes	Does model partition net radiation in latent and sensible heat fluxes?		Yes / No / N/A	Yes	Yes	Yes	Yes
	Does model simulate ground heat flux?		Yes / No / N/A	Yes	Yes	Yes	Yes
	How does the model simulate canopy heat storage?	Computed from canopy temperature	Yes / No / N/A	Yes	No	Yes	Yes
		Vegetation heat storage term	Yes / No / N/A	Yes	No	Yes	No
		Prognostic change in canopy heat storage	Yes / No / N/A	Yes	No	Yes	Yes
		Non specified - Residual	Yes / No / N/A	Yes	Yes (assumed to be negligible)	N/A	N/A
Conductances	Does model parametrize turbulent processes?		Yes / No / N/A	Yes	Yes	Yes	Yes
	Does model parametrize in-canopy diffusive processes?		Yes / No / N/A	Yes	Yes	Yes	Yes
	Does model parametrize canopy / stomatal conductance?	Shaded leaves	Yes / No / N/A	Cohort-based model. Some cohorts will be partially or fully shaded.	Yes	No	No (for this study, but shade/sun configuration available)
		Sun leaves	Yes / No / N/A	Cohort-based model. Some cohorts will be partially or fully exposed.	Yes	No	No (for this study, but shade/sun configuration available)
		Whole canopy (No distinction)	Yes / No / N/A	No	No	Yes	Yes
	What stomatal conductance scheme does the model uses?	Jarvis-type	Yes / No / N/A	No	No	No	No
		Ball-Berry	Yes / No / N/A	No	Yes	Yes	Yes
		Other (specify)		Leuning (1995)	Collatz et al. (1991)	N/A	Jacobs (1994)
	Is the canopy / stomatal conductance connected to the photosynthesis component?		Yes / No / N/A	Yes	Yes	Yes	Yes
Precipitation partition	Among which processes is the precipitation partitioned?	Throughfall	Yes / No / N/A		Yes	Yes	es
		Interception	Yes / No / N/A	Yes	Yes	Yes	Yes
		Transpiration	Yes / No / N/A	Yes	Yes	Yes	Yes
		Soil evaporation	Yes / No / N/A	Yes	Yes	Yes	Yes
		Canopy evaporation	Yes / No / N/A	Yes	Yes	Yes	Yes
		Runoff	Yes / No / N/A	Yes	Yes	Yes	Yes
		Groundwater flow	Yes / No / N/A	Yes out	Yes	Yes	
		Subsurface flow	Yes / No / N/A	Yes out	Yes	Yes	
Time step SVAT	What is the time step of the SVAT, in hours?		[hours] / N/A	Dynamic maximum 0.25 hours	0.5	1 hour	0.5 hours

Table S2. Model description: Energy and water cycle dynamics, as from LBA-DMIP (de Goncalves et al., 2009).

	K34	CAX	K67	RJA	All sites
LE ~ Intercept + a Rn + b Tair					
Estimated Coefficients:Estimate [SE] pValue					
(Intercept)	295.15 [682.44] 0.667	2344.158 [1138.996] 0.049	-1702.758 [344.058] 5.571e-06	145.522 [308.797] 0.639	-461.23 [253.16] 0.07
a	0.349 [0.065] 1.297e-06	0.949 [0.1224] 1.91e-08	0.2012 [0.058] 0.001	0.182 [0.057] 0.002	0.31 [0.034] 3.81e-17
b	-0.85 [2.28] 0.709	-8.01 [3.81] 0.045	5.89 [1.162] 3.59e-06	-0.301 [1.0467] 0.775	1.697 [0.85] 0.048
Number of observations	64	31	68	59	220
Error degrees of freedom	61	28	65	56	217
Root Mean Squared Error	12.4	15.8	7.23	7.84	11.8
R-squared	0.459	0.683	0.503	0.175	0.385
Adjusted R-Squared	0.442	0.661	0.488	0.146	0.38
F-statistic vs. constant model	25.9	30.2	32.9	5.95	68
P-value	7.15E-09	1.01E-07	1.32E-10	0.00454	1.18E-23
AICvalue	5.07E+02	2.62E+02	4.65E+02	4.13E+02	1.71E+00
diff LE_{model} - LE_{observations}	5.84E-14	6.83E-14	3.27E-13	-3.47E-14	-1.80E-13
LE ~ Intercept + a Rn + b Tair + c Rn x Tair					
Estimated Coefficients:Estimate [SE] pValue					
(Intercept)	4180.73 [1775.335] 0.022	1033.88 [7226.829] 0.887	-675.61 [2329.656] 0.773	1266.943 [2089.92] 0.547	602.55 [1159.9] 0.6
a	-31.0229 [13.31] 0.023	10.4123 [51.51959] 0.841	-8.847 [20.294] 0.664	-8.02 [15.109] 0.598	-7.88 [8.71] 0.37
b	-13.77 [5.909] 0.023	-3.6356 [24.113] 0.8813	2.452 [7.799] 0.754	-4.063 [7.013] 0.565	-1.865 [3.88] 0.632
c	0.104 [0.044] 0.0217	-0.0316 [0.1719] 0.8556	0.0303 [0.0679] 0.657	0.0275 [0.051] 0.589	0.027 [0.029] 0.348
Number of observations	64	31	68	59	220
Error degrees of freedom	60	27	64	55	216
Root Mean Squared Error	1.20E+01	1.61E+01	7.28E+00	7.89	1.18E+01
R-squared	0.505	0.684	0.505	0.18	0.388
Adjusted R-Squared	0.48	0.649	0.482	0.135	0.379
F-statistic vs. constant mode	20.4	19.5	21.8	4.01	45.6
P-value	3.08E-09	6.33E-07	7.90E-10	0.0118	7.13E-23
AICvalue	5.04E+02	2.64E+02	4.67E+02	4.15E+02	1.71E+03
diff LE_{model} - LE_{observations}	6.04E-13	4.35E-13	-1.21E-13	-1.01E-13	2.90E-13
LE ~ Intercept + a SWdown + b Tair					
Estimated Coefficients:Estimate [SE] pValue					
(Intercept)	1227.832 [642.07] 0.0598	5420.45 [1352.435] 0.0004	-1557.245 [546.415] 0.0067	10.85 [338.25] 0.974	-88.043 [301.13] 0.77
a	0.281 [0.0565] 4.216e-06	0.7846 [0.11] 9.17e-08	0.1514 [0.0589] 0.0137	0.0734 [0.0416] 0.083	0.224 [0.031] 1.174E-11
b	-3.973 [2.157] 0.0695	-18.332 [4.55] 0.0004	5.3927 [1.8544] 0.00579	0.186 [1.147] 0.872	0.442 [1.019] 0.665
Number of observations	76	31	45	59	209
Error degrees of freedom	73	28	42	56	206
Root Mean Squared Error	14.7	16.7	7.21	8.3	13
R-squared	2.98E-01	6.47E-01	5.39E-01	0.0764	2.97E-01
Adjusted R-Squared 0.279	2.79E-01	6.21E-01	5.17E-01	0.0434	2.91E-01
F-statistic vs. constant model	15.5	25.6	24.6	2.32	43.6
P-value	2.48E-06	4.74E-07	8.59E-08	0.108	1.61E-16
AICvalue	6.28E+02	2.65E+02	3.08E+02	4.20E+02	1.67E+03
diff LE_{model} - LE_{observations}	7.97E-14	7.87E-13	3.57E-13	6.26E-15	2.19E-14
LE ~ Intercept + a Tair					
Estimated Coefficients:Estimate [SE] pValue					
(Intercept)	-1044.884 [518.421] 0.047	755.711 [1952.93] 0.7016	-2215.327 [334.838] 7.323e-09	-283.144 [299.65] 0.349	-1374.9 [254.57] 1.65E-07
a	3.742 [1.723] 0.033	-2.235 [6.519] 0.734	7.688 [1.122] 2.755e-09	1.2188 [1.0045] 0.23	4.89 [0.852] 3.0E-08
Number of observations	76	31	69	59	233
Error degrees of freedom	74	29	67	57	231
Root Mean Squared Error	16.9	27.5	7.77	8.45	14.1
R-squared	0.0599	0.00404	0.412	0.0252	0.125
Adjusted R-Squared	0.0472	-0.0303	0.403	0.00808	0.121
F-statistic vs. constant model	4.72E+00	1.18E-01	4.70E+01	1.47	3.29E+01
P-value	3.31E-02	7.34E-01	2.76E-09	0.23	3.00E-08
AICvalue	6.48E+02	2.95E+02	4.81E+02	4.21E+02	1.90E+03
diff LE_{model} - LE_{observations}	-9.91E-14	6.94E-14	6.30E-13	1.30E-13	-9.29E-14
LE ~ Intercept + a Swdown					
Estimated Coefficients:Estimate [SE] pValue					
(Intercept)	45.296 [7.139] 1.595e-08	-27.4 [23.998] 0.263	31.631 [8.1899] 0.00037	65.6041 [6.942] 2.87e-13	42.384 [4.64] 6.357E-17
a	0.206 [0.0399] 1.933e-06	0.5649 [0.1179] 4.5408e-05	0.270 [0.0459] 5.311e-07	0.0769 [0.035] 0.0346	0.232 [0.0248] 1.488E-17
Number of observations	76	31	45	59	209
Error degrees of freedom	74	29	43	57	207
Root Mean Squared Error	15	20.6	7.81	8.22	13
R-squared	0.265	0.442	0.446	0.076	0.297
Adjusted R-Squared	0.255	0.423	0.434	0.0598	0.293
F-statistic vs. constant model	2.67E+01	2.29E+01	3.47E+01	4.69	8.74E+01
P-value	1.93E-06	4.54e-05	5.31E-07	0.0346	1.49E-17
AICvalue	6.29E+02	2.77E+02	3.15E+02	4.18E+02	1.67E+03
diff LE_{model} - LE_{observations}	2.58E-14	3.37E-14	-1.04E-14	4.82E-16	2.03E-14
LE ~ Intercept + a Rn					
Estimated Coefficients:Estimate [SE] pValue					
(Intercept)	39.768 [5.615] 1.552e-09	-43.392 [17.812] 0.0194	40.0516 [7.411] 9.602e-07	56.728 [6.921] 3.239e-11	41.77 [3.89] 7.013E-22
a	0.332 [0.046] 8.267e-10	0.899 [0.127] 8.607e-08	0.329 [0.061] 9.367e-07	0.175 [0.0504] 0.001	0.34 [0.03] 5.77E-24
Number of observations	64	31	68	59	220
Error degrees of freedom	62	29	66	57	218
Root Mean Squared Error	12.3	15.6	8.48	7.78	11.8
R-squared	0.458	0.636	0.307	0.174	0.374
Adjusted R-Squared	0.449	0.621	0.297	0.16	0.371
F-statistic vs. constant model	5.24E+01	5.02E+01	2.93E+01	12	1.30E+02
P-value	8.27E-10	8.61E-08	9.37E-07	0.00101	5.77E-24
AICvalue	5.05E+02	2.64E+02	4.86E+02	4.11E+02	1.71E+03
diff LE_{model} - LE_{observations}	-8.44E-15	-1.88E-14	4.60E-15	1.18E-14	1.74E-15
LE ~ a Rn					
Estimated Coefficients:Estimate [SE] pValue					
a	0.6437 [0.017] 1.6771e-45	0.58194 [0.02] 1.7047e-23	0.64002 [0.01] 1.7025e-61	0.581 [0.010] 2.859e-54	0.655 [0.007] 1.94E-171
Number of observations	64	31	68	62	220
Error degrees of freedom	63	30	67	61	219
Root Mean Squared Error	16.4	16.8	10.2	11.1	14.6
R-squared	0.6812	0.805	0.563	4.44E-01	0.612
AICvalue	5.40E+02	2.64E+02	5.09E+02	4.75E+02	1.81E+03
diff LE_{model} - LE_{observations}	-3.00E+00	1.07E+00	-6.40E-01	-1.19E+00	-1.76E+00

Table S3. Latent heat flux (*LE*; W m^{-2}) linear models for four Amazonian tropical forests. Independent variables: air temperature (T_{air}, ºC), net radiation (*Rn*, W m^{-2}), and incoming shortwave radiation (SW_{down}, W m^{-2}). Sites from left to right and top to lower panels: Manaus (K34), Caxiuanã (CAX), Santarém (K67) and Jaru (RJA) forests.

References

Andreae, M. O., Artaxo, P., Brandão, C., Carswell, F. E., Ciccioli, P., Costa, A. L. da, Culf, A. D., Esteves, J. L., Gash, J. H. C., Grace, J., Kabat, P., Lelieveld, J., Malhi, Y., Manzi, A. O., Meixner, F. X., Nobre, A. D., Nobre, C., Ruivo, M. d. L. P., Silva-Dias, M. A., … Waterloo, M. J. (2002). Biogeochemical cycling of carbon, water, energy, trace gases, and aerosols in Amazonia: The LBA-EUSTACH experiments. *Journal of Geophysical Research*, *107*, 25 PP. https://doi.org/200210.1029/2001JD000524

Aragão, L. E. O. C., Malhi, Y., Roman-Cuesta, R. M., Saatchi, S., Anderson, L. O., & Shimabukuro, Y. E. (2007). Spatial patterns and fire response of recent Amazonian droughts. *Geophysical Research Letters*, *34*, 5 PP. https://doi.org/200710.1029/2006GL028946

Araújo, A. C., Nobre, A. D., Kruijt, B., Elbers, J. A., Dallarosa, R., Stefani, P., Randow, C. von, Manzi, A. O., Culf, A. D., Gash, J. H. C., Valentini, R., & Kabat, P. (2002). Comparative measurements of carbon dioxide fluxes from two nearby towers in a central Amazonian rainforest: The Manaus LBA site. *Journal of Geophysical Research*, *107*(D20), LBA 58-1-LBA 58-20. https://doi.org/200210.1029/2001JD000676

Barr, A. G., King, K. M., Gillespie, T. J., Den Hartog, G., & Neumann, H. H. (1994). A comparison of bowen ratio and eddy correlation sensible and latent heat flux measurements above deciduous forest. *Boundary-Layer Meteorology*, *71*(1), 21–41. https://doi.org/10.1007/BF00709218

Chambers, J. Q., dos Santos, J., Ribeiro, R., & Higuchi, N. (2001). Tree damage, allometric relationships, and aboveground net primary production in a tropical forest. *Forest Ecology and Management*, *152*, 73–84.

Charuchittipan, D., Babel, W., Mauder, M., Leps, J.-P., & Foken, T. (2014). Extension of the Averaging Time in Eddy-Covariance Measurements and Its Effect on the Energy Balance Closure. *Boundary-Layer Meteorology*, *152*(3), 303–327. https://doi.org/10.1007/s10546-014-9922-6

Costa, M. H., & Cohen, W. B. (2013). *LBA-ECO CD-15 LAI and Productivity Data, km 67, Tapajos National Forest: 2003-2004*. 0.256586 MB. https://doi.org/10.3334/ORNLDAAC/1167

Domingues, T. F., Berry, J. A., Martinelli, L. A., Ometto, J. P. H. B., & Ehleringer, J. R. (2005). Parameterization of Canopy Structure and Leaf-Level Gas Exchange for an Eastern Amazonian Tropical Rain Forest (Tapajós National Forest, Pará, Brazil). *Earth Interactions*, *9*(17), 1–23.

Hewison, T. J. (2001). Airborne measurements of forest and agricultural land surface emissivity at millimeter wavelengths. *IEEE Transactions on Geoscience and Remote Sensing*, *39*(2), 393–400. https://doi.org/10.1109/36.905247

Hunter, M. O., Keller, M., Vitoria, D., & Morton, D. C. (2013). Tree height and tropical forest biomass estimation. *Biogeosciences. 10:8385-8399*. https://doi.org/10.5194/bg-10-8385-2013

Hunter, Maria O., Keller, M., Morton, D., Cook, B., Lefsky, M., Ducey, M., Saleska, S., Jr, R. C. de O., & Schietti, J. (2015). Structural Dynamics of Tropical Moist Forest Gaps. *PLOS ONE*, *10*(7), e0132144. https://doi.org/10.1371/journal.pone.0132144

Iwata, H., Malhi, Y., & von Randow, C. (2005). Gap-filling measurements of carbon dioxide storage in tropical rainforest canopy airspace. *Agricultural and Forest Meteorology*, *132*(3–4), 305–314. https://doi.org/10.1016/j.agrformet.2005.08.005

Keller, M., Varner, R., Dias, J. D., Silva, H., Crill, P., Oliveira, R. C. de, & Asner, G. P. (2005). Soil–Atmosphere Exchange of Nitrous Oxide, Nitric Oxide, Methane, and Carbon Dioxide in Logged and Undisturbed Forest in the Tapajos National Forest, Brazil. *Earth Interactions*, *9*(23), 1–28. https://doi.org/10.1175/EI125.1

Malhado, A. C. M., Malhi, Y., Whittaker, R. J., Ladle, R. J., Steege, H. ter, Phillips, O. L., Butt, N., Aragão, L. E. O. C., Quesada, C. A., Araujo-Murakami, A., Arroyo, L., Peacock, J., Lopez-Gonzalez, G., Baker, T. R., Anderson, L. O., Almeida, S., Higuchi, N., Killeen, T. J., Monteagudo, A., … Laurance, W. F. (2009). Spatial trends in leaf size of Amazonian rainforest trees. *Biogeosciences*, *6*(8), 1563–1576. https://doi.org/10.5194/bg-6-1563-2009

Malhi, Y., Aragao, L. E. O. C., Metcalfe, D. B., Paiva, R., Quesadas, C. A., Almeida, S., Anderson, L., Brando, P., Chambers, J. Q., da Costa, A. C. L., Hutyra, L. R., Olivera, P., Patino, S., Pyle, E. H., Robertson, A. L., & Texteira, L. M. (2009). Comprehensive assessment of carbon productivity, allocation and storage in three Amazonian forests. *Global Change Biology*, doi: 10.1111/j.1365-2486.2008.01780.x.

Malhi, Y., Pegoraro, E., Nobre, A. D., Pereira, M. G. P., Grace, J., Culf, A. D., & Clement, R. (2002). Energy and water dynamics of a central Amazonian rain forest. *Journal of Geophysical Research*, *107*(D20), LBA 45-1-LBA 45-17. https://doi.org/200210.1029/2001JD000623

Malhi, Y., Wood, D., Baker, T. R., Wright, J., Phillips, O. L., Cochrane, T., Meir, P., Chave, J., Almeida, S., Arroyo, L., Higuchi, N., Killeen, T. J., Laurance, S. G., Laurance, W. F., Lewis, S. L., Monteagudo, A., Neill, D. A., Vargas, P. N., Pitman, N. C. A., … Vinceti, B. (2006). The regional variation of aboveground live biomass in old-growth Amazonian forests. *Global Change Biology*, *12*(7), 1107–1138. https://doi.org/10.1111/j.1365-2486.2006.01120.x

Marcolla, B., & Cescatti, A. (2018). Geometry of the hemispherical radiometric footprint over plant canopies. *Theoretical and Applied Climatology*, *134*(3), 981–990. https://doi.org/10.1007/s00704-017-2326-z

Markkanen, T., Rannik, Ü., Marcolla, B., Cescatti, A., & Vesala, T. (2003). Footprints and Fetches for Fluxes over Forest Canopies with Varying Structure and Density. *Boundary-Layer Meteorology*, *106*(3), 437–459. https://doi.org/10.1023/A:1021261606719

Metcalfe, D. B., Meir, P., Aragão, L. E. O. C., Malhi, Y., Costa, A. C. L. da, Braga, A., Gonçalves, P. H. L., Athaydes, J. de, Almeida, S. S. de, & Williams, M. (2007). Factors controlling spatio-temporal variation in carbon dioxide efflux from surface litter, roots, and soil organic matter at four rain forest sites in the eastern Amazon. *Journal of Geophysical Research*, *112*(G4), 1–9. https://doi.org/200710.1029/2007JG000443

Moderow, U., Aubinet, M., Feigenwinter, C., Kolle, O., Lindroth, A., Mölder, M., Montagnani, L., Rebmann, C., & Bernhofer, C. (2009). Available energy and energy balance closure at four coniferous forest sites across Europe. *Theoretical and Applied Climatology*, *98*(3), 397–412. https://doi.org/10.1007/s00704-009-0175-0

Nepstad, D. C., Moutinho, P., Dias-Filho, M. B., Davidson, E., Cardinot, G., Markewitz, D., Figueiredo, R., Vianna, N., Chambers, J., Ray, D., Guerreiros, J. B., Lefebvre, P., Sternberg, L., Moreira, M., Barros, L., Ishida, F. Y., Tohlver, I., Belk, E., Kalif, K., & Schwalbe, K. (2002). The effects of partial throughfall exclusion on canopy processes, aboveground production, and biogeochemistry of an Amazon forest. *Journal of Geophysical Research*, *107*, 18 PP. https://doi.org/200210.1029/2001JD000360

Oliveira, R. S., Dawson, T. E., Burgess, S. S. O., & Nepstad, D. C. (2005). Hydraulic redistribution in three Amazonian trees. *Oecologia*, *145*(3), 354–363. https://doi.org/10.1007/s00442-005-0108-2

Pyle, E. H., Santoni, G. W., Nascimento, H. E. M., Hutyra, L. R., Vieira, S., Curran, D. J., Haren, J., Saleska, S. R., Chow, V. Y., Carmago, P. B., Laurance, W. F., & Wofsy, S. C. (2008). Dynamics of carbon, biomass, and structure in two Amazonian forests. *Journal of Geophysical Research-Biogeosciences*, *113*, G00B08, 20 PP.

Restrepo-Coupe, N., Levine, N. M., Christoffersen, B. O., Albert, L. P., Wu, J., Costa, M. H., Galbraith, D., Imbuzeiro, H., Martins, G., da Araujo, A. C., Malhi, Y. S., Zeng, X., Moorcroft, P., & Saleska, S. R. (2017). Do dynamic global vegetation models capture the seasonality of carbon fluxes in the Amazon basin? A data-model intercomparison. *Global Change Biology*, *23*(1), 191–208. https://doi.org/10.1111/gcb.13442

Rice, A. H., Pyle, E. H., Saleska, S. R., Hutyra, L. R., Palace, M., Keller, M., Camargo, P. B. de, Portilho, K., Marques, D. F., & Wofsy, S. C. (2004). Carbon balance and vegetation dynamics in an old-growth Amazonian forest. *Ecological Applications*, *14*(4), S55–S71.

Twine, T. E., Kustas, W. P., Norman, J. M., Cook, D. R., Houser, P. R., Meyers, T. P., Prueger, J. H., Starks, P. J., & Wesely, M. L. (2000). Correcting eddy-covariance flux underestimates over a grassland. *Agricultural and Forest Meteorology*, *103*(3), 279–300. https://doi.org/10.1016/S0168-1923(00)00123-4

Wehr, R., & Saleska, S. R. (2015). An improved isotopic method for partitioning net ecosystem–atmosphere CO2 exchange. *Agricultural and Forest Meteorology*, *214–215*, 515–531. https://doi.org/10.1016/j.agrformet.2015.09.009

Wehr, Richard, & Saleska, S. R. (2020). Calculating Canopy Stomatal Conductance from Eddy Covariance Measurements, in Light of the Energy Budget Closure Problem. *Biogeosciences Discussions*, 1–16. https://doi.org/10.5194/bg-2020-154

Williams, Shimabukuro, Y. E., Herbert, D. A., Lacruz, S. P., Renno, C., & Rastetter, E. B. (2002). Heterogeneity of soils and vegetation in an eastern Amazonian rain forest: Implications for scaling up biomass and production. *Ecosystems*, *5*(7), 692–704. https://doi.org/10.1007/s10021-002-0165-x

Wilson, K., Goldstein, A., Falge, E., Aubinet, M., Baldocchi, D., Berbigier, P., Bernhofer, C., Ceulemans, R., Dolman, H., Field, C., Grelle, A., Ibrom, A., Law, B. E., Kowalski, A., Meyers, T., Moncrieff, J., Monson, R., Oechel, W., Tenhunen, J., … Verma, S. (2002). Energy balance closure at FLUXNET sites. *Agricultural and Forest Meteorology*, *113*(1–4), 223–243. https://doi.org/10.1016/S0168-1923(02)00109-0